Addis Ababa University

Addis Ababa Institute of Technology

African Railway Center of Excellence

Systems and Methods for Real-Time Measurements of Rail Vehicle Wheel Flange Wear using Inductive Displacement Sensor Under Effects of Temperature and Noises

A Thesis Submitted to the School of Graduate Studies of Addis Ababa
University in Partial Fulfilment of the Requirements for the Degree of
Master of Science in Railway Engineering (Traction and Train Control)

Case Study: Ethio-Djibouti Railway (Mainline)

James Ndodana Njaji

Reg. Number: GSR/7994/12

Advisor: Dr. Celestin Nkundineza

August 2021

Addis Ababa, Ethiopia

DECLARATION

I declare that this is my original work and it has not been presented anywhere in any learning institution.

APPROVAL

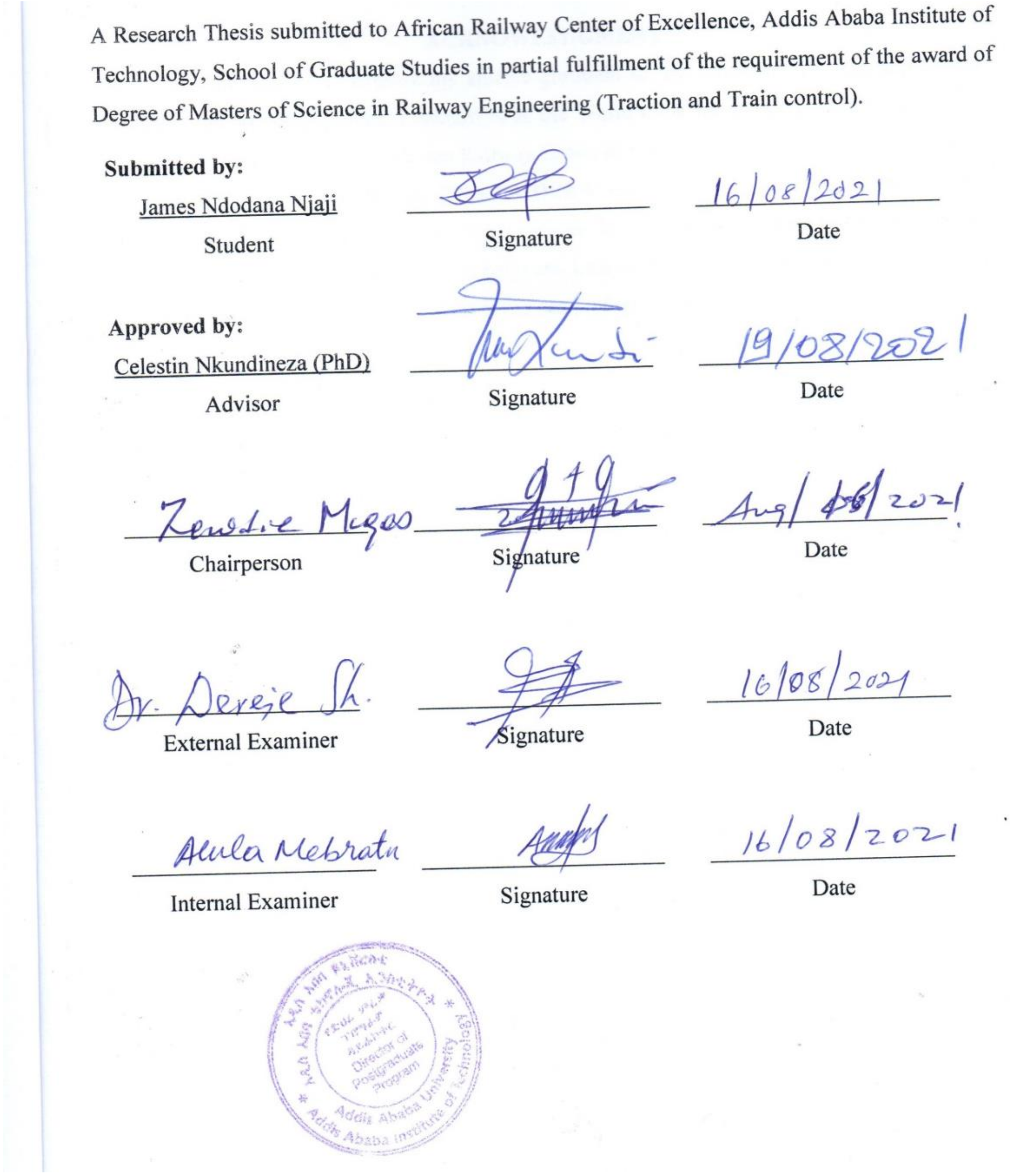

A Research Thesis submitted to African Railway Center of Excellence, Addis Ababa Institute of Technology, School of Graduate Studies in partial fulfillment of the requirement of the award of Degree of Masters of Science in Railway Engineering (Traction and Train control).

Submitted by:

James Ndodana Njaji — Signature — 16/08/2021

Student — Signature — Date

Approved by:

Celestin Nkundineza (PhD) — Signature — 19/08/2021

Advisor — Signature — Date

Zewdie Megos — Signature — Aug/ [illegible]/2021

Chairperson — Signature — Date

Dr. Dereje Sh. — Signature — 16/08/2021

External Examiner — Signature — Date

Alula Mebratu — Signature — 16/08/2021

Internal Examiner — Signature — Date

ACKNOWLEDGMENT

I take this opportunity to express my sincere gratitude to my supervisor Dr. Celestin for the research support and guidance. I acknowledge the World Bank for the support provided in this research through a grant to the African Railway Center of Excellence. I acknowledge the National Instruments Company for providing the LABVIEW and DAQ software trial licenses. I also acknowledge the support provided by Computational Mechanics ltd for providing us the free six months license of Universal Mechanism software. Last but not least I am acknowledging the lab technician, Mr. Yohannes, for assistance in the setup of the laboratory experiment.

ABSTRACT

Railway systems are expected to be in their most safe state ensuring safe operations of trains. The contact between rail and wheel is one of the most fundamental aspects of railway systems. Therefore, the instruments and measurement devices giving essential information on wheel flange wear are expected to perform accurately with high precision. This research presents an online wheel flange measurement system based on inductive sensing technology. Previous research on using the inductive displacement sensor for wheel flange wear measurement has focused on the light rail vehicles, and considered the effect of temperature negligible, as opposed to mainline vehicles where the wheel temperature variation is large. Also, the filtering of noises has been done using non-real-time data. Therefore, the objective is to study the effects of temperature on the inductive displacement sensor, employ methods to reduce measurement drifts from temperature changes, perform multibody system simulations on the locomotive, design an online filter, and design a sensor support structure mechanism to be fixed on the locomotive. Several experimental measurements are carried in the lab on a moving disk. During measurements, temperatures around the inductive displacement sensor and the metal target are increased from 19℃ to 98℃, similar to temperatures built up by flange and tread contact in the rail. Then multiple regression analysis of the data is carried out to come up with the measurement model equation. The system uses machine learning algorithms to automate regression models built from the input data that have been taken from the inductive sensor, thermocouple, and micrometer readings. Using the regression model algorithm, which is uploaded in LabView, the real-time non-linear data correlation takes place, giving a clearance response signal with improved error from 3.8174% to 3.46646%. Effects of vehicle dynamics and sensor noise are removed from the measurements by designing an infinite impulse digital filter. The filter specifications are obtained by carrying out Fast Fourier Transform of the results from a locomotive multibody dynamic simulation along a curved track and the measurements data from the prototype. Experimental results show effects of temperature on the inductive sensor measured data which are eliminated using a machine learning algorithm. This effect is taken into account to quantify the clearance between the disk and the sensor tip. The precision and accuracy after filtering are determined to be 0.06 Volts and 0.0285 mm, respectively. This system is expected to enhance the real-time and/or online monitoring of the safety of rail vehicles. Also, it can be integrated with Automatic Train Protection (ATP) and the detection of track lateral irregularities from the wheel flange real-time measurement data.

Keywords—*Effect of temperature, FFT, inductive displacement sensor, sensor fusion, data acquisition, machine learning, multibody system dynamic simulation, online filtering, rail vehicle safety, wheel flange wear.*

TABLE OF CONTENTS

LIST OF FIGURES

LIST OF TABLES

ACRONYMS AND ABBREVIATIONS

- ABM: Adams-Bashforth-Moulton method
- BDF: Backward Differentiation Formula
- BTC: Bus Target Counter
- CAD: Computer-Aided Design
- DAQ system: Data Acquisition system
- DFII: Direct form II
- DOF: Degree of Freedom
- DSP: Digital Signal Processing
- EN: Enable signal
- FSM: Finite State Machine
- FPGA: Field programmable gate arrays
- IIR: Infinite Impluse Response
- LRs: Load Registers
- NI: National instruments
- RCL: Resistor capacitor Inductor circuit
- ROM: Read-only Memory
- TC: Temperature coefficient
- MBS: Multi-body System
- ML: Machine Learning
- NMR: Nuclear Magnetic Resonance
- SOS: Second-order Sections
- UM: Universal Mechanism
- WMA: Wheel motoring assembly
- XIN: Input signal

1 INTRODUCTION

1.1. Background

Since its evolution, transit and transportation in terms of loads and passengers became essentials of human life. A large volume of rail transportation is carried out every day, in terms of passengers and freight over long distances which is cheaper compared to road transport [1]. Over the years, railway industries have continuously sought ways to improve operation cost-effectiveness by finding better, efficient, effective technologies as the solutions. Options to achieve this are implementing more efficient, effective, and reliable solutions using advanced technologies. Modern rail systems are becoming increasingly complex due to the high demand for safety, punctuality, comfort, availability, and reliability of the railway and rolling stock. This is so by the emerging of new technologies that need to satisfy all the requirements.

For many years rail and wheel contact has been an underlying aspect of railway systems to the safety of the rail vehicle [2]. Hence its interaction in railway transportation is considered critical for many years. The locomotive wheelsets are a significant component of the running gear since it is one of the most heavily wearing units, often requiring expensive repairs [3]. The uniform motion and safety of the rolling stock largely depend on their performance. This interaction of rail and wheel results in wear and noise considered significant issues in railway transportation depending on many factors. Therefore, this is a major attribute affecting the safety of the rail vehicle, which when not addressed extensively may results in accidents as a result of derailments. There are two main wear zones: the contact area between a wheel flange on a rail gauge and a wheel tread on a railhead. The former causes wear of the wheel flange, influenced by deformation and surface heating from thermal effects. Wear in the wheel flange contact occurs when a railway vehicle moves on curved parts of tracks, realizes tractive, braking efforts, or vehicle moving in a high-speed mode [4]. Furthermore, uneven tracks contribute to the wear of the wheel flange due to the un-uniform motion of wheels. In return, the frictional energy dissipation causes temperature rise on contacting surfaces. Wheel flange wear measurement is a critical operation in monitoring the wheel profile wear, the safety of railway vehicles being the principal attribute [5]. Precise measurement of flange wear is the premise of accurate design and optimization of the inductive displacement sensor.

Machine learning is a branch of artificial intelligence, that uses various algorithms to predict properties of the program that generate responses or outputs from inputs [6]. The algorithms are trained to make predictions from statistical methods, uncovering critical insights within data mining projects [7]. In this research, the data collected from the experiments in the laboratory using inductive and temperature sensors (thermocouple type K) and a micrometer is aggregated together from which a decision key algorithm is developed from the regression model, that updates automatically when new input data are feed into the database. The proposed ML algorithm takes aggregated data over time, which were taken by performing manual measurements. At any time, it can automatically update the regression model coefficients that achieve the correlation coefficient which is within the confidence interval (above 95%). Thus it predicts the clearance between the sensor and the wheel accurately when it is fed by the sensor voltage and temperature. However the ML algorithm does not take into account the effects of vibrations and signal noises, and these effects must be filtered in real-time if the operators must be informed of the status of the vehicle wheel flange at any time. Therefore, an IIR filter is chosen for this task because of its advantage of less delay, less memory requirement, and high resolution at low frequencies.

Multi-univariate regression analysis is used to compute the wheel flange wear using temperature and sensor voltage data. Here the integration of data from the thermocouple and inductive sensor is done by the mathematical regression equation modeled using a machine learning agent. Extensively, all tasks that demand any type of parameter estimation from multiple sources can benefit from the use of data/information correlation methods [8]. Data integration is typically employed for raw data obtained directly from the different sensors. This technique has been extensively employed in multisensory environments to fuse and aggregate data from the different sensors; however, these techniques can also be applied to other domains. The grail of using data integration in multisensory environments is to obtain a lower detection error probability and achieve higher reliability by using data from multiple distributed sources. From the modeled non-linear multi-univariate equation by the machine learning agent, two independent variables are voltage and temperature (inputs from inductive sensor and thermocouples) and one dependent variable which is being predicted (disk clearance). When the system is online, using voltage and temperature inputs, the regression equation predicts the disk clearance, writing it on measurement. In this research, the data prediction methods and techniques are based on the data sources' relation [9]. The complementary criteria are used where the information provided by input sources represent different parts of the scene (inductive sensor output and temperature of the surrounding), hence used to obtain complete information of wheel flange thickness.

This research uses the program package Universal Mechanism (UM) to design and automate the analysis of the locomotive moving along a curved track represented as a multibody system (MBS). In the system, rigid objects are connected utilizing kinematics and force elements. This approach is used to predict what will be expected of a real system given similar input conditions. The significance of carrying out multi-body simulations of the locomotive along a curved track with irregularities is to get the dynamics and vibrations that introduce higher frequencies in flange measurements. UM operates on systems that involve theoretical and applied mechanics in two or three dimensions. The architecture of UM eases the complexity that comes with mechanical systems with a large number of bodies posing a degree of difficulty not only in the analysis of the equations but their generation and even distribution of the structure of the object [10].

Digital signal processing ranks among the most demanding applications of digital design concepts and practices. Signal processing is significant in this work as signals from the flange measurement system are subjected to analyzing, synthesizing, sampling, encoding, transforming, decoding, enhancing, transporting, and archiving. This is done to improve the accuracy and integrity of the response given by the system. The spectral representation and analysis of signals are carried out through mathematical transforms; Fourier series and Fourier transform. The processing entails modifying, reshaping, and transforming the spectrum of the response signal which is filtering in this case [11]. The filtering process here involves selecting a specific desirable band of frequencies and rejecting one or more undesirable bands of frequency components. Lowpass filtering which is adopted in this research selects a band of preferred low frequencies and rejects a band of undesirable high frequencies present in the measured signal.

1.2. Problem statement

Usually, as the railway vehicle moves on a rail during rolling operations, thermal effects are experienced due to friction heating on spinning. In return, the frictional energy dissipation causes temperature rise on contacting surfaces. The temperature rise on the two contact surfaces causes heat transfer by radiation to the inductive displacement sensor, which affects its operation during wheel flange thickness measurement. High temperatures are built up in the flange contact as the rail vehicle moves along curved tracks during braking operations and moves at high speed due to increased friction heating. Different temperature rises are experienced in the flange contact, depend on slip velocity, contact force, and speed of the train. Therefore, the flange surface to be sensed will be having varying temperature jumps as the railway vehicle moves, all factors put in place. An inductive displacement sensor falls under eddy current sensors. Data acquired from eddy current sensors, however, is affected by a large number of variables that include simple conductivity, permeability, geometry, temperatures, and sensor lift-off. Heat transfer through radiation will affect and distort measurement readings of the inductive displacement sensor due to temperature increase affecting the internal parameters of the sensor. Previous methods on the development of an on-board measurement system for railway vehicle wheel flange wear to measure the wheel flange wear using an inductive displacement sensor did not consider the effect of temperature and filtered noises using non-real-time data (filtering after the train is in depot). Therefore, a need arises to study the behavior of the inductive displacement sensor under different temperatures similar to temperature values recorded during these acceleration and braking operations.

1.3. Research questions

Considering different temperatures at the surrounding contact surfaces where the inductive sensor is in range during measurements and online filtering of the real-time measurements, the following are research questions:

i. What are the effects of temperature on the inductive displacement sensor accuracy for wheel flange wear thickness?
ii. How can the effects of temperature on the inductive displacement-based measurements be removed from measurement data?
iii. How can we monitor the temperature of the area between the wheel flange and the sensor?
iv. What is the best method of filtering noises in real-time measurements?

1.4. Contributions

Having an onboard measurement system that takes timely measurements in real-time and then afterward an operator or engineer takes these measurements data for filtering makes the system unreliable. The integrity of the flange measurements is sensitive in the sense that from the temperature effect, vehicle dynamics, and sensor noise, false and inaccurate data will be given. When the system is online with no filters, false alerts or alarms are most likely to be registered, which might noise in the measured data. Dealing with sensitive data in this scenario, non-real-time filtering is not effective. Therefore, a need arises to focus on design and implement real-time methods and systems that work effectively, reliable, giving accurate data on the flange thickness wear at all times of train operation. This by far opens up different methods and approaches in designs to implement the online digital filter for the onboard measurement system.

1.5. Objectives

1.5.1. General objective

To develop real-time methods and systems for wheel flange measurement based on inductive sensing technology under the effect of temperature, vehicle dynamics, and sensor noise.

1.5.2. Specific objectives

- To develop an experimental setup and procedure that will test the effect of temperature on the inductive displacement sensor.
- To develop a multiple regression model that determines the wheel flange thickness from the recorded inductive sensor voltage and temperatures.
- To develop a self-updating multiple univariate regression-based machine learning agent that estimates wheel flange wear from sensor voltage and thermocouples readings.
- To design a digital filter that removes sensor noises and vibrations from the measurement data in real-time.
- To make a CAD drawing for the inductive displacement sensor support structure.

1.6. Significance of the research

Operations and maintenance of railway systems are critical for the realization of safe operations of trains all the time. The integrity of flange thickness measurements is the core entity of this research. Focusing on the developed onboard measurement system using an inductive sensor with its convenient features to improve its performance in terms of reliability, accuracy, efficiency, and effectiveness is the goal of this research. The knowledge that inductive sensors have temperature drift problems not considered in the previous research and noises in the measurements filtered in non-real-time data, integrity, and reliability of flange measurements is compromised. Effects of these are accidents from derailments. Therefore, the importance of this research is improving the reliability of wheel flange measurement systems, enhancing the safety monitoring of rail vehicles by studying the effects of temperatures on the inductive sensor, eliminating distortion of measurements, and employing online filtering of these measurements.

1.7. Motivation of research

Derailments of rail vehicles are catastrophic, which calls for an affordable, reliable measurement system with high accuracy and precision to monitor the wheel flange thickness and act accordingly during danger. Focusing on non-contact measurement methods for wheel flange wear, the inductive displacement sensor rendered suitable features for low cost, high precision, and higher accuracy. From previous research (Turabimana and Nkundineza, 2020) using inductive displacement sensors, wheel flange measurements were acquitted in real-time, but effects of temperature on the inductive sensor were not considered and noises were filtered in non-real-time data. The safety of a rail vehicle is assured if all these problems in this system are fully addressed as accidents happening because of the lack of an affordable, accurate, and reliable measurement system. Major challenges on available measurement systems are the high cost in terms of equipment installation and maintenance, especially in the third world countries across the globe.

1.8. Research methods

The specific objectives outlined need the following methods to achieve them: literature review, experiment method by a prototype, Multi-body system simulations, digital filter design, computer-aided drawing of sensor support structure mechanism. The following flow chart in figure 1-1 below shows the methods to achieve this research.

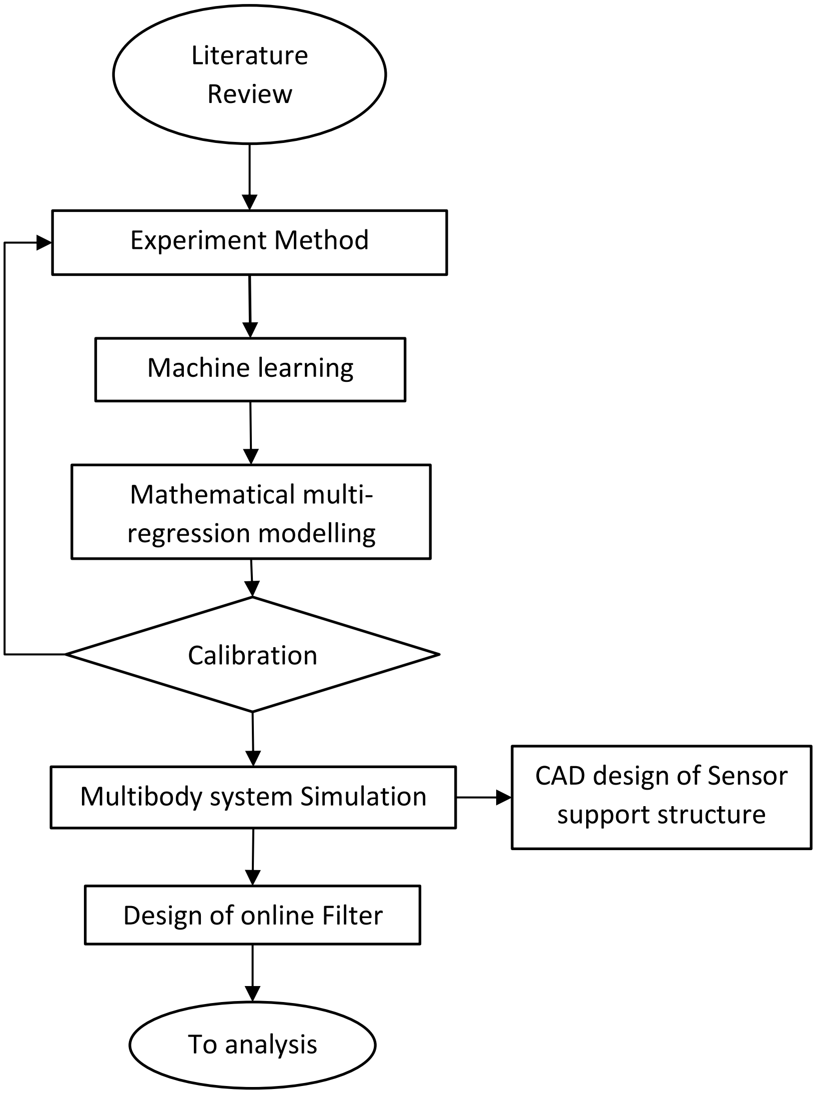

Figure 1-1. Flow chart of research methods

2 LITERATURE REVIEW

2.1. Temperatures in the contact zone between a wheel flange and a rail gauge

In the realization of tractive efforts by a railway vehicle with slip presented between contact surfaces of a wheel and a rail, interaction forces between surfaces are acting, accompanied by the release of heat energy in the contact zone. Energy processes act by using big specific loads on small contact surfaces providing high energy concentrations and thus gives a jump in temperature. In the wheel flange/rail gauge contact, the values of slip velocities are higher than that of wheel-rail contact, which explains a jump in temperature [4]. Numerous researches have been done on determining temperature build-up in the flange contact considering the track geometry (straight track and curved part of tracks with different radius), contact force, train speed, and slip velocity. However, the flange models for the temperature calculations are still at the stage of development. Sundh and Olofsson [12] calculated average and maximum temperatures in the contact, but this approach cannot be accurate if necessary to apply results to the contact model between a wheel and a rail. Figure 2-1 below shows the dimensions of the contact zones. Table 2-1 presents the dimension of the contact area surfaces.

Table 2-1. Distribution of temperature in the flange contact for data presented

V, Km/h	Dimension of contact area			
	Wheel tread and rail head		Flange contact	
	2a, mm	2b, mm	2a, mm	2b, mm
Curved part of the track with a radius of 600m				
60	14.3	14.8	9.9	6.3

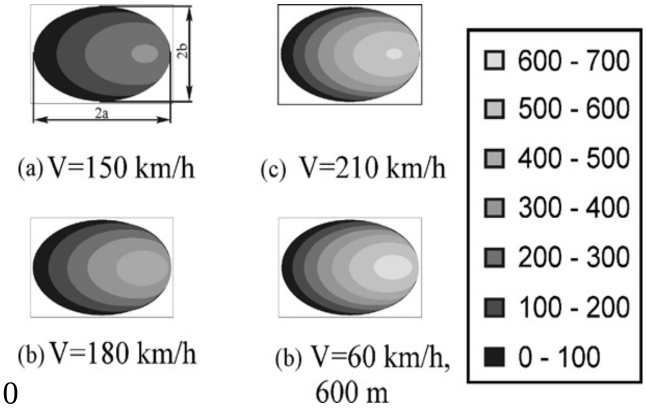

0

Figure 2-1. Temperature built up in the flange contact

Our case study is the Ethio-Djibouti mainline, the maximum speed of the passenger and freight railway vehicle is 120km/h and 80 km/h respectively. However, the track has lots of irregularities, hence the speeds of both the passenger and freight train are reduced to 80km/h and 60km/h respectively. The rail vehicle speeds on curved tracks with different radius, reduce from the maximum speeds. Temperatures registered in the flange contact ranges from 0 to 120℃ and 0 to 60℃ between the wheel tread and railhead. In some scenarios during braking, accelerations, those temperatures jump to higher values from 200℃ are lowered using special coolants.

2.2. Existing on-board wheel flange thickness measurement technologies

There are existing flange measurement methods, classified into contact and non-contact methods. The contact methods involve manual measurement techniques using handheld tool devices [13] and; using electronic wheel profile meters when the rail vehicle is at the depot [14]. Non-contact measurement methods are divided into two categories trackside and onboard measurement devices. The trackside electronic devices, ultrasonic sensors, lasers, and image processing devices process real-time measurements only when the train passes by them [15]–[17]. The limitation of the trackside devices is that at different locations, there are no measurements recorded. It is disadvantaged and expensive to install a continuous trackside measurement device to monitor the wheel flange wear in terms of reliability. The onboard measurement devices include the use of lasers, ultrasonic, and inductive devices [5], [18], [19]. For the computer vision-based systems with cameras, laser sensors, and image processing technologies taking flange measurements while the train is in operation, there is a cost-effect in equipment and installation along the track.

The current developed onboard flange measurements method based on inductive sensing technology, in the other case, is simple, affordable, and with high accuracy and precision [5]. Therefore such a device would work well for rail vehicles that do not experience increased temperature at the wheel flange, such as trams and metro. They run at low speeds and use a disk braking system on the axle. On the other hand, mainline trains in the Ethio-Djibouti line run at higher speeds and usually use brake shoes on the wheel, which increases the wheel temperature. Furthermore, noises were filtered in non-real-time data.

2.3. Overview of inductive sensors

Inductive sensors are one of the non-contacting displacement measuring systems that are nowadays preferred for industrial position feedback at actuators [20]. In this application, the inductive displacement sensor is used to determine the clearance gap between the sensor tip and the wheel flange surface. Due to its flexibility, reliability, ruggedness, compact design, with high accuracy and precision, it is ideal for wheel flange measurements and also opens up areas for new implementations. In general, inductive sensors are devices using the principle of electromagnetic induction to detect objects. On excitation, the inductor develops a magnetic field in which a current flows through the inductor as the magnetic field changes through it. When a metal object is near the changing magnetic field, eddy currents induced in the object sets up a new magnetic field opposing the original magnetic field. The net effects being changing the inductance of the coil. This effect is used to detect metal objects that interact with the produced magnetic field. On the other hand, non-metallic substances such as dirt or fluids do not interact with the magnetic field. Hence an inductive sensor can operate in both wet and dirty conditions [21].

2.3.1. Operation principle of inductive sensors

The inductive sensors are based on Faraday’s law of induction. The variation of the magnetic flux Φ through N turns circuit will induce a voltage e which is as follows:

$$e = -N \frac{d\Phi}{dt} \qquad (2.1)$$

and is expressed in a similar way as:

$$e = -N \times S \frac{d\mathrm{B}}{dt} \qquad (2.2)$$

where e is the induced voltage, Φ magnetic flux, B is the induced magnetic field and S is the section over which the magnetic field is induced.

$$B = \frac{\mu_o i}{2\pi d} \tag{2.3}$$

where μ_o is the permeability of the free space, i is the current in the coils and d is the distance between the sensor tip and metal target. The ambient temperature change will cause the material electromagnetic performance change for the conductive and permeability varies with temperature. Making the assumptions that the induced magnetic field B is homogeneous over a section S, the n the Magnetic flux will be expressed $\Phi = B \times S$. Figure 2-2 below shows the construction of the electric circuit of the inductive sensor depicting its principle of operation.

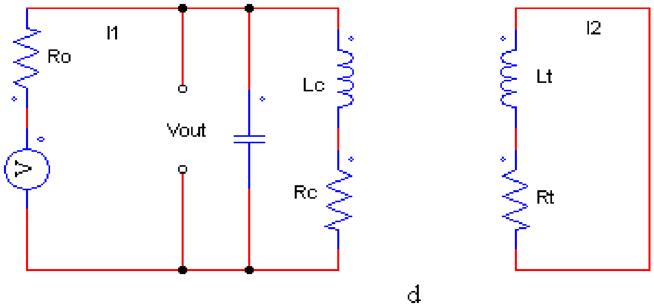

Figure 2-2. Electric circuit model of the inductive sensor; d is the clearance in mm.

Kirchoff voltage law is used to show the relationship between equivalent circuit parameters and output signal [22].

$$R_c I_1 + j\omega L_c I_1 - j\omega M I_2 = V_{out} \tag{2.4}$$

$$R_t I_2 + j\omega L_t I_2 - j\omega M I_2 = 0 \tag{2.5}$$

The equivalent impedance R, inductance L and impedance Z of the sensor is derived from equation (2.4) and (2.5).

$$R = R_c + \frac{\omega^2 M^2}{{R_t}^2 + (\omega L_t)^2} R_t = R_c + R_e \tag{2.6}$$

$$L = L_c - \frac{\omega^2 M^2}{{R_t}^2 + (\omega L_t)^2} L_t = L_c - L_e \tag{2.7}$$

$$Z = R + j\omega L = [R_c + R_e] + j\omega[L_c - L_e] \tag{2.8}$$

The change of equivalent impedance is as a result of equivalent resistance R and equivalent inductance L variation while R and L are determined by the clearance between the sensor coil and target (M), exciting voltage frequency $(f, f = 2\pi\omega)$, coil inductance (L_c) and coil resistance (R_c) as shown in equations (6) and (7). R_t and L_t is the equivalent resistance and inductance of induced eddy current. In certain conditions, f , L_c, and R_c are constants, therefore the equivalent impedance becomes the univalent function of distance (d).

2.3.2. Applications as proximity sensors

Inductive displacement sensors are non-contact electronic proximity sensors used for the positioning and detection of metal objects. The sensing range is dependent on the type of metal being detected. For example, ferrous metals (iron and steel) allow for a more extended sensing range, while nonferrous metals, such as aluminum and copper, may reduce range by up to 60 percent. Since the output of inductive sensors has two possible states, it is sometimes referred to as an inductive proximity switch [23], [24].

The sensor consists of an inductor coil or detector coil, which is a magnet wire wound around a high magnetic permeability core. The winding may or may not have feedback tap some number of turns from one end of the total winding. The inductor coil is connected parallel to a capacitance to form a tuned frequency oscillator tank circuit. In concurrence with voltage or current gain devices like a transistor or operational amplifier, this forms a tuned frequency oscillator. When excited, the resulting oscillation is a high-frequency alternating electric current in the coil with a constantly changing magnetic field able to induce eddy currents in the metal target (wheel flange surface). The closer the target is and the high conductivity, the greater the induced eddy currents and the more effect the resulting opposing magnetic fields have on the magnitude and frequency of the oscillation. This magnitude is reduced as the load increases in a non-magnetic conductor like aluminum because the induced field in the target is opposite that of the source induction field, lowering net inductive impedance and simultaneously tuning the oscillation frequency higher. But that magnitude is less affected if the target is a highly magnetically permeable material, like iron, as that high permeability increases the coil inductance, lowering the frequency of oscillation. From this, a change in oscillation magnitude may be detected with a simple amplitude modulation detector that passes the peak voltage value to a small filter producing a reflective DC voltage value. A frequency change may be detected by several kinds of frequency discriminator circuits, like a phase lock loop detector, to see the amount of frequency shift and its direction. From this, either the magnitude or amount of frequency change can serve to defined a proximity distance at which the sensors go from on to off, or vice versa.

2.4. Literature review on the effects of temperature on the inductive sensor

The inductive method is suitable for wheel flange measurements; its simple structure, low cost, easy installation, achieves high precision and accuracy [25]. However, the measurement signal of the inductive sensor has temperature drift problems, inevitably affected by temperature variation for measuring principle [26]. Moreover, they have a much larger temperature coefficient (TC) because of the high TC of metal resistivity, limiting their application in high precision displacement measurement systems [27]. In application, the effect of temperature on the inductive sensor has been studied in turbines, other industrial applications but not yet for railway industries. Turimbana et al [5] used the inductive displacement sensor to measure the wheel flange wear successfully, hence achieved high accuracy and precision compared to existing multicamera and onboard laser-based systems. The method did not consider the effect of temperature and filtered noises using non-real-time data (filtering after the train is depot).

Over recent years, different methods to reduce effects temperature on the inductive sensor, such as increasing working frequency, use of temperature sensors to compensate drift, use of compensation integrated electronics, and use of differential probe structures [28]. Lyu et al [22] used a temperature compensation circuit added in the output stage of the sensor to eliminate the temperature drift of the inductive sensor from $20℃\ to\ 500℃$. Experimental results verified that the designed high-temperature eddy current sensor had good output sensitivity and linearity within the temperature range variation, with practical drift eliminating properties. Its limitation is that it requires an extra temperature compensation circuit that adds to the hardware. The experimental research of Wang et al. [29] proposed a new method to reduce thermal drift of eddy-current sensor (ECS) by two orders of magnitude. Theoretical analysis showed that a well-designed bridge would help decouple two vectors related to the resistance and inductance variation of the sensing coil of ECSs. Experiments showed that resistance variation has a considerably larger coefficient with temperature change than inductance variation. This self-temperature compensation method for ECS is simple, low cost, universal, very practical, and with competitive advantages in most applications. The limitation of this correction method is that the rate of temperature change should be less than $1℃/h$, which is necessary for most (sub-) nanometer resolution displacement measurements.

Zhao et al [30] focused on the eddy current sensor design and validation for reducing temperature effect. Simulation and experiment methods were both used to determine optimal sensor structure parameters and materials. The inductive sensor was encapsulated by a planar coil made of platinum wire with a maximum sensing range of 5mm, excited by a high-frequency AC signal. The planar platinum wire can withstand high temperatures in the furnace. However, the limitations of a short sensing range of 5mm while exciting it with an AC signal and platinum itself are expensive. In this research, an analog inductive displacement sensor with a sensing range of 10mm excited with a 25Vdc signal [31] is used for wheel flange wear measurement considering thermal effects. This research aims to improve the accuracy and precision of the inductive displacement sensor used in wheel flange wear measurement.

2.5. Overview to IIR digital filter design

This system is designed to be a recursive discrete-time system, whose output at any instant depends on a set of values of the input as well as a set of values of the output. A recursive discrete-time system, known as the infinite impulse response whose output at any instant depends on a set of values of the input, and a set of values of the output is considered. IIR filters are useful for high-speed designs because they typically require a lower number of multiply compared to FIR filters. They can be designed to have a frequency response that is a discrete version of the frequency response of an analog filter. These filters are very sensitive to filter coefficients quantization errors that occur due to using a finite number of bits to represent the filter coefficients.

The response of a fairly general recursive, linear time-invariant, discrete-time system is given by [32]

$$y(nT) = \sum_{i=-K}^{M} a_i x(nT - iT) - \sum_{i=1}^{N} b_i y(nT - iT) \tag{2.9}$$

That is, if instant nT were taken to be present, then the present response would be a function of the past M values, the present values, the future K values of the excitation as well as the past N values of the response. The dependence of the response on several past values of the response implies that a recursive discrete-time system must involve feedback from the output to the input. The order of a recursive discrete-time system is the same as the order of its difference equation, as in a non-recursive system, and it is larger if M+K and N+K. Approximation methods for IIR filter design differ quite significantly from those used for the design of non-recursive filters, the reason being that in the first case the transfer function is a ratio of polynomials of z whereas in the second case it is polynomial of z^{-1}.

In recursive filters, the approximation problem is usually solved through indirect methods. First, a continuous-time transfer function that satisfies certain specifications is obtained using one of the standard analog-filter approximations [33]. Then a corresponding discrete-time transfer function is obtained using one of the following methods [1-9]:

- Invariant impulse-response method
- Modified version of method 1
- Matched-z transformation
- Bilinear transformation

2.6. Literature on real-time IIR digital filtering

Digital filters are used as pre-processing tools in any application to assure attenuation of undesired frequencies during the introduction of a nominal frequency. Advantages of digital filters over analog filters are improved baseline performance, better dynamic range, and improved overall sensitivity [34]. There are several technologies on software and hardware implementation for the digital filers, with different designs depending on the architecture chosen. Over the past years, there are numerous researches on software and hardware implementation for IIR digital filters. Woods et al. [35] designed a high-performance IIR digital filter chip that indicated circuit architectures based on the most significant bit first arithmetic, which offers considerable potential for full-scale development. Complexity in design for a higher order of the filter. Delta operators realizing digital filters gained interest due to their excellent finite word length performance under sampling rate. Kauraniemi et al. [36] focused on round-off noise analysis, where the direct form II transposed delta structure showed the lowest quantization noise levels at its output. The DFII outperformed both the conventional direct-form (delay) structures and the state-space structures for narrow-band lowpass filters regarding output roundoff noise. There was excellent filtering of noise, but it came with additional implementation complexity compared to delay realization. Dehner, [37] gave design procedures for cascades with second-order sections (SOS) indirect form and state-space form. Pairing and ordering of poles and zeros within the cascades were determined using dynamic programming. Results depicted that according to the transfer functions, the appropriate choice of SOS forms with optimizing the pairing and ordering is helpful for different hardware designs.

Islam et al. [38] proposed an architecture of a programmable digital IIR filter based on XILINX FPGA board, in which gate-level design analyzes the impulse response of the filter. It is disadvantaged when realizing higher-order filters as the speed, cost, and flexibility are affected by complex computations. Second-order IIR filters on FPGAs are the ones to go for since field-programmable gate arrays give enhanced speed because hardware implementation of lots of multipliers can be done effortlessly on FPGA, limited in the case of programmable digital processors. There are better performances to the standard filter structures in processing speed, cost, and power consumption. Therefore, these designed filters based on FPGA can work for the real-time processing of any digital signal. Chen and Wang [39] presented a simple and more efficient method for IIR digital filter design based on Butterworth analog filter using the invariant impulse method. The design involved: designing a non-quantitative IIR filter using MATLAB; converting the designed IIR filter of M language into hardware description language using AcceIDSP; finally verifying by timing the simulation and synthesizing the IIR design using ISE the current 10.1 of Xilinx. This design method by far overcomes the ambiguity of IIR filter design with hardware description language directly. Hence, a cheaper, higher sampling rate, real-time IIR design with AcceIDSP. Hourani et al. [40] utilized concepts inherent to both second-order sections (SOS) and state-space models to implement IIR filters in hardware. They compared the performance of the state space hardware model to the conventional IIR filter implementation using Spartan 3 XC3S400-4FG320 FPGA and a two-fold increase in hardware throughput using the state space SOS models was observed. Toledo-Pérez et al. [41] filtered noises using an IIR digital filter FPGA for Myoelectric signals. Real-time digital filtering has been applied to various application examples in NRM spectroscopy due to the availability of fast DSPs [42].

The online digital IIR filter is modeled using Matlab/Simulink and simultaneously using LabView design for this research. Simulation of the two models is verified when the system is online, as the accuracy of the filtered results is determined. Reliability, accuracy, and integrity of the flange measurement data is the primary attribute to the safety of the rail vehicle. This research presents an analog inductive displacement sensor with a sensing range of 10mm excited with a 25Vdc signal, used for wheel flange wear measurement considering thermal effects. The research aims to study the effect of temperature of this inductive sensor used for wheel flange wear measurements, which were not considered in the previous research.

Furthermore, data prediction techniques are used to reduce and eliminate the measurement drift. A Multi-regression model is developed from an array of data taken from the manual measurement readings from the inductive sensor thermocouple and micrometer, which is reproduced automatically by a machine learning algorithm. In the Labview program, arithmetic operations and Matlab scripts are used to write the regression model for data fusion operations in which the run-time of two responses is compared. The error of the response to the actual response is measured. A low-pass digital infinite impulse filter is used to filter the noises present in the measurement. Measurement data taken at temperatures up to 98℃ are presented. Machine learning agent is implemented to improve the dynamics of the system through optimization, reducing human interaction. Multibody simulations using the universal mechanism software for the vibration and dynamic analysis of locomotive along a curved track are done. Finally, an online digital infinite impulse response filter is designed in LabView and Simulink to remove all noises from the system and train vibrations.

3 METHODOLOGY

The work presented in this research consists of measuring the wheel flange wear in terms of the clearance between the sensor tip and wheel flange surface. The flow chart of the system Data structure is presented in the block diagram below in Figure 3-1. Experiments through prototyping are carried out, involving manual measurements from which all raw daily data taken are written in an excel file. From the aggregated raw data, a multi-univariate regression model is reproduced automatically and uploaded to the data acquisition software (Labview program). Then during data acquisition, voltage and temperature from the inductive sensor and thermocouple, are integrated using the uploaded regression model and a clearance response is estimated which is of good confidence of 95% and above.

The accuracy of the response is continuously checked to verify the minimization of the flange measurements. Multibody simulations of the locomotive are carried out to get the vibrations from the dynamics of the vehicle in terms of yaw, lateral and vertical displacements of the bogie and wheelsets. The track geometry is designed with lateral irregularities, which translate to high oscillations in the vehicle dynamics. Since the machine learning agent does not consider the noises from the sensor and vibrations from the train dynamics, a multiple Fast Fourier transform analysis of the unfiltered measurements with the multibody simulation results are correlated together. Afterward, suitable filter design specifications are obtained, and the filter is designed. Using software implementation, the filter transfer function is written in the LabView program, and the online filtering process is tested. The exact online measurements are passed in a SIMULINK digital filter model where the finite differential equation is used and the simulation is done alongside using LabView.

Accuracy of then both filtered measurements from the LabView filter design and Simulink model are determined. The delay in the online filtered measurements is checked, and from that, conclusions and recommendations are made. With the coordinate position of the sensor selected in the locomotive design, the displacements relative to the coordinate of the sensor are studied when the vehicle is moving along a curved track geometry with a specified radius. From this, a suitable sensor support structure mechanism is designed from which its purpose is to maintain the coordinate system of the sensor with all the train dynamics inclusive and keep the sensing range intact.

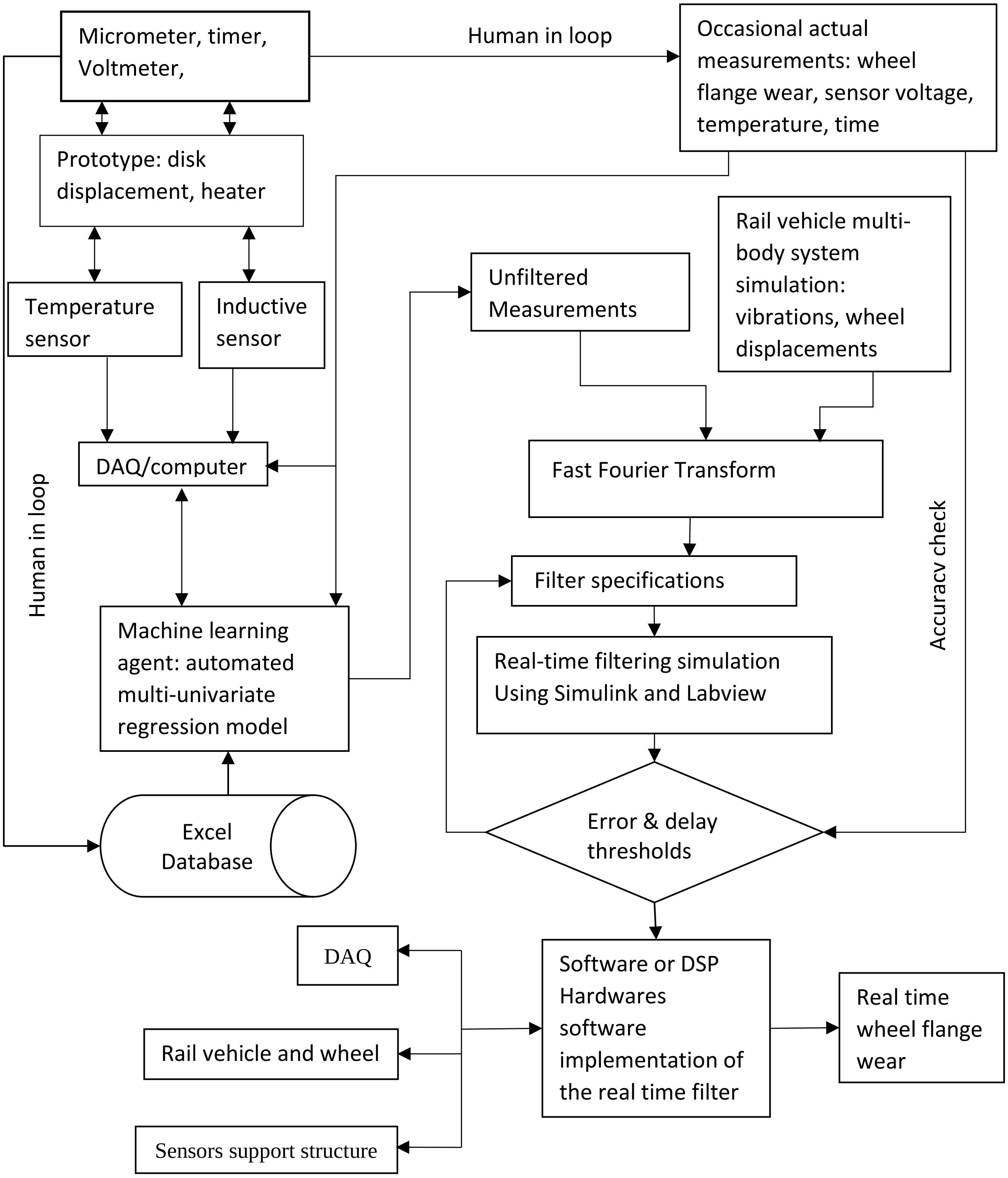

Figure 3-1. Data flow of research methods

3.1. Methods of Data Acquisition

The onboard wheel flange measurement system uses an inductive-based method sensing technology. The system picks up signals using the sensors in place, processes them, and generates output signals, transforming them into comprehensive data, which prompts alarms and warnings. An inductive sensor measures wheel flange, and thermocouple type K is used to record temperatures of the surroundings as a result of heat by radiation that distorts measurement readings data. The following methods are used:

3.1.1. Experimental Setup

For data collection and testing of the system, a prototype mimicking the flange measurement system is set up (see Figure 3-2). The setup consists of: an inductive displacement sensor, a calibration target which is a disk mimicking a train wheel flange; a micrometer screw gauge coupled to the shaft of the disk; a temperature sensor (thermocouple), hot air supply (electric blower), DAQ system, a user interface (LabView) and connecting wires. Figures 3-2 below show the experiment prototype set up to carry out multiple tests.

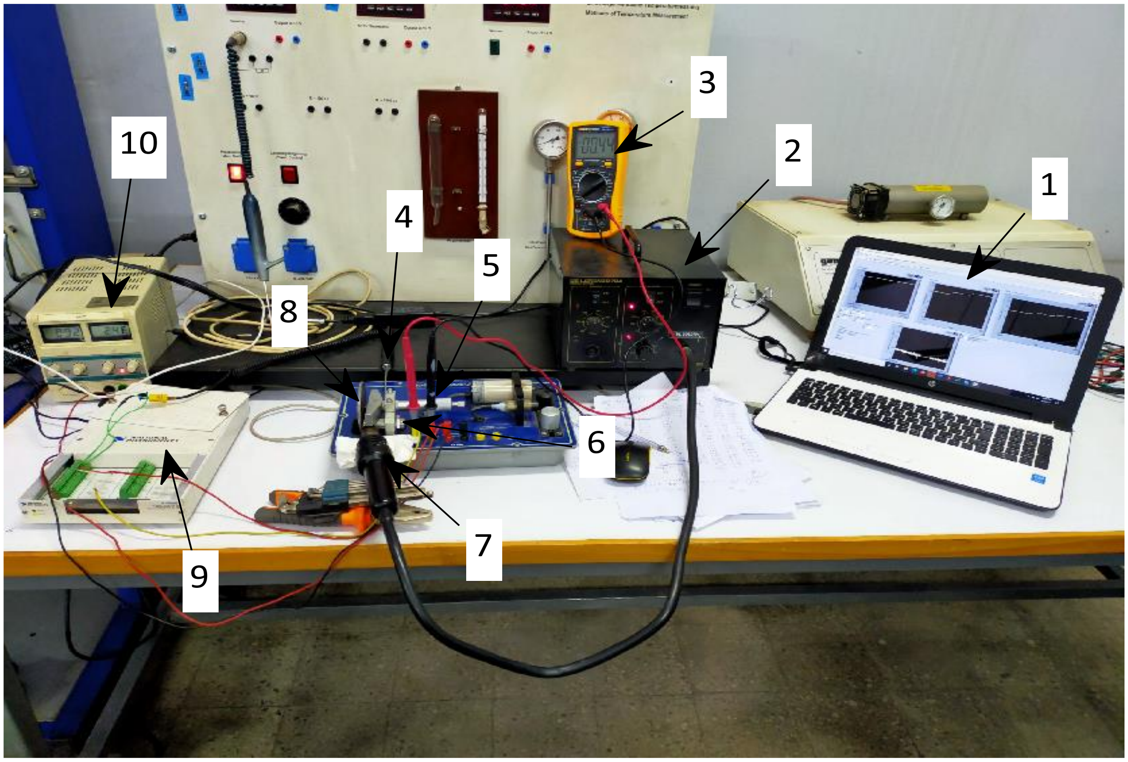

Figure 3-2. Experiment setup prototype: user interface (1), heat blower generator (2), voltmeter (3), thermocouple (4), micrometer (5), inductive sensor (6), hot air nozzle (7), steel disk (8), data acquisition system (9), DC power supply (10)

A micrometer screw gauge coupled to a steel disk shaft measures the disk clearance gap from the sensing tip of the inductive displacement sensor. Measurement data readings are taken moving the disk laterally using a micrometer gauge couple to the shaft fixed to the steel disk. The disk clearance is proportional to the output signal (voltage) of the inductive sensor. An electric heat blower with adjustable heat temperatures from $0℃\ up\ to\ 500℃$ produces consistent heat through radiation to the steel disk and the sensor casing. A temperature sensor (thermocouple type K) monitors the surrounding near the sensor shield and disk. In data collection, we have two-stage processes. Stage 1 involved taking measurement readings using a micrometer, thermocouple, and voltmeter manually which are considered to be reference data since they have fewer random errors. Repeated multiple tests are carried out daily at different temperatures, $19℃\ to\ 98℃$. Stage 2 involves data acquisition to automatically measure data from the inductive sensor and thermocouple, writing it to a computer file. The LabView software is used with the data acquisition interface and a NI USB 6221 board to record the sensor readings.

3.1.2. Multiple-regression modeling

Data collected at experiment stage one is put together in ascending order about the clearance. Using MATLAB, the large amount of data collected manually is fitted to a 3-axis plot, with clearance being a dependent variable, while voltage and temperature independent variables. A multi-regression model that predicts clearance as a function of sensor output voltage and temperature is formulated. Clearance (d) is in millimeters, voltage v in volts, and temperature in degree Celsius. A non-linear multi-regression model of second-order with a good correlation factor is considered [43]:

$$d = a_o + a_1 V + a_2 T + a_{11} V^2 + a_{22} T^2 + a_{12} VT + \epsilon \qquad (3.1)$$

where ϵ is the residual terms of the model. To estimate the parameters of more complex models, linear algebra methods are used to make the computation more efficient. The coefficients $a_o, a_1,.., a_{22}$ are obtained by solving error minimization. Taking partial derivatives of equation (3.1):

$$\frac{\partial}{\partial a_o} \sum_{i=1}^{N} [d_i - (a_o + a_1 V_i + a_2 T_i + a_{11} V_i^2 + a_{22} T_i^2 + a_{12} V_i T_i)]^2 = 0 \qquad (3.2)$$

$$\frac{\partial}{\partial a_1}\sum_{i=1}^{N}[d_i-(a_o+a_1V_i+a_2T_i+a_{11}V_i^2+a_{22}T_i^2+a_{12}V_iT_i)]^2=0 \tag{3.3}$$

$$\frac{\partial}{\partial a_2}\sum_{i=1}^{N}[d_i-(a_o+a_1V_i+a_2T_i+a_{11}V_i^2+a_{22}T_i^2+a_{12}V_iT_i)]^2=0 \tag{3.4}$$

$$\frac{\partial}{\partial a_{11}}\sum_{i=1}^{N}[d_i-(a_o+a_1V_i+a_2T_i+a_{11}V_i^2+a_{22}T_i^2+a_{12}V_iT_i)]^2=0 \tag{3.5}$$

$$\frac{\partial}{\partial a_{22}}\sum_{i=1}^{N}[d_i-(a_o+a_1V_i+a_2T_i+a_{11}V_i^2+a_{22}T_i^2+a_{12}V_iT_i)]^2=0 \tag{3.6}$$

$$\frac{\partial}{\partial a_{12}}\sum_{i=1}^{N}[d_i-(a_o+a_1V_i+a_2T_i+a_{11}V_i^2+a_{22}T_i^2+a_{12}V_iT_i)]^2=0 \tag{3.7}$$

After differentiation and algebraic manipulations of equations (3.2),(3.3),…,(3.7) a 6 by 6 matrix equation (3.8) is formed to solve for the coefficients:

$$\begin{bmatrix} a_o \\ a_1 \\ a_2 \\ a_{11} \\ a_{22} \\ a_{12} \end{bmatrix} = \left[\sum_{i=1}^{N}\begin{bmatrix} n & V_i & T_i & V_i^2 & T_i^2 & V_iT_i \\ V_i & V_i^2 & \mathrm{V}_i\mathrm{T}_i & {V^3}_i & V_iT_i^2 & V_i^2T_i \\ T_i & \mathrm{V}_i\mathrm{T}_i & T_i^2 & V_i^2T_i & T_i^3 & V_iT_i^3 \\ V_i^2 & {V^3}_i & V_i^2T_i & V_i^4 & {V^3}_iT_i^2 & {V^3}_iT_i \\ T_i^2 & V_iT_i^2 & T_i^3 & V_i^2T_i^2 & T_i^4 & V_iT_i^3 \\ V_iT_i & V_i^2T_i & V_iT_i^2 & {V^3}_iT_i & V_iT_i^3 & V_i^2T_i^2 \end{bmatrix}\right]^{-1} \begin{bmatrix} \sum_{i=1}^{N} d_i \\ \sum_{i=1}^{N} d_iV_i \\ \sum_{i=1}^{N} d_iT_i \\ \sum_{i=1}^{N} d_i\,V_i^2 \\ \sum_{i=1}^{N} d_iT_i^2 \\ \sum_{i=1}^{N} d_iV_iT_i \end{bmatrix} \tag{3.8}$$

The regression coefficient r is given by,

$$r_{VT}=\sqrt{1-\frac{Q_R}{Q_M}} \tag{3.9}$$

Where,

$$Q_R=\sum(d_i-(a_o+a_1\mathrm{V}+a_2\mathrm{T}+a_{11}V^2+a_{22}T^2+a_{12}VT+\epsilon))^2$$

$$Q_M=\sum(d_i-\bar{d})^2$$

Coefficients that suffice r, greater or equal to 0.975 have good confidence of 95% and thus the equation is selected. Then using this equation comes in stage 2 of the experimental procedure. The data collected during daily multiple tests at adjustable disk position from 0mm to 10.5mm, at different temperatures was fitted to a 3D axis plot, where clearance is the dependent variable while temperature and sensor output voltage are independent variables. Fitting a curve of best fit, a second-order polynomial multi-regression curve was fitted to the large chunk of measured data. Figure 3-3 shows the fitted data in a 3-axis plot.

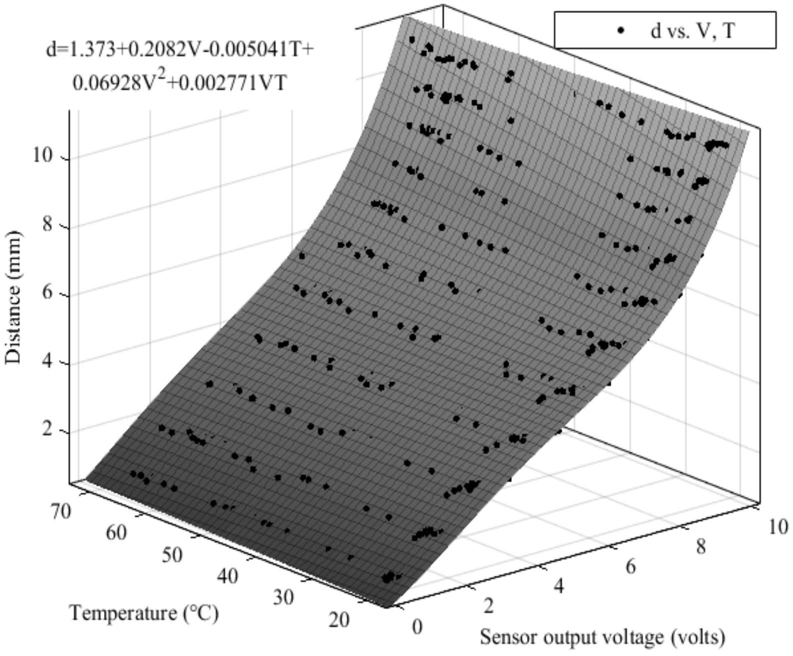

Figure 3-3. Curve fitting of the fused data

A second-order polynomial regression model,

$$d = 1.373 + 0.2082V - 0.005041T + 0.06928V^2 + 0.002771VT \tag{3.10}$$

whose coefficients are with good confidence of 97.09%, with adjusted $r_{V,T}^2$ = 0.9709, or $r_{V,T}$ = 0.9853 was found.

3.1.3. Real-time clearance measurement using an inductive sensor, thermocouple, and data acquisition system

In the LabView software, an algorithm is executed to estimate the disk clearance in mm from the input data of inductive displacement and temperature sensors through a regression equation. As shown in Figure 3-4, a calibration equation is obtained using multi regression analysis using two dynamic input variables that is, an output voltage of the inductive sensor and the temperature from a thermocouple of type K. The program reads actual disk displacement in mm as the output

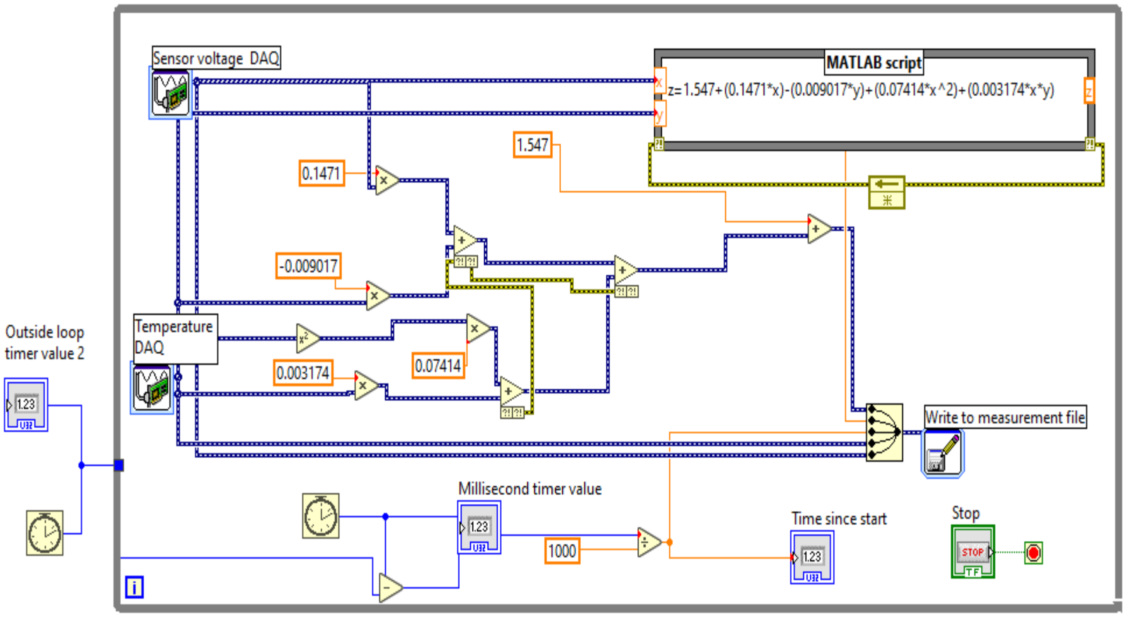

```
z=1.547+(0.1471*x)-(0.009017*y)+(0.07414*x^2)+(0.003174*x*y)
```

Figure 3-4. LabView program showing the data integration process

To ensure the run-time of the system is minimum as possible to realize effective real-time measurement, MATLAB script node and numerical operators completing the equation were used to write the multi-regression equation having two inputs: the dynamic data of temperature and voltage. The response is the dynamic data of clearance, in which d1 represents the clearance response from the numerical operators shown in the Labview program and d2 the clearance response from the MATLAB script (see Table 3-1).

Table 3-1. Run-time check of response

d1(mm)	d2(mm)	d1(mm)	d2(mm)
1.768844	1.884958	1.822104	1.965721
1.763462	1.879061	1.831405	1.983979
1.761364	1.876915	1.834452	2.005647
1.744545	1.866896	1.846918	2.006709
1.768581	1.888242	1.872819	2.027542
1.820492	1.964325	1.857446	2.019315

It was found out that the run-time of MATLAB script response is lesser than that of numerical operators. Delays were registered in the numerical arithmetic operators. Therefore, a script standalone android application executing similar operations as MATLAB script can be embedded on the system to achieve faster run-time.

3.1.4. Machine learning agent

Dynamic changing of the daily measurements with time is seen by the repeatability tests done on the measurements at different temperatures. Therefore, a machine learning agent is built to train the system on the behavior of measurements under all different conditions and where all the manual measurements are written in an excel file database. The non-linear regression describes a non-linear relationship in the experiment data collected in stage 1. Machine learning methods are used for non-parametric linear regression [44]. The parametric regression models the dependent variable (clearance called the response) to combine two independent variables (voltage and temperature). This model is of a single response variable which is the clearance. The non-linear parameter estimates are determined using an iterative algorithm. The multiple daily data collected in stage one of the experiments are written in an excel file and updated regularly when new measurements are taken. A MATLAB code modeling a non-linear multi-regression model from the data is executed. The model is of the form [43]:

$$d_k = \sum_{i=0}^{m} \sum_{j=0}^{n} a_{ij} V_k^i T_k^j + \epsilon_k, \qquad k = 0,1, \dots N \qquad (3.11)$$

where d_k is k^{th} observation in N measurements (measurement of the clearance between the sensor tip and the wheel flange surface), a_{ij} represent coefficients of the regression model to be solved, m and n are the orders of the regression model. V is N-by-1 voltage matrix observations; T is an N-by-1 temperature matrix observations; and ϵ is an N-by-1 vector of independent, identically distributed random measurement errors. The algorithm solves the coefficients by searching coefficients that automatically minimize the measurement total squared errors. It means

$$\frac{\partial}{\partial a_{pq}} \sum_{k=1}^{N} \epsilon_k^2 = 0, \qquad (3.12)$$

with $p = 0,1,2,..m$ and $q = 0,1,2,..n$

Using Equation (3.11) for differentiation, Equation (3.12) is equivalent to [43]:

$$\sum_{k=1}^{N} d_k V_k^p T_k^q = \sum_{k=1}^{N} \sum_{j=0}^{n} \sum_{i=0}^{m} a_{ij} V_k^{i+p} T_k^{j+q} \qquad (3.13)$$

with $p = 0,1,2,..m$ and $q = 0,1,2,..n$

Through a set of resulting equations the coefficients $a_{ij}$are solved. The algorithm continuously checks the regression coefficient r of the regression model. Then conditions are stipulated as: if r is equal to or greater than 0.975 (good confidence of 95%), then upload the regression model and save it in a file. Moreover, if the adjusted r is less than 0.975, increase the order of the regression model by adding more coefficients till the condition is satisfied. The regression model file stored in the LabView directory is updated every time data is added to the excel file. The Matlab script in the LabView program calls this file with the regression equation, and the algorithm executes step-wise instructions. From the experimental data with added disk measurements at temperature up to 98℃, a second-order regression model was found to be:

$$\mathrm{d} = 1.16 + 0.3672\mathrm{V} - 0.0036\mathrm{T} + 0.05812V^2 + 0.0006618VT \qquad (3.14)$$

whose coefficients are with good confidence of 97.06%, with adjusted $r_{V,T}^2$ = 0.9706, or $r_{V,T}$ = 0.9852. Figure 3-5 shows the curve fittings of the added data, whose regression equation is updated in the MATLAB Script (see Figure 3-6).

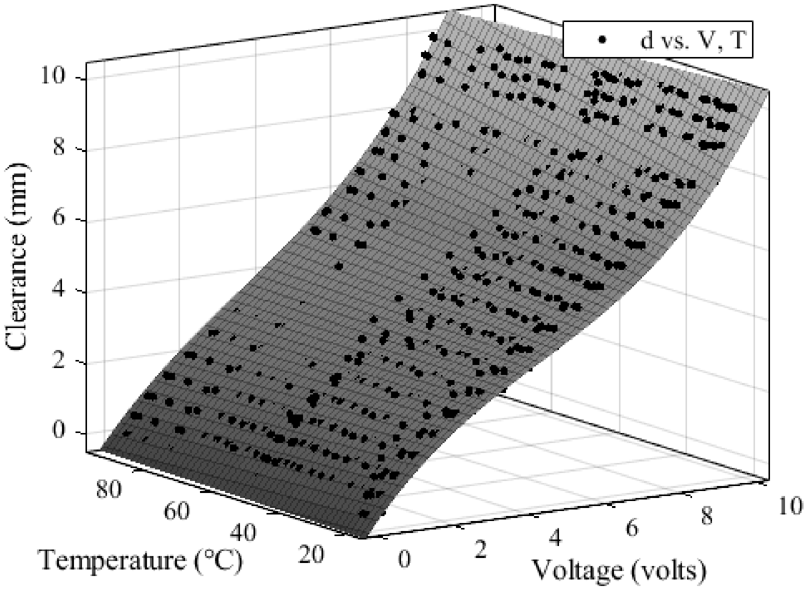

Figure 3-5. Fitting of the regression model

3.2. Design of IIR digital filter

The design of a digital filter involves the following five steps:

i. Filter specification: this includes stating the type of filter, the desired amplitude and phases response and the tolerances, the sampling frequency, and the word length of the input data.
ii. Filter coefficients calculation: the coefficient of a transfer function H(z) is determined in this step, which satisfies the given specification. The choice of coefficient calculation method will be influenced by several factors. The most important of which are the critical requirements that is, specification.
iii. Realization: this involves converting the transfer function into a suitable filter network or structure
iv. Analysis: The effect of quantizing the effect of filter coefficients and input data as well the effect of carrying out the filtering operation using fixed word length on the filter performance is analyzed.
v. Implementation: This involves producing the software code/hardware and performing actual filtering.

The output data signal (clearance) is defined at discrete instants of time, every millisecond. Data acquitted automatically by the prototype system is considered the measured data and recorded from micrometer gauges, the actual data. From the sampling period T that is the time taken to collect one sample data, sampling frequency $f_s = 1/T$ is determined. To filter out noises from this measured data, a digital filter, in this case, is designed to allow some frequencies to pass while attenuating others.

A low pass Butterworth recursive filter is selected to be designed to remove out the noises from the measurement data. Its Suitable characteristic is a maximum flatness in the passband at frequency zero and maximum flatness in the stopband at infinite frequency. However, the transition band roll-off rate is very shallow for a given filter order N. In practice, Butterworth's ideal frequency response is unattainable. It produces an excessive passband ripple. We start with the realizability constraints that must be satisfied by the discrete-time transfer function. Then deal with the aforementioned details that can be used to derive transformed low-pass discrete-time transfer functions from a given low-pass discrete-time transfer function. There are different analytical approaches to design IIR digital filters. In this case, we adopt the different approaches to see which gives better results when designing these filters, in terms of calculating filter coefficients and showing the responses. The following are the steps taken

- Choose prototype continuous-time lowpass filter $H_{lp}(s)$
- Prewarp critical frequencies, that is, take frequencies in the discrete domain and map them to corresponding frequencies of a continuous filter. This mapping is chosen so that when we apply Bilinear transformation, the critical frequencies end up where we want them to be.
- Apply frequency transformation,

$$H(\check{s}) = H_{lp}(s)|_{s=f(\check{s})} \tag{3.15}$$

- Apply the bilinear transformation, $H(z) = H(\check{s})|_{s=\frac{2}{T}\left(\frac{z-1}{z+1}\right)}$. Given an analog filter, the corresponding digital filter is readily obtained by using the bilinear transformation.

In this, a digital filter system is designed using lab-view and Simulink. Figure 3-6 shows the physical design of the digital filter as a block using Labview.

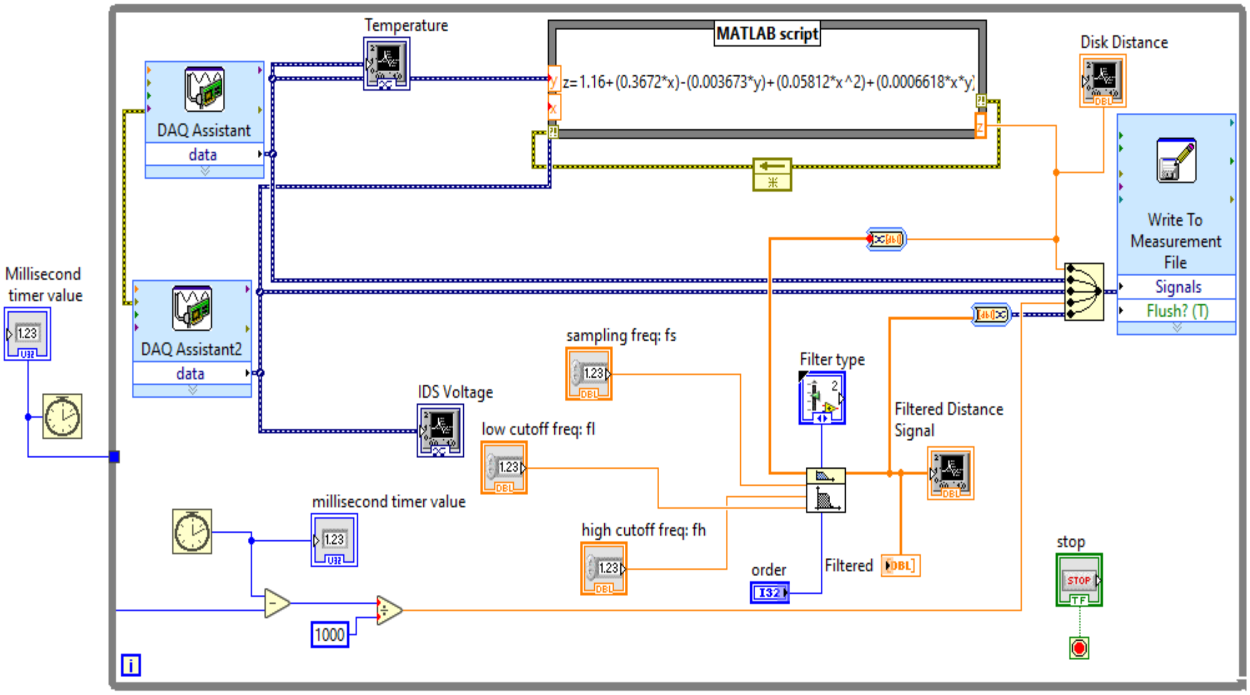

```
z=1.16+(0.3672*x)-(0.003673*y)+(0.05812*x^2)+(0.0006618*x*y)
```

Figure 3-6. Labview graphical programming interface with updated regression model in the Matlab script

Simulink model of the IIR filter is designed and configured with the data acquisition system (see Figure 3-7)

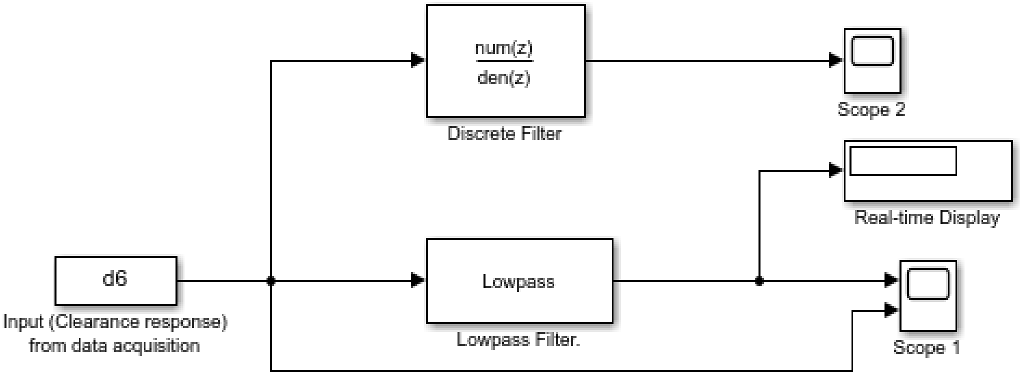

Figure 3-7. Online filter in model Simulink

3.3. Locomotive multi-body system simulation

When the train moves on track, many dynamics involve changing the wheelsets and the bogie frame position. With the sensor support structure fixed to the bogie frame and in range with the wheel flange, these dynamics affect measurement readings as the set point of the inductive sensor may be changing. The previous research using inductive displacement sensor [5] studied lateral and Yaw displacements of the wheelsets at curves about the designed sensor holding fixture. Here we look at vertical, lateral, and yaw displacements of the wheelsets and bogie frame. The Ethio-Djibouti railway under study uses a co-co locomotive to drive both the passenger and freight wagons. This co-co locomotive has two bogie frames, each of which has its wheelsets. The vertical, lateral, and yaw displacements of the bogies and wheelsets translates noises in the flange measurements through sensor support structure fixed on the bogie frame. The multibody simulations are carried out to determine these displacements when the Locomotive moves through curved tracks and show vibrations translated from the irregularities of the track. Therefore, a suitable sensor support mechanism design is proposed to maintain the set coordinate of the sensing tip during curves. An online digital filter to removing noises in measurement resulting from displacements, locomotive vibrations, and track irregularities is designed.

3.3.1. Physical model

The locomotive and curved track model is designed using universal mechanism software. The vehicle is modeled as a multibody system with 106 degrees of freedom considering every component in the locomotive. There are several principles components, one car body, two bogies, six wheelsets, traction rods, reduction gear boxes, rotor card on a shaft, and axle boxes. Equations governing the locomotive dynamics are defined by the existing principles [45]. D'Alembert's principle is used to define the equations of motion of the Locomotive by using the system coordinates moving along the curved track with vehicle speed. The locomotive equation of motion is described as a second-order differential equation in the time domain.

$$m_v a_v + c_v(v_v)v_v + k_v(x_v)x_v = F_v(x_v, v_v, x_t, v_t) + F_{ext} \tag{3.16}$$

Where x_v, v_v, and a_v are vectors of displacements, velocities, and accelerations of the rail vehicle, respectively; m_v is the mass matrix of the vehicle; $c_v(v_v)$ and $k_v(x_v)$ are the damping and stiffness matrices that depend on the current state of the rail vehicle, hence describing nonlinearities within the suspension; $x_t\ and\ v_t$ are the vectors of displacement, and velocities of the track subsystem; $F_v(x_v, v_v, x_t, v_t)$ is the system load vector representing the non-linear wheel-rail contact forces that depend on the motions x_v, v_v of the rail vehicle and x_t, v_t of the track; and F_{ext} are external forces including gravitational forces and centripetal forces when the Locomotive moves through a curve. In the locomotive model, there are several principal components, including one loco-body, two bogies, six wheelsets, traction rods, reduction gearboxes, rotor Cardan shaft, and axle boxes All components are assumed to be rigid each with 5 degrees of freedom (vertical, lateral, yaw, pitch and roll motions).

3.3.1.1. Locomotive model

The basic unit of a high-speed train model is the locomotive model, which depends on the specific train formation. The locomotive sub-model is established here based on the multibody system dynamics. Assumptions are made that:

a) The loco-body, bogie frames, and wheelsets are all rigid bodies with no elasticity.
b) The locomotive body moves at a constant speed along the track without consideration of the stretching vibration of the vehicle and the longitudinal dynamic interaction between neighboring vehicles.
c) The loco-body is symmetrical about its center of mass at x, y, and z directions.

Figure 3-8 shows the locomotive model of a high-speed train consists of seven rigid bodies, including the loco-body, bogies, and wheelsets, as well as primary and secondary suspensions. The model considers the linear or non-linear stiffness and damping properties of the primary and the secondary suspension in three directions. As stated earlier five DOFs are taken into consideration for each rigid body.

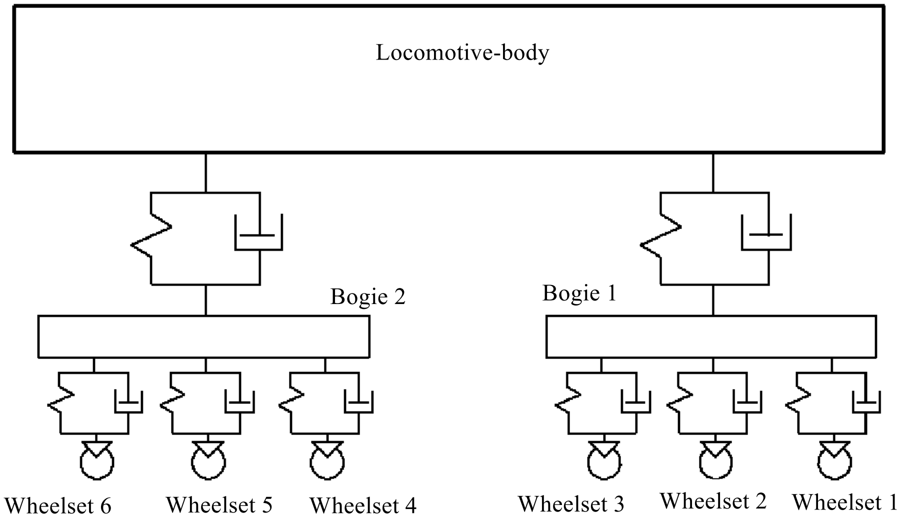

Figure 3-8. Three-dimensional locomotive model: side elevation

3.3.1.2. Equation of motion for the locomotive

The equation of the locomotive vehicle subsystem is established according to D'Alembert's principle as shown in Equations (3.17)-(3.36) [46]. The vehicle suspensions forces are dependent on the suspension properties as well as relative displacements and relative velocities between two components at the end of the suspension systems.

(1) Equation of motion of the locomotive body

The physical meaning of the notations used is shown in Table 0-1 in the appendix section (see Appendix A.)

Vertical motion:

$$m_{lc}\left(\ddot{z}_{lc} - d_o\ddot{\theta}_{selc} - \frac{V^2}{R_{lc}}\theta_{selc} - g\right) = -F_{zsL1} - F_{zsR1} - F_{zsL2} - F_{zsR2} \tag{3.17}$$

Pitch motion:

$$I_{lcy}\ddot{\varphi}_{lc} = (F_{zsL1} + F_{zsR1} - F_{zsL2} - F_{zsR2})l_{lc} + (F_{xsL1} + F_{xsR1} + F_{xsL2} + F_{xsR2})h_1 \tag{3.18}$$

Lateral motion:

$$m_{lc}\left[\ddot{y}_{lc} + \frac{V^2}{R_c} + (r_o + h_1 + h_2 + h_3)\ddot{\theta}_{selc} - g\theta_{selc}\right] = F_{ysL1} + F_{ysR1} + F_{ysL2} + F_{ysR2} \tag{3.19}$$

Roll motion:

$$I_{lcx}(\ddot{\theta}_{lc} + \ddot{\theta}_{selc}) = (F_{zsL1} - F_{zsR1} + F_{zsL2} - F_{zsR2})e_2 - (F_{ysL1} + F_{ysR1} + F_{ysL2} + F_{ysR2})h_1$$

.... (3.20)

Yaw motion:

$$I_{lcx}[\ddot{\psi}_{lc} + V\frac{d}{dt}(\frac{1}{R_{lc}})] = (F_{ysL1} + F_{ysR1} - F_{ysL2} - F_{ysR2})l_c + (-F_{xsL1} + F_{xsR1} - F_{xsL2} - F_{xsR2})e_2 \tag{3.21}$$

(2) Equation of motion for bogies (i=1-2)

Vertical motion:

$$m_b\left(\ddot{z}_{bi} - d_o\ddot{\theta}_{sebi} - \frac{V^2}{R_{bi}}\theta_{sebi} - g\right) = -F_{zsLi} + F_{zsRi} - F_{zfL(2i-1)} - F_{zfR(2i-1)} - F_{zfL(2i)} - F_{zfR(2i)} \tag{3.22}$$

Pitch motion:

$$I_{by}\ddot{\varphi}_{bi} = \left(F_{zfL(2i-1)} + F_{zfR(2i-1)} - F_{zfL(2i)} - F_{zfR(2i)}\right)l_b - (F_{xsLi} + F_{xsRi})h_2 - (F_{xfL(2i-1)} + F_{xfR(2i-1)} + F_{xfL(2i)} + F_{xfR(2i)})h_3 \tag{3.23}$$

Lateral motion:

$$m_b\left[\ddot{y}_{bi} + \frac{V^2}{R_{bi}} + (r_o + h_3)\ddot{\theta}_{sebi} - g\theta_{sebi}\right] = -F_{ysLi} - F_{ysRi} + F_{yfL(2i-1)} + F_{yfR(2i-1)} + F_{yfL(2i)} + F_{yfR(2i)} \tag{3.24}$$

Roll motion:

$$I_{bx}(\ddot{\theta}_{bi} + \ddot{\theta}_{sebi}) = -(F_{yfL(2i-1)} + F_{yfR(2i-1)} + F_{yfL(2i)} + F_{yfR(2i)})\, h_3 - (F_{ysLi} + F_{ysRi})h_2 + (F_{zfL(2i-1)} - F_{zfR(2i-1)} * F_{zfL(2i)} - F_{zfR(2i)})e_1 - (F_{zfL(2i)} - F_{zfR(2i)})e_2 \tag{3.25}$$

Yaw motion:

$$I_{bz}\left[\ddot{\psi}_{bi} + V\frac{d}{dt}\left(\frac{1}{R_{bi}}\right)\right] = \left(F_{yfL(2i-1)} + F_{yfR(2i-1)} - F_{yfL(2i)} - F_{yfR(2i)}\right)l_b - \left(F_{xfL(2i-1)} - F_{xfR(2i-1)} + F_{xfL(2i)} + F_{xfR(2i)}\right)e_1 + (F_{xsLi} + F_{xsRi})e_2 \tag{3.26}$$

(3) Equation of motion for wheelsets (j=1-6)

Vertical motion:

$$m_w\left(\ddot{z}_{wj} - d_o\ddot{\theta}_{sewj} - \frac{V^2}{R_{wj}}\theta_{sewj} - g\right) = -F_{zfLj} + F_{zfRj} - N_{Lzj} - N_{Rzj} - F_{Lzj} - F_{Rzj} \tag{3.27}$$

Lateral motion:

$$m_w\left[\ddot{y}_{wj} + \frac{V^2}{R_{wj}} + (r_o)\ddot{\theta}_{sewj} - g\theta_{sewj}\right] = -F_{yfLj} - F_{yfRj} + N_{Lyj} + N_{Ryj} + F_{Lyj} - F_{Ryj} \tag{3.28}$$

Roll motion:

$$I_{wx}(\ddot{\theta}_{wj} + \ddot{\theta}_{sewj}) = e_1(F_{zfRj} - F_{zfLj}) + d_o(N_{Lzj} - N_{Rzj} + F_{Lzj} - F_{Rzj}) - r_{Lj}(N_{Lyj} + F_{Lzj}) - r_{Rj}(N_{Rzj} + F_{Rzj} \tag{3.29}$$

Yaw motion:

$$I_{wz}\left[\ddot{\psi}_{wj}+V\frac{d}{dt}\left(\frac{1}{R_{wj}}\right)\right]=e_1\left(F_{xfLj}-F_{xzfRj}\right)+d_o\psi_{wj}\left(N_{Lyj}-N_{Ryj}+F_{Lyj}-F_{Ryj}\right)+ d_o\left(F_{Lxj}-F_{Rxj}+N_{Lxj}-N_{Rxj}\right) \tag{3.30}$$

(4) Equations defining suspension forces

Secondary suspension (longitudinal, lateral and vertical) forces: (i=1-2)

$$F_{xs(L,R)i}=K_{2x}\left[h_1\emptyset_{lc}+h_2\emptyset_{bi}\pm e_2\psi_{lc}\mp e_2\psi_{bi}\mp(-1)^{i-1}e_2\left(\frac{l_{lc}}{R_{lc}}\right)\right]+C_{2x}\left[h_1\dot{\emptyset}_{lc}+h_2\dot{\emptyset}_{bi}\pm e_2\dot{\psi}_{lc}\mp e_2\dot{\psi}_{bi}\mp(-1)^{i-1}e_2\frac{d}{dt}\left(\frac{l_{lc}}{R_{lc}}\right)\right] \tag{3.31}$$

$$F_{ys(L,R)i}=K_{2y}\left[y_{bi}-y_{lc}+h_1\theta_{lc}+h_2\theta_{bi}+(-1)^{i-1}\,l_{lc}\psi_{lc}\left(\frac{{l_{lc}}^2}{2R_{lc}}\right)\right]+C_{2y}\left[\dot{y}_{bi}-\dot{y}_{lc}+h_1\dot{\theta}_{lc}+h_2\dot{\theta}_{bi}+(-1)^{i-1}l_{lc}\dot{\psi}_{lc}+\frac{d}{dt}\left(\frac{{l_{lc}}^2}{2R_{lc}}\right)\right] \tag{3.32}$$

$$F_{zs(L,R)i}=K_{2z}(z_{lc}-z_{bi}\mp e_2\theta_{lc}\mp e_2\theta_{bi}+(-1)l_{lc}\varphi_{lc})+C_{2z}\left(\dot{z}_{lc}-\dot{z}_{bi}\mp e_1\dot{\theta}_{lc}\mp e_2\dot{\theta}_{bi}+(-1)l_{lc}\dot{\varphi}_{lc}\right) \tag{3.33}$$

Primary suspension (longitudinal, lateral, and vertical) forces: (j=1-6)

$$F_{xf(L,R)j}=K_{1x}\left[h_3\emptyset_{bi}\pm e_2\psi_{bi}\mp e_2\psi_{wj}\mp(-1)^{i-1}e_1\left(\frac{l_b}{R_{bi}}\right)\right]+C_{1x}\left[h_2\dot{\emptyset}_{bi}\pm e_1\dot{\psi}_{lc}\mp e_1\dot{\psi}_{wj}\mp(-1)^{j-1}e_1\frac{d}{dt}\left(\frac{l_b}{R_{bi}}\right)\right] \tag{3.34}$$

$$F_{yf(L,R)j}=K_{1y}\left[y_{wj}-y_{bi}+h_3\theta_{bi}+(-1)^j\,l_b\psi_{bi}+\left(\frac{{l_b}^2}{2R_{bi}}\right)\right]+C_{2y}\left[\dot{y}_{wj}-\dot{y}_{bi}+h_3\dot{\theta}_{bi}+(-1)^j l_b\dot{\psi}_{bi}+\frac{d}{dt}\left(\frac{{l_b}^2}{2R_{bi}}\right)\right] \tag{3.35}$$

$$F_{zf(L,R)j}=K_{1z}\left(z_{bi}-z_{wj}\mp e_1\theta_{bi}\mp e_1\theta_{wj}+(-1)^j l_b\phi_{bi}\right)+C_{1z}\left(\dot{z}_{ti}-\dot{z}_{wj}\mp e_1\dot{\theta}_{bi}\mp e_1\dot{\theta}_{wj}+(-1)^j l_b\dot{\phi}_{bi}\right) \tag{3.36}$$

3.3.2. Numerical simulation of the locomotive system dynamics

Computer simulation of the locomotive train subsystem provides an efficient and effective approach to evaluating the dynamics and vibrations as it moves through the curved track geometry which is uneven.

3.3.2.1. Integration of equation of motions using the universal mechanism software

Numerical integration is one of the basic tools for the analysis of mechanical system behavior. A multi-variant mode of simulation is used in this case since UM Experiments module is available in the UM configuration. A numerical method and accuracy of the integration are chosen, with the results being extracted. This facilitates the supervision of the object motion with the help of as many animation windows as necessary. The information displayed in the graphical windows can easily be copied, interrupt integration at the instant of concern, and interactively influence the integration process by processing messages in the control file.

With the object simulation inspector input parameters are specified before the simulation process starts:

- To choose a numerical method and its parameters;
- To change initial conditions (coordinates and their time derivatives);
- To modify identifier values;
- To assign a list of automatically calculated variables.

The park solver method which is an implicit solver of the second order with a variable step size is selected. Minimal step size is chosen to get precise computations. Since the speed of the locomotive is set to 20m/s the use of jacobian matrices is not activated because the solver is stable. Reducing the locomotive speed to less than 8-10 m/s, as a rule, it requires activating the use of Jacobian matrices, set smaller tolerance, and set minimal step size to zero. This is because the solver might result in instable solutions. The equation of motions of the locomotive are generated according to Newton—Euler formalism and are differential-algebraic. Analysis of the equations is carried out using the ABM, BDF numerical multistep methods with automatic choice of the step size and the order of the method, as well as the Park and Gear methods for stiff equations. The Park-parallel solver is the powerful numeric-iterative solver, which allows the usage of multithreading on the multi-core processors.

3.3.3. CAD models of the locomotive subsystems

Figure 3-9 shows the wheelset motoring assembly. The traction motor casing is rigidly fixed to the bogie frame. The rotor is connected to the motor casing by the rotation joint jTraction motorRotor. The shaft transmits the traction torque by coupling to the Gear wheel of the reducer. The reduction gearbox is connected to the wheelset by the rotation joint jWSet_reduction gearbox and to the frame by the linear bipolar element Rod.

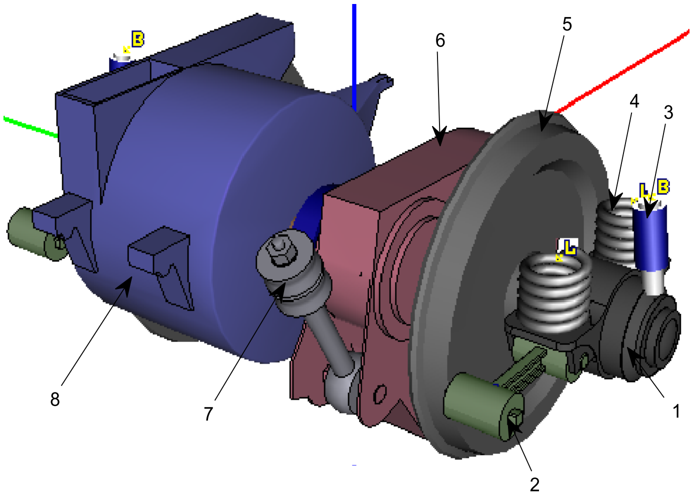

Figure 3-9. Model of wheelset-motor assembly (WMA): axle-box (1), traction rod (2), damper (3), primary suspension (4), wheel (5), reduction gearbox (6), reducer suspension rod (7), traction motor (8)

The bogie model contains three included subsystems WMA (see Figure 3-10). The front and the rear WMA are identical, whereas the middle differs in the description of the axle-boxes degree of freedom. An inclined traction rod is used in the bogie model for the transfer of the traction efforts. The traction rod is connected with the bogie frame and car body by special force elements of the bushing type joint _traction_1 and joint_traction_2. The second bushing is the external one. The bogie model is finalized by assigning connections to all external elements introduced in the WMA subsystems.

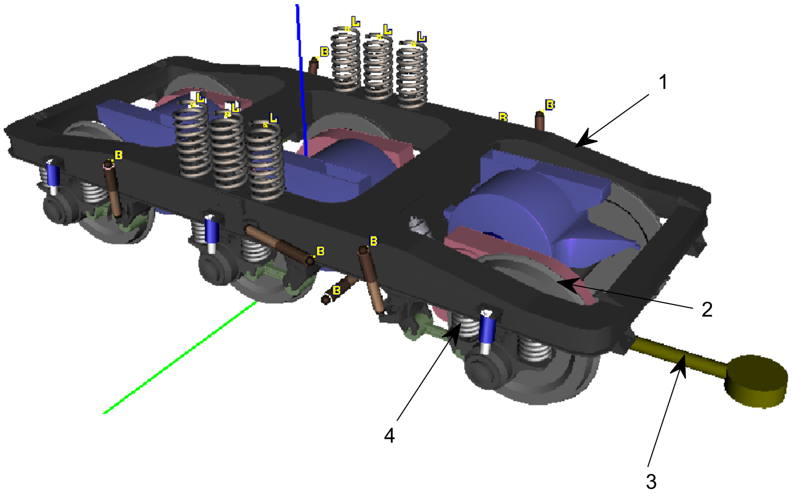

Figure 3-10. Bogie model: Bogie frame (1), wheelset with motoring assembly (2), traction rod (3), primary suspension (4)

Now considering a full locomotive model, the bogie is converted into a subsystem. After that, the car body image was created in a CAD program (Inventor) and imported to UM. The model includes one body corresponding to the loco-body, and one joint with six degrees of freedom jbody introducing coordinates of the car body relative to the SCO. Figure 3-11 presents the locomotive model.

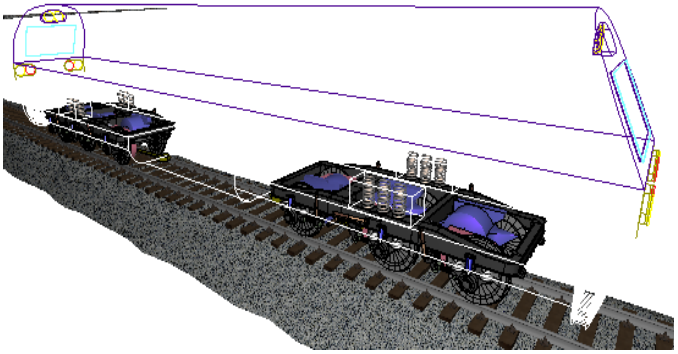

Figure 3-11. Locomotive model

The input parameters to the locomotive are all included in the process of modeling before the simulations are run. The details of the specifications are included in the appendix (see Tables 0-2 to 0-7).

3.3.4. Physical design of track model

A ballast track with concrete sleepers in this case is considered as in the case of Ethio-Djibouti mainline. The following parameters are considered for the track model: a tangent of 10m; length of transition before the curve of full constant radius (P11) is set to 50m; Length of the curve of constant radius (R1) 300m; cant (H) 0.09m; length of transition curve after the curve of constant radius is set to 50m; track widening in a curve is: $15\text{mm}(R < 300m), 10mm(R \leq 350m)$. Point (0;0;1.4) is selected on two bogie frames, and for each bogie, one wheelset is selected with the sensor pointed at the wheelbase (0;0;0). The locomotive runs at a velocity of 20m/s on track with a single lateral irregularity at the beginning of the track. The amplitude of the irregularity is 20mm, and its length is 10m. The effects of these irregularities from the displacement results are then presented. Specifying the track properties as stated, a graphical track model is shown below (see Figure 3-12).

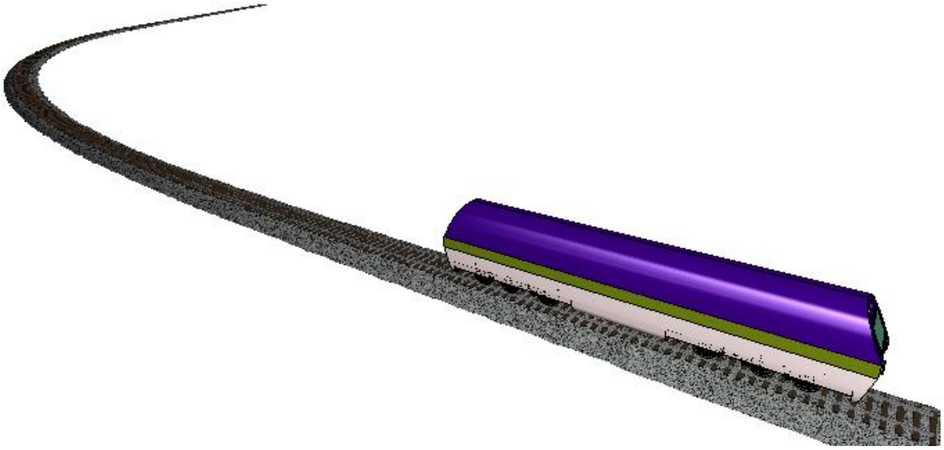

Figure 3-12. Locomotive moving through the curved track

3.4. Sensor support structure CAD design

The work presented in this paper consists of measuring the wheel flange wear in terms of the clearance between the sensor tip and wheel flange surface (see Figure 3-13). Using Autodesk inventor professional, a computer-aided drawing of a sensor support structure mechanism is designed and fixed on the bogie frame. The structure is strategically placed to be in the measuring range of the wheel flange.

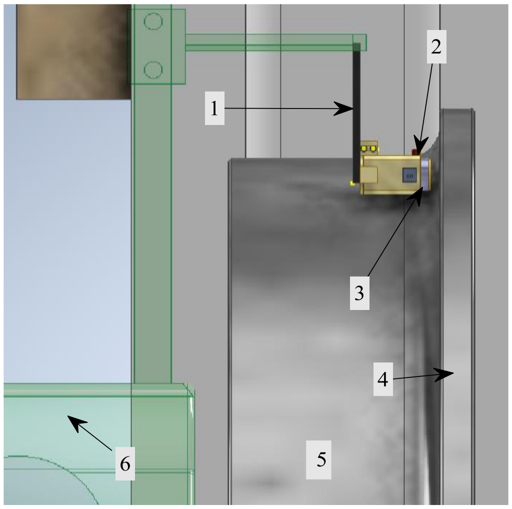

Figure 3-13**.** Magnified view on the fixed position of the sensor support structure, (1) Sensor holding fixture, (2) Thermocouple sensor, (3) Inductive sensor, (4) Wheel flange, (5) Wheel tread, (6) Bogie frame

The sensor support structure design has provisions for holding the inductive displacement sensor and temperature sensor. It consists of linear and angular positioners to ensure that the inductive sensor is in proximity range, follows the wheel flange maintaining coordinate points at all track geometries. Accessibility being a factor, it is positioned in a strategic place where it can be easy for maintenance. Figure 3-14 shows the mechanisms in the sensor support structure.

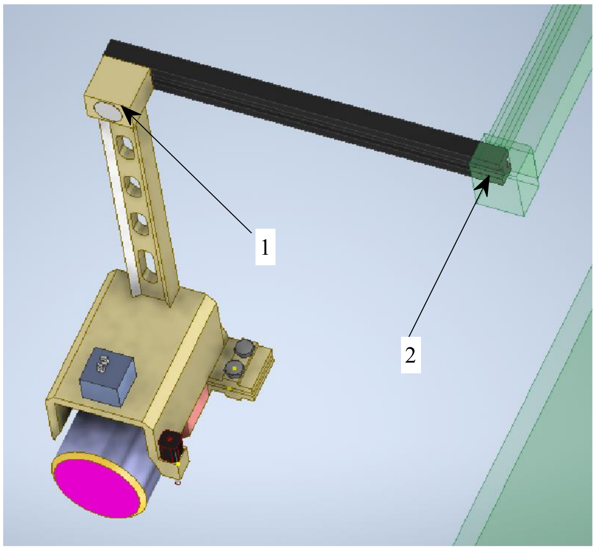

Figure 3-14. Sensor support structure mechanism: servo positioners (1), lateral positioner (2)

The wheel flange thickness reduction, R_T, is determined by the difference between the set reference distance (d_{rf}) and the measured distance (d_f).

$$R_T = d_f - d_{rf}, \tag{3.37}$$

Where d_f is the clearance between the sensor tip and the wheel flange surface; d_{rf} of the next measurement is the last measured distance. Safe operation of the train is when the measured thickness reduction is less than the minimum allowable reduction h.

$$R_T \leq h. \tag{3.38}$$

The wheel flange thickness is given by T, (see Figure 3-15)

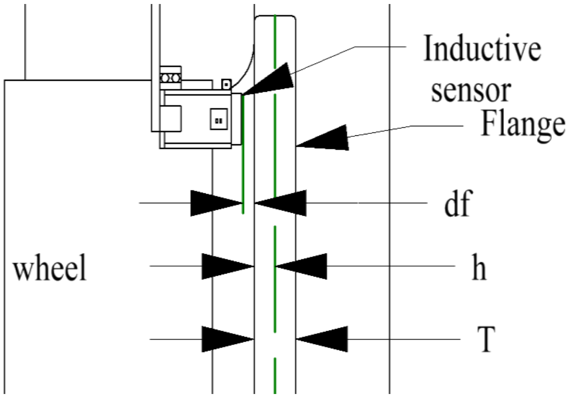

Figure 3-15. Wheel flange detection and sensor characteristics

The sensor positioned in proximity to the flange surface with an initial clearance of 2mm. With maximum flange thickness given as 33mm, the system is set to trigger a warning alarm when the clearance is measured to 8mm. Meaning the wear of the flange is of 6mm and the flange thickness is 27mm. Further, when the flange thickness reaches to 25mm, a continuous alarm goes off signifying criticality of the safety of the locomotive. Therefore, these wheels should be replaced before any accidents may occur.

4 RESULTS AND DISCUSSIONS

In this chapter, a discussion of the results acquired from the experimental testing is presented and analyzed. Signal processing analysis of the measured data is carried out and the IIR low pass Butterworth filter is designed to remove noises in measurement. Multibody simulation results and analysis are also presented. Finally, simulation results of the online IIR digital filter are presented, where the accuracy and sensitivity of the system are determined.

4.1. Effect of temperature on inductive displacement sensor

The results presented were obtained from, manual measurements recorded on daily basis. The average of these multiple measurements at different temperatures is plotted (see Figure 4-1) where voltage placed is against clearance. The challenge while taking these measurements was keeping the temperature constant while collecting data (manual measurements). The drift of the measurement due to temperature changes is seen. Figure 4-1 (a) shows the distribution of data from $\mathbf{20}^{\circ}\mathrm{C}\ \boldsymbol{to}\ \mathbf{48}^{\circ}\mathrm{C}$, where at different temperatures, there is voltage variation at each clearance of the target (disk). The voltage is seen to converge as the disk clearance gap goes further away from the inductive sensor. Increasing temperatures from $\mathbf{50}^{\circ}\mathrm{C}\ \mathbf{to}\ \mathbf{73}^{\circ}\mathrm{C}$, minimal drift from 0mm to 5mm is registered and from 5mm to 10mm a significant temperature effect on data is observed as the voltage diverges (see Figure 4-1b).

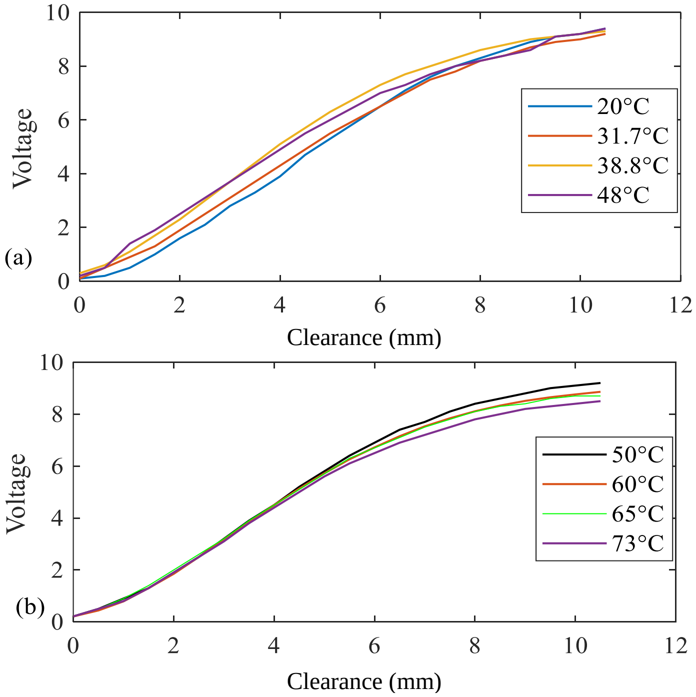

Figure 4-1. Average daily measurement data at different temperatures “in press” [47]

Further increasing temperatures from **79℃ to 98℃**, drift in measurement from 5mm to 10mm is observed with deviations of 0.1mm to 0.5mm (see Fig 4-2). There is a consistent drop in the analog output voltage when the temperature around the inductive sensor is increased. To explain this phenomenon, elevating temperatures around the shielded analog inductive sensor increases the resistance of the ferrite coil decreasing the sensor output voltage.

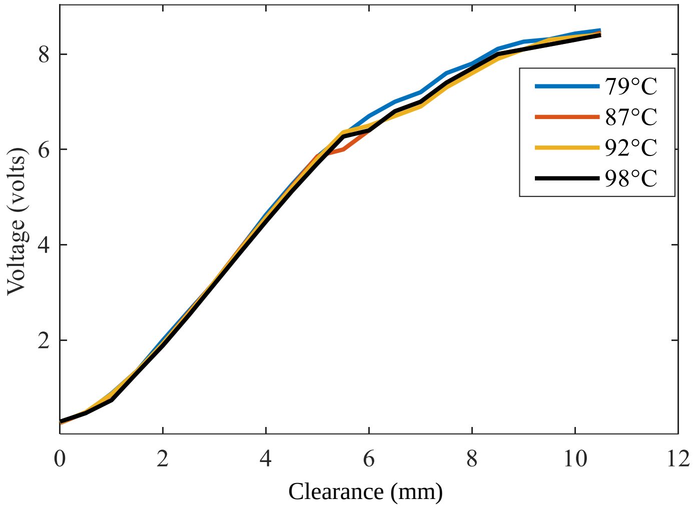

Figure 4-2. Average daily measurements from 79℃ *to* 98℃

In design, this analog inductive displacement sensor is constructed of an RCL oscillating circuit composed of a capacitor in parallel with an inductor and resistor. The inductor is made with a coil wound around a ferrite core whose internal resistance is affected by temperatures, Heat transfer by radiation to the inductive sensor affects the measurements of the flange thickness as in the case (see Figure 4-1a and 4-1b). At these higher temperatures, 79℃ to 98℃, starting from clearance of 8.5mm the output voltage values of the inductive sensor are very close showing effects of saturation. This means that the sensing range diminishes as temperatures increased at higher temperatures. This demonstrates the effect of temperature on the analog inductive displacement sensor used for flange measurements.

4.2. Error in measurement relative to clearance at different temperatures

This subsection shows errors in the measurement of the inductive displacement sensor output voltage at different temperatures. They compare the error at each clearance measurement. For this case, the reference measurement is taken to be at room temperature where the inductive displacement sensor operates normally. The normal operating range of the inductive sensor during experiments in the laboratory was at 20℃. Therefore, we calculate the error in output voltage at each temperature with the following formula.

$$error\ in\ measurement = |V - V_R| \tag{4.1}$$

Where V is the observed output voltage at each clearance and V_R is the reference voltage that is taken at room temperature. Figure 4-3 below presents a comparison of errors in measurement from **20**℃ **to 65**℃. The error at **20**℃ is at the baseline zero in the graphs since it is taken to be the reference point. From the presented results, we see the variation in errors in measurements at different temperatures.

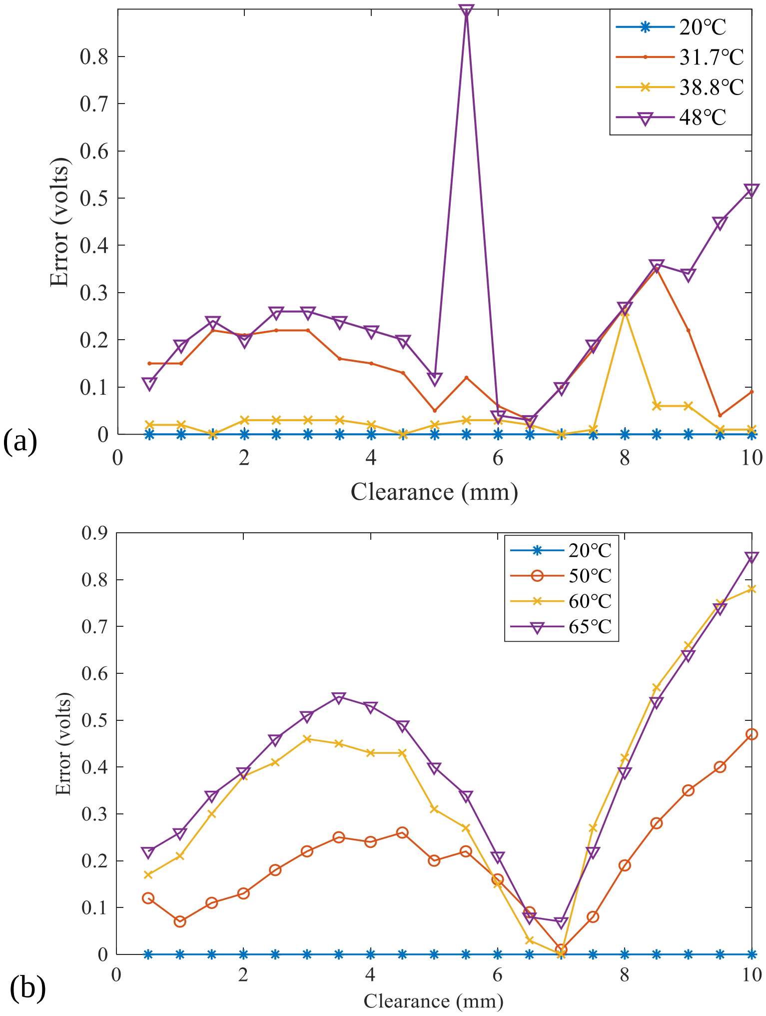

Figure 4-3. Error in output at different temperatures

Further, we continue to determine the error in measurement at elevated temperatures, that is, from **20**℃ **to 98**℃ (see Figure 4-4). It is evident that errors in measurement due to the temperature effect are significant, hence this calls for machine learning methods to train the system on the patterns of the measurements with different input conditions.

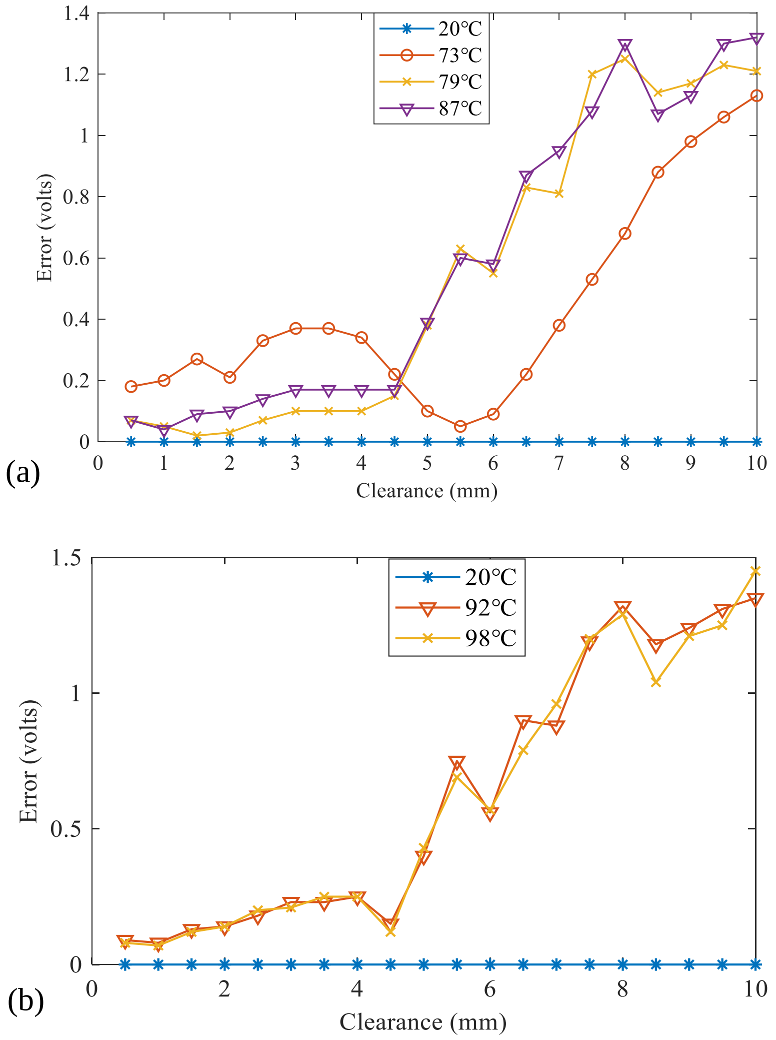

Figure 4-4. Error in measurement output at different temperatures

From repeated daily measurements taken at different temperatures, the precision of the measurement system was studied by repeatability testing, determined using relative standard deviation.

$$s_{pooled} = \sqrt{\frac{[(n_1-1)s_1^2+(n_2-1)s_2^2+\cdots+(n_k-1)s_k^2]}{[n_1+n_2+\cdots+n_k-k]}} \qquad (4.2)$$

Where s_k is the standard deviation of daily measurements from the multiple measurements taken. The repeatability is calculated at each temperature, and the variations result from random errors in experimental measurements (see Table 4-1).

Table 4-1. Repeatability at different temperatures

Relative standard deviation (Volts)	**Temperature**
±0.05818	19.4℃
±0.0983705	20℃
±0.107465	25℃
±0.04565	38.8℃
±0.064083	44℃
±0.0637246	48℃
±0.054814	50℃
±0.132915	55℃
±0.0113445	60℃
±0.0134643	65℃
±0.050675	70℃
±0.02942	73℃

4.3. Disk clearance measurement system results and frequency analysis

Stage two of the experiments involving the data acquisition system presents measurement results of predicted clearance against time. The data prediction technique was used to combine and correlate all the experimental raw data measured using the inductive sensor and thermocouple (K type) to achieve a refined disk position and identify the exact estimated clearance of the disk. In this case, all data collected from the sensors was loaded into the database. From correlation analysis, a regression equation takes inputs from both sensors and estimates the wheel flange thickness as the output at any given temperature. The response is obtained from data integration of inductive sensor and thermocouple type K by the regression equation updated regularly every time more data is loaded to the database. Figure 4-5 shows the clearance response taken at 43℃ to 50℃ which is compared with the true data, that is read from the micrometer with the timer at certain intervals of time. Measurements are taken as temperatures around the sensor keep on changing. The data used to develop a regression model fusing these inputs have temperatures reach up to 73℃.

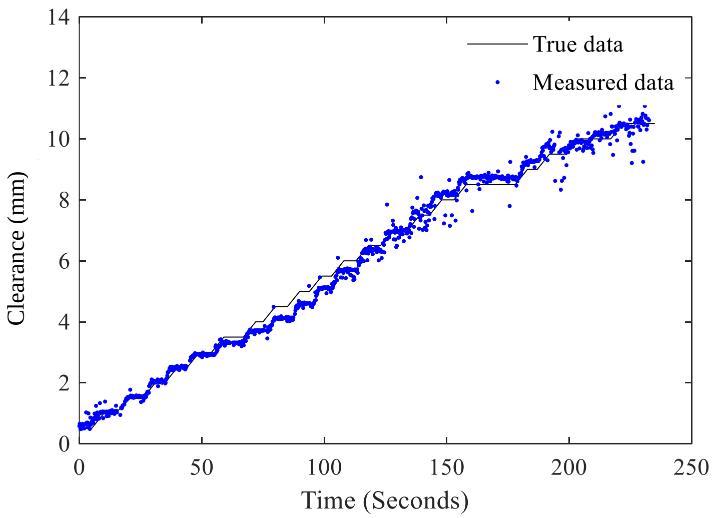

Figure 4-5. Measured clearance readings against time using the data acquisition system

The accuracy of the output about the actual clearance is shown (see Table 4-2) calculated in terms of absolute error.

$$percent\ error = [(|d_o - d_a|)/d_a]\% \tag{4.3}$$

Where $d_o = Measured\ value, d_a = \ True\ value,$

$$|d_o - d_a| = Absolute\ error$$

Table 4-2. Accuracy estimation of the system at different disk positions

Clearance (mm)	Error	%error
1	0.02595	2.595
2	0.020736	2.0736
3	0.024471	2.4471
4	0.078376	7.8376
5	0.081988	8.1988
6	0.056695	5.6695
7	0.01452	1.452
8	0.02922	2.922
9	0.027095	2.7095
10	0.0226914	2.26914

The precision of the system is averaged to $\pm 0.06083V$, corresponding to an error of 0.038174, that's an accuracy of 96.1826%, from which the sensitivity of the sensor is determined as

1.594volts/mm. The sensitivity of the system changes at different temperatures, as shown in Table 4-3.

Table 4-3. Sensitivity of the system dependent on the temperature

Sensitivity (Volts/mm)	**Temperature**
1.524	19.4℃
2.577	20℃
2.815	25℃
1.196	38.8℃
1.679	44℃
1.669	48℃
1.436	50℃
3.482	55℃
0.297	60℃
0.353	65℃
1.328	70℃

More recorded measurements from 19.8℃ to 98℃ were added to the database, and the regression model equation (3.14) was updated. The system then took measurements at temperature 92℃ to 96℃ and the predicted clearance is seen in Fig 4-6 below.

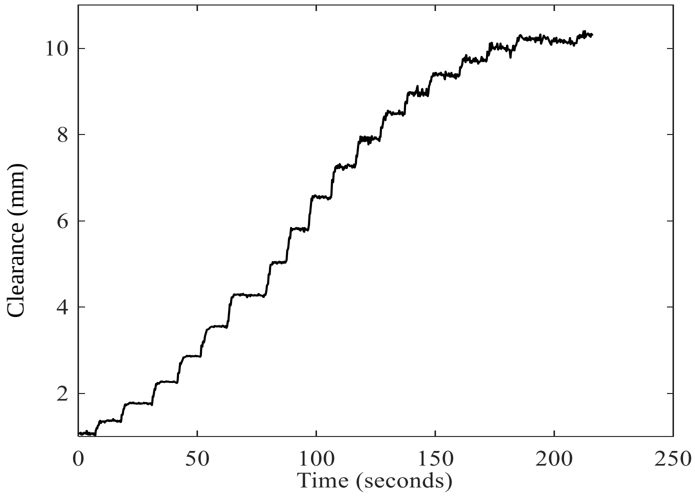

Figure 4-6. Real-time disk measurement readings at temperatures 92℃ to 98℃

The accuracy of the system is then measured (see Figure 4-7)

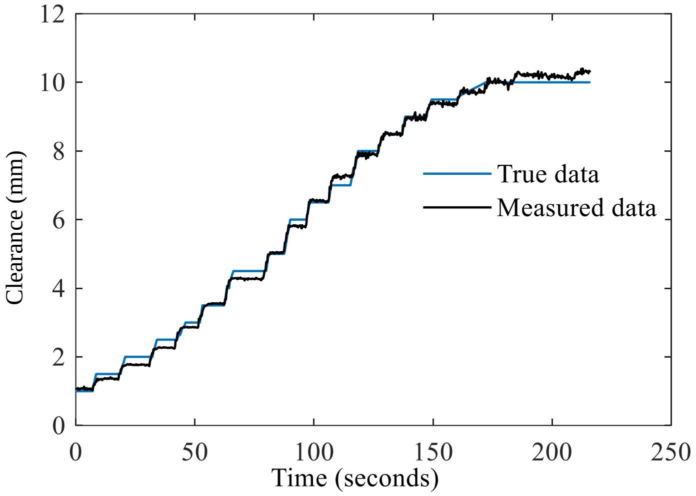

Figure 4-7. Accuracy test of the acquitted response

Equation (4.3) determines the system's accuracy at each disk position in terms of percentage error. Table 4-4, Presents the results, which are averaged to get the overall system accuracy at elevated temperatures.

Table 4-4. Accuracy estimation of the system at different disk position measured response

Clearance (mm)	**Error**	**Percent error (%)**
1	0.068014	6.801436
1.5	0.089082	8.908169
2	0.107114	10.71144
2.5	0.084953	8.495297
3	0.044563	4.456256
3.5	0.014637	1.463719
4	0.025938	2.593796
4.5	0.047186	4.71855
5	0.007226	0.722596
6	0.031677	3.167742
6.5	0.007587	0.75868
7	0.034893	3.489255
7.5	0.009612	0.961197
8	0.012693	1.269339
8.5	0.00301	0.301005
9	0.006372	0.637185
9.5	0.012563	1.256268
10	0.016844	1.684358
Average	0.034665	3.46646

The error improves by reducing to 0.034665, thus the accuracy of the predicted clearance response at different disk positions from the added data has improved to 96.534%. It is can be argued that over time, the system loses its properties, and needs a sort of calibration. However, the calibration requires a lot of input data to be taken at a time. The machine learning agent is taught by previous data acquired during measurement.

4.3.1. Filter design specifications from the measurements

As observed in Figure 4-8, there are noises present in measurement resulting from systematic errors during measurements. These noises reflect higher frequencies in the FFT analysis of the measured response (see Figure 4-6), hence reducing the accuracy of the system (See Appendix B). Frequency analysis of the measured response (clearance) is correlated with the actual measurements to determine the filter design specifications

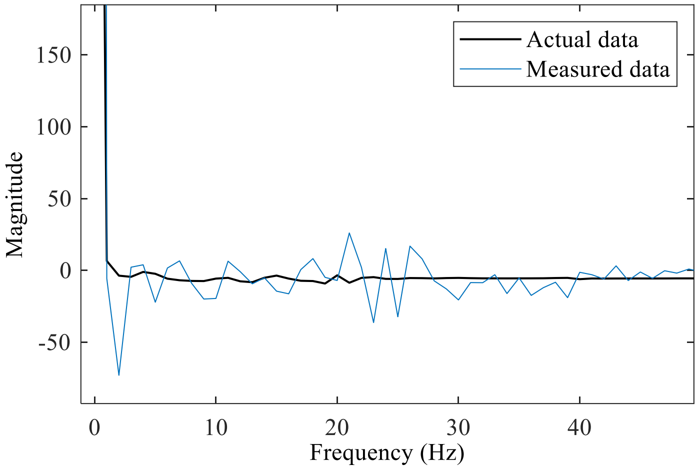

Figure 4-8. FFT analysis of the real-time measured and actual clearance data

A generalized equation representing an nth order Butterworth filter, the frequency response is given as:

$$|H_n(j\omega)| = A_o/\sqrt{1+(\omega/\omega_o)^{2n}} \tag{4.4}$$

Where A_o is the maximum gain in the passband, ω_o, the upper cutoff angular frequency in radians per second, ω is the angular frequency of the input signal, and n is the order of the filter. The squared response of the Butterworth filter is given as the function of the cutoff frequency

$$|H_n(j\omega)|^2 = 1/(\omega/\omega_o)^{2n} \tag{4.5}$$

The design specifications from FFT analysis of the output signal are given; sampling frequency (f_s)= 6Hz; hence T=0.167sec. Approximation of the passband edge $(f_p) = 0.1\ Hz$ and stopband edge $(f_a) = 0.9\ Hz$ are obtained from the FFT analysis.

$$\omega = 2\pi f / f_s$$

$$\omega_p = 2\pi f_p = 2\pi \times 0.21 rad/sec$$

$$\omega_a = 2\pi f_a = 2\pi \times 0.9 rad/sec$$

Cut off frequency, $\omega_c = \frac{(\omega_p + \omega_a)}{2} = 3.142 rad/sec$

Transition band: $\Delta\omega = \omega_a - \omega_p = 4.335 rad/sec$

Next, we apply a pre-warping transformation: pre-warp critical (stopband, passband) frequencies to transform to a required continuous system, for which ω is in the digital domain and Ω is in the analog domain. The bilinear z-transform is a mathematical transformation from the s-domain to the z domain, which preserves the frequency characteristics, defined by:

$$s = \frac{2}{T}\frac{1-z^{-1}}{1+z^{-1}} \tag{4.6}$$

where T = sampling period

The entire $j\omega$ axis in the s-plane is mapped onto the unit circle in the z-plane, where the left-half s-plane is mapped inside the unit circle and the right-half s-plane outside the unit circle. Ω is solved as :

$$z = \frac{1+{}^{s}/_{2}}{1-{}^{s}/_{2}} \quad \xrightarrow[s = j\omega]{} \quad z = \frac{1+{}^{j\Omega}/_{2}}{1-{}^{j\Omega}/_{2}} \rightarrow e^{j\omega} = \frac{1+{}^{j\omega}/_{2}}{1-{}^{j\omega}/_{2}}$$

Solving for Ω,

$$j\Omega = \frac{2}{T}\frac{1-e^{-j\omega T}}{1+e^{-j\omega T}} = \frac{2}{T}\frac{e^{{}^{j\omega T}/_{2}} - e^{{}^{-j\omega T}/_{2}}}{e^{{}^{j\omega T}/_{2}} + e^{{}^{-j\omega T}/_{2}}} = \frac{2je^{{}^{-j\omega}/_{2}} \sin{}^{\omega T}/_{2}}{2je^{{}^{-j\omega/}/_{2}} \cos{}^{\omega T}/_{2}} \tag{4.7}$$

$$\Omega = \frac{2}{T}\tan{}^{\omega T}/_{2}$$

Therefore, the pre-warped critical frequencies are:

$$\Omega_p = \frac{2}{T} tan \frac{\omega_p T}{2} = 1.328 rad/s$$

$$\Omega_a = \frac{2}{T} tan \frac{\omega_a T}{2} = 6.1287 rad/s$$

In which, $f_p = 0.21128 Hz$ and $f_a = 0.975 Hz$ shows the warping effect near $\frac{f_s}{2}$.

$$\mathrm{f}_c = \frac{f_p + f_a}{2} = 0.59314 Hz,$$

Next, the order of the Butterworth filter is determined as:

$$N = \frac{\log \frac{\sqrt{10^{0.1\alpha_a - 1}}}{\sqrt{10^{0.1\alpha_p - 1}}}}{\log\left(\frac{\Omega_a}{\Omega_p}\right)} \tag{4.8}$$

To simplify the numerator, let us set: $\sqrt{10^{0.1\alpha_a} - 1} = \lambda$ and $\sqrt{10^{0.1\alpha_p} - 1} = \varepsilon$,

such

$$N = \frac{\log\left(\frac{\lambda}{\varepsilon}\right)}{\log\left(\frac{\Omega_a}{\Omega_p}\right)} \tag{4.9}$$

λ and ε are calculated from the following expressions:

$$\frac{1}{\sqrt{1+\varepsilon^2}} = A_{p1} \text{ and } \frac{1}{\sqrt{1+\lambda^2}} = A_{a1} \tag{4.10}$$

Considering δ is the amplitude of the largest passband ripple which happens to be the same as the amplitude of the largest stopband ripple. The maximum passband loss and minimum stopband attenuation is defined as

$$A_p = 20 \log(1 + \delta / 1 - \delta) \tag{4.11}$$

$$A_a = -20 log\delta \tag{4.12}$$

Setting δ to be 0.01 taken from the FFT, A_p and A_a are calculated to be

$$A_p = 0.1737 dB$$

$$A_a = 40 dB$$

In linear terms, the gain is:

$$A_{p1} = 10^{\frac{A_{dB}}{20}} = 10^{\frac{-0.1737dB}{20}} = 0.9802$$

$$A_{a1} = 10^{\frac{A_{dB}}{20}} = 10^{\frac{-40dB}{20}} = 0.01$$

Substituting these values to equation (4.10), we have: $\frac{1}{\sqrt{1+\varepsilon^2}} = 0.9802, \; \frac{1}{\sqrt{1+\lambda^2}} = 0.01$

Hence, $\varepsilon \; = 0.1802 \;\; \lambda = 499.999$. Substitution these variables to equation (4.9), the filter order is found to be:

$$N \geq \frac{2.69}{0.664} \geq 4.0582$$

$$N = 5$$

The predetermined transfer function of a normalized sixth order low pass filter is given as:

$$H_n(s) = \frac{1}{\mathrm{s}^5+3.236\mathrm{s}^4+5.236\mathrm{s}^3+5.236\mathrm{s}^2+3.236\mathrm{s}+1} \tag{4.13}$$

Now we substitute $s \rightarrow \frac{s}{\Omega_c}$

$$\Omega_c = \frac{\Omega_p}{(\sqrt{10^{0.1\alpha_p} - 1})^{1/N}} = \frac{\Omega_p}{(\varepsilon)^{1/N}} = \frac{1.328}{(0.1802)^{1/5}} = 1.871 rad/s$$

$$H(s) = \; H_n(\frac{s}{\Omega_c}) = \frac{1}{\left(\frac{s}{3.727}\right)^5+3.236\left(\frac{s}{3.727}\right)^4+5.236\left(\frac{s}{3.727}\right)^3+5.236\left(\frac{s}{3.727}\right)^2+3.236\left(\frac{s}{3.727}\right)+1}$$

$$H(s) = \frac{1}{0.0014s^5+0.0168s^4+0.1011s^3+0.377^2+0.8683s+1} \tag{4.14}$$

Applying the bilinear transformation to the transfer function of an arbitrary analog filter yields a digital filter characterized by the discrete-time transfer function

$$H(z) = H(s)|_{s=\frac{2}{T}\left(\frac{1-z^{-1}}{1+z^{-1}}\right)}$$

where T=0.167seconds

$$H(z) = \frac{0.001076+0.005379z^{-1}+0.01076z^{-2}+0.01076z^{-3}+0.005379z^{-4}+0.001076z^{-5}}{1-3.06z^{-1}+3.997z^{-2}-2.721z^{-3}+0.9566z^{-4}-0.138z^{-5}} \tag{4.15}$$

Figure 4-9 shows the magnitude response of the fifth-order filter

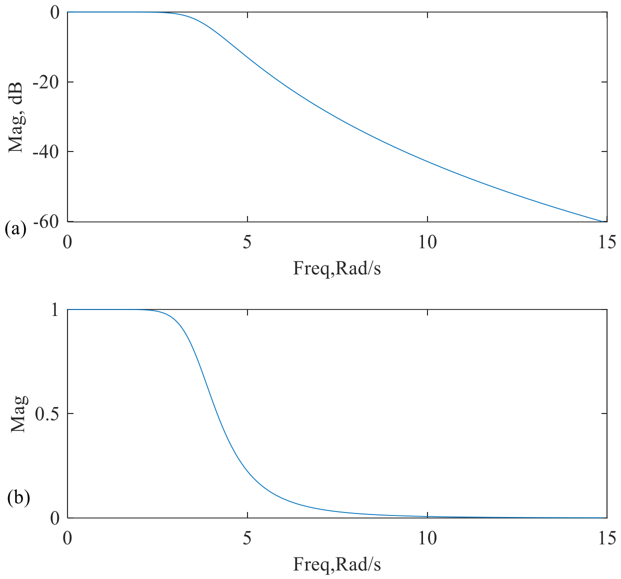

Figure 4-9. (a) Magnitude (db) response, and (b) Magnitude (linear) response

It is known that transfer function;

$$H(z) = \frac{Y(z)}{X(z)} \text{ , from which } Y(z) = H(z)X(z)$$

Inversing the transfer function, the finite difference equation of the filter is found to be:

$$y(n) = 3.06y(n-1) - 3.997y(n-2) + 2.721y(n-3) - 0.9566y(n-4) + 0.138y(n-5) + 0.001076x(n) + 0.005379x(n-1) + 0.01076x(n-2) + 0.010706x(n-3) + 0.005379x(n-4) + 0.001076x(n-5) \quad (4.16)$$

4.4. Multi-body simulation results and filter design specification

This subsection presents the multi-body simulation results of the locomotive dynamics along the curved track showing vertical, lateral, and yaw displacement motions. Fourier analysis of these displacements is done to which they are correlated with the measurement data.

4.4.1. Vertical, lateral, and yaw displacements

The locomotive model designed in um input runs in um simulations window, where all the parameters to be analyzed is selected. Below are the graphical results data showing vertical, lateral, and yaw motion of wheelsets and bogie. Vertical displacement of the left and right wheels on all bogies is displayed (see Figure 4-10). During the curve transition, oscillations due to the lateral irregularity with amplitude 20mm at length 10m are shown by the uniform trend of the curve. At constant curve radius, vertical displacement increases from the initial position, to which the point of wheel-rail contact is displaced, and the wheel position changes as the train moves through the curve. When the Locomotive nears the end of the transition curve, approaching a straight track the positions of the wheelsets becomes initials.

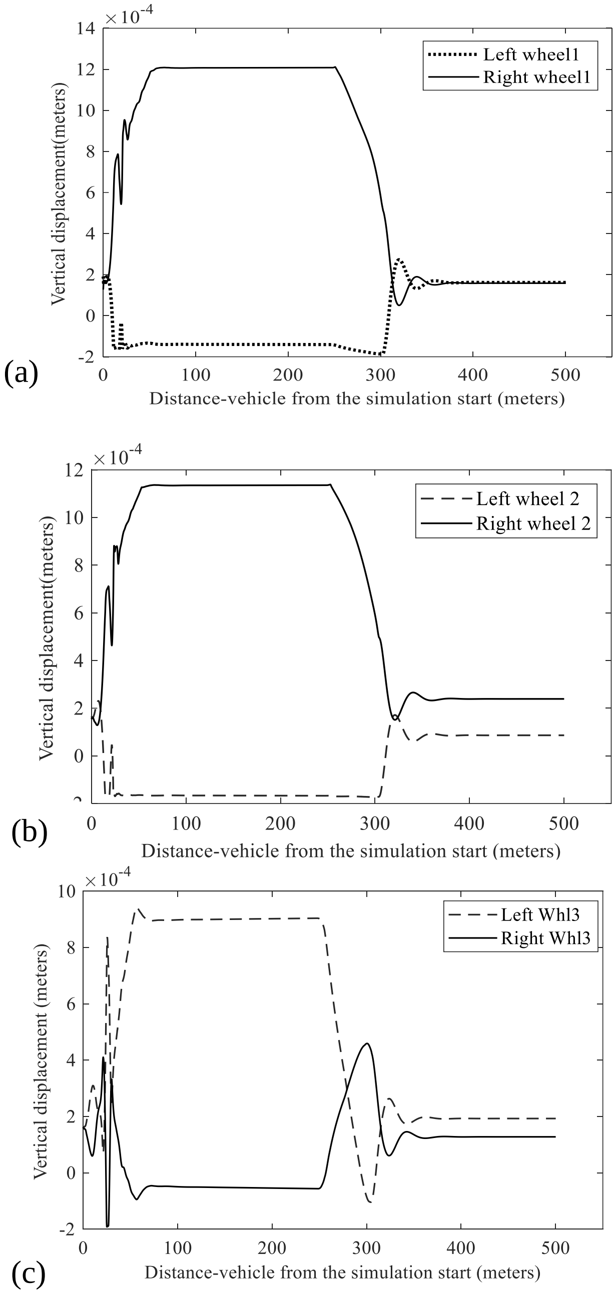

Figure 4-10. Vertical displacement of the wheelsets

Table 4-5. Presents maximum vertical displacements of the left and right wheels for three wheelsets gotten from simulations

Table 4-5. Maximum vertical wheelset displacement

Vertical displacement		
Wheelset	**Right wheel (mm)**	**Left wheels (mm)**
1	1.2	0.2
2	1.135	0.1672
3	0.188	0.9322

The bogie vertical displacement from its sitting position increases to 34mm on the constant curve radius (see Figure 4-11).

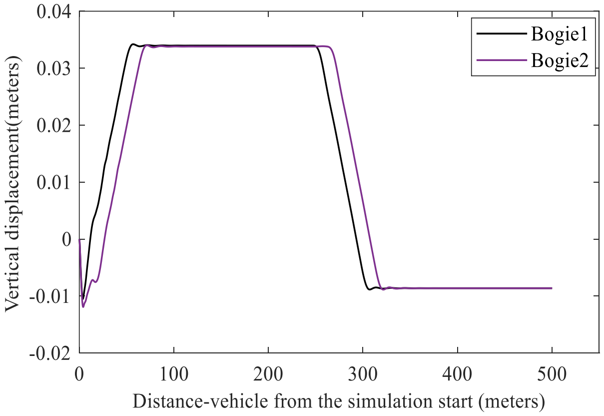

Figure 4-11. Vertical displacement of the bogie

The centripetal forces experienced at the curve shifts the positions of wheels at different points from initial contacts. The three wheelsets have different lateral displacement values. Wheelset one and two seem to have the same motion distinct from wheelset three (see Figure 4-12). Table 4-6. shows the maximum lateral displacements of both left and right wheels from the simulation.

Table 4-6. Maximum lateral wheelset displacement

Lateral displacement		
Wheelset	**Right wheel (mm)**	**Left wheel (mm)**
1	21.41	6

2	19.4	6
3	5.92	14.64

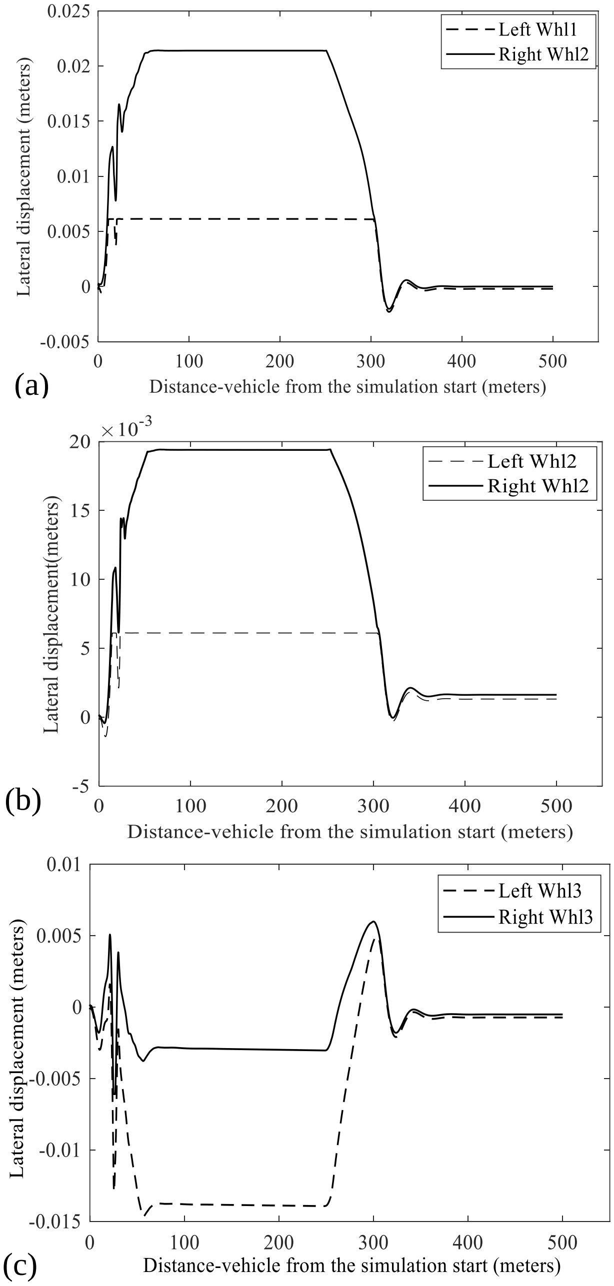

Figure 4-12. Lateral displacement of the wheelsets

The yaw motion of the wheelsets is presented as shown (see Figure 4-13). Vibrations resulting from the lateral irregularities are seen at the beginning of the uneven oscillations when the train is in a transition curve. Wheelset one leads in the yaw displacements on the two bogies.

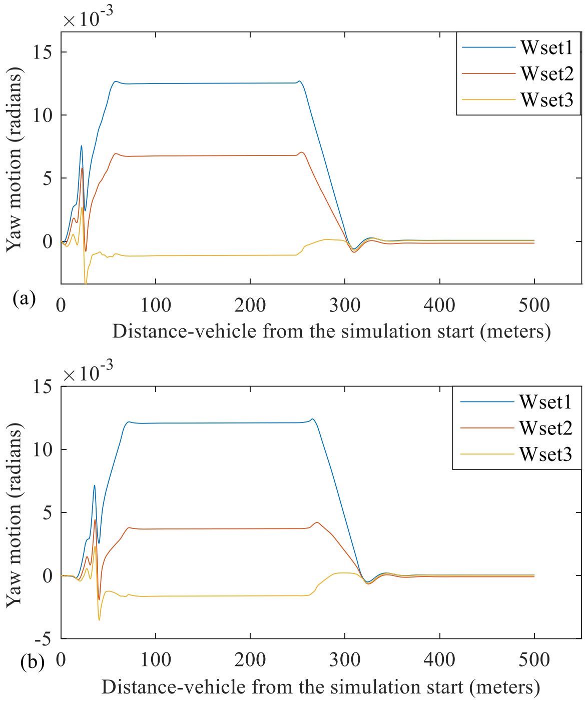

Figure 4-13. Yaw motion of the wheelsets

Table 4-7. tabulates the maximum yaw displacement of the wheelsets relative to the local system of coordinate.

Table 4-7. Yaw displacement

Maximum yaw displacement (radians)		
	Bogie 1	**Bogie 2**
1	0.012578	0.012
2	0.00608	0.0037137
3	0.00116	0.001577

Comparing these results with the literature of close works done to determine the bogie and wheelsets displacements, we see that different input parameters conditions in these papers were used [45], [48]–[50]. However, a different case scenario in this multi-body simulation is used, where we use a speed of 72km/h and the locomotive moving on a 600m radius, with lateral irregularities. Eralp et al [51] analysis, shows the lateral, yaw, and vertical displacement results at different speeds along a tangent track geometry. It was therefore seen that maximum lateral displacement to be 2mm, 5mm, and 8.5mm at 15km/h, 50km/h, and 90km/h respectively. For yaw displacements of wheelsets the results are 0.006 rads, 0.001 rads, and 0.002rads at 15km/h, 50km/h and 90km/h respectively. Finally, for vertical displacements, the results are 2.5mm, 6mm, and 6.5mm at 15km/h, 50km/h, and 90km/h respectively. Though there is nothing much we could compare since the input conditions used for the analysis is different, we see the displacement values at speed 50 km/h are in range to some of the results we obtained.

4.4.2. Frequency analysis of the displacements

The FFT analysis of the displacements is correlated with actual measurements. Higher frequencies resulting from vibrations from the locomotive dynamics that will affect measurement data are identified, and stopband attenuation in decibels is determined. A stopband frequency of 50Hz corresponding to the stopband amplitude ripples (δ) is chosen for all the FFT analysis graphs of displacements. The attenuation is calculated using Equation 4.17

$$A_a = -20 log\delta \qquad (4.17)$$

Figure (4-14,15,16) Shows the FFT analysis of displacements from which the filter specification are extracted.

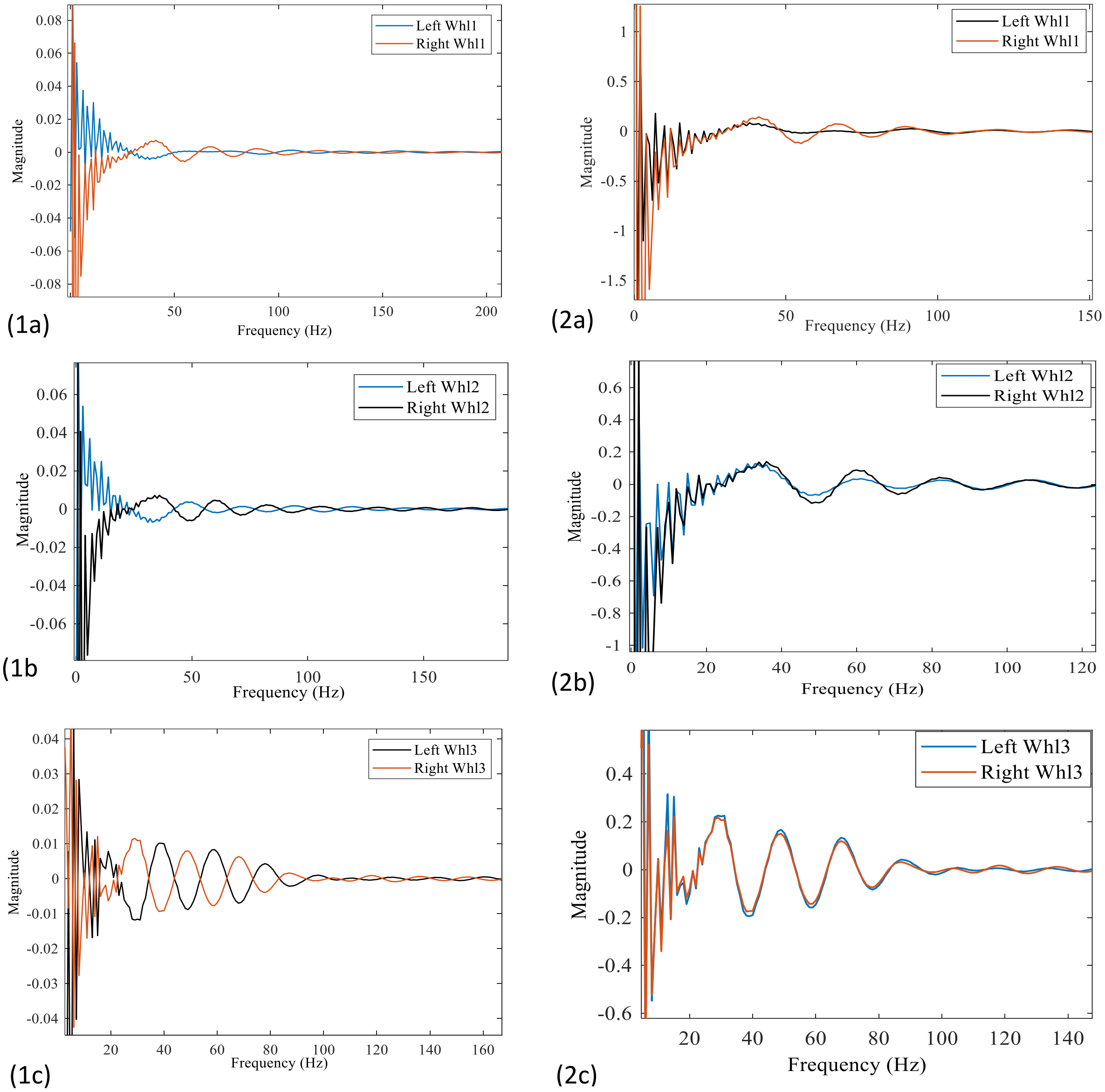

(1a)

(2a)

(1b

(2b)

(1c)

(2c)

Figure 4-14. FFT analysis of vertical 1(a,b,c) and 2(a,b,c) lateral displacement.

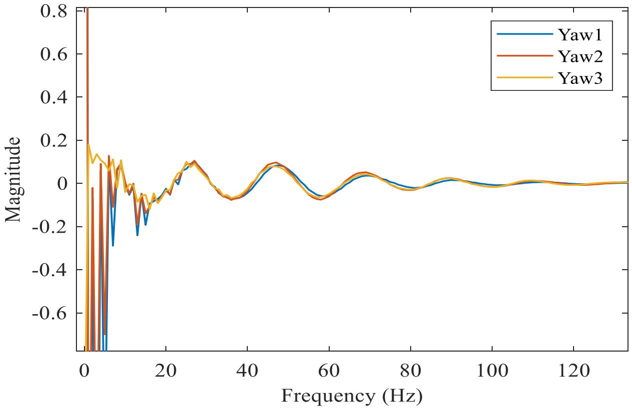

Figure 4-15. FFT analysis of the yaw motions of wheelsets in bogie1

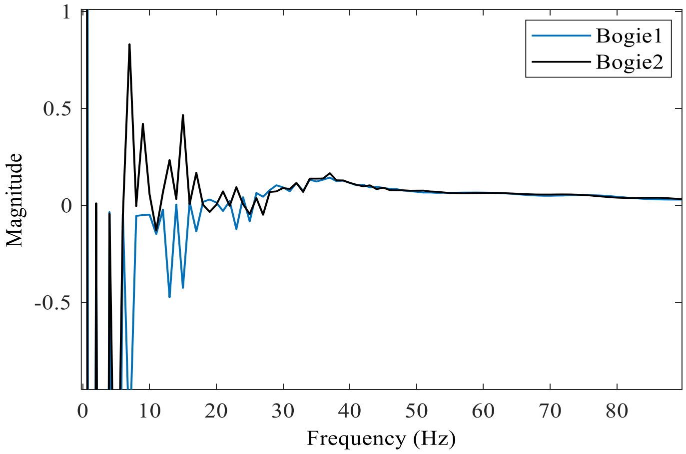

Figure 4-16. FFT analysis of the vertical motions of the bogie

Table 4-8 shows the stopband attenuations of the wheelsets and bogie displacement frequencies.

Table 4-8. Stopband attenuation for the displacements frequencies

Stopband attenuation (dB)			
	Vertical	**Lateral**	**Yaw**
Wheelset1	47.69	27.81	20
Wheelset2	60	24	21
Wheelset3	60	30.75	21.22
Wheelset4	52.69	30.18	23
Wheelset5	53.97	20.94	21.87
Wheelset6	49.77	17.78	23.5
Bogie1	23.769	35.65	
Bogie2	23.769	35.65	

The vertical displacement amplitude is smaller than that of the lateral and Yaw motion, meaning there are more vibrations in the lateral and Yaw motions. δ of the vertical wheelsets range from 0.001 to 0.004, while for the bogie frame where the sensor support structure is fixed equals 0.0648. Lateral displacement of the wheelsets registers much higher amplitudes than the vertical motions. The bogie lateral movement amplitudes are slightly lower than those of vertical motions. δ of the lateral wheelsets range from 0.04 to 0.129, while for the bogie frame equals 0.0165. Yaw motions frequency amplitudes shoot from 0.1 to 0.0668. Therefore to remove these higher frequencies that affect the measurement, a lowpass digital Butterworth filter with standard specifications to remove all these unwanted frequencies from all the vehicle dynamics is used. Lower amplitudes of the stopband attenuations with lesser ripples are chosen to design this filter. The data storage rate of the multi-body simulation was 0.01seconds for every displacement analysis; hence, sampling frequency (f_s)= 100Hz. Passband edge $(f_p) = 10\ Hz$ and stopband edge $(f_a) = 50Hz$ are selected from the FFT analysis. The same procedure is followed as of measurements filter design in section 4.3.1 with the following specifications.

$$\omega_p = 2\pi f_p = 62.832 rad/sec$$

$$\omega_a = 2\pi f_a = 314.159 rad/sec$$

Which leads to a low pass filter of minimum order of $N = 7$.

The predetermined transfer function of a normalized seventh-order low pass filter is given as [32]:

$$H_n(s) = \frac{1}{s^7+4.494s^6+10.0978s^5+14.5918s^4+14.5918s^3+10.0978s^{2+}4.494s+1} \tag{4.18}$$

Substituting for $s \rightarrow \frac{s}{\Omega_c}$ in (62),

$$\Omega_c = \frac{\Omega_p}{\left(\sqrt{10^{0.1\alpha_p}-1}\right)^{1/N}} = \frac{\Omega_p}{(\varepsilon)^{1/N}} = \frac{1.0966}{(0.0633)^{1/7}} = 1.626 rad/s$$

$$H(s) = H_n\left(\frac{s}{\Omega_c}\right) = \frac{1}{0.03314s^7+0.2423s^6+0.8857s^5+2.083s^4+3.388s^3+3.815s^2+2.762s+1} \tag{4.19}$$

Applying the bilinear transformation to the transfer function of an arbitrary analog filter yields a digital filter characterized by the discrete-time transfer function

$$H(z) = H(s)\big|_{s=\frac{2}{T}\left(\frac{1-z^{-1}}{1+z^{-1}}\right)} \text{ where T=0.01seconds,}$$

$$H(z) = \frac{Y(z)}{X(z)} =$$

$$\frac{2.273e{-}15z^7+1.591e{-}14z^6+4.773e{-}14z^5+7.955e{-}14z^4+7.955e{-}14z^3+4.773e{-}14z^2+1.591e{-}14z+2.273e{-}15}{z^7-6.927z^6+20.56z^5-33.92z^4+33.56z^3-19.93z^2+6.574z-0.9295} \;\ldots..$$

$$\ldots \tag{4.20}$$

The magnitude response of this 7th order low pass Butterworth filter is given as (see Figure 4-17)

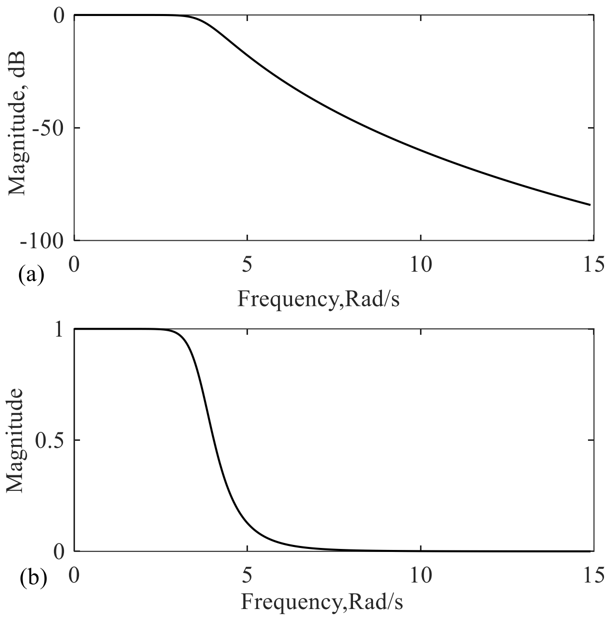

Figure 4-17. (a)Magnitude (dB) response, and (b) Magnitude (linear) response

Inversing the transfer function, the finite difference equation of the filter is found to be:

$$y(n) = 6.927y(n-1) - 20.56y(n-2) + 33.92y(n-3) - 33.56y(n-4) + 19.93y(n-5) - 6.574y(n-6) + 0.9295y(n-7) + 2.273e-15x(n) + 1.591e-14x(n-1) + 4.773e-14x(n-2) + 7.955e-14x(n-3) + 7.955e-14x(n-4) + 4.773e-14x(n-5) + 1.591e-14x(n-6) + 2.273e-15x(n-5) \tag{4.21}$$

4.5. Real-time noise and vibration filtering results

Filtering of the real-time measurements is implemented using the software IIR lowpass filter design. Using the filter specifications obtained numerically from the real-time measured response and the locomotive multibody system simulations, the actual real-time filtering using the Simulink model and LabView program is tested. First, a recursive equation (4.16) c++ Matlab code is written to filter noises in the measured response (Clearance) from the data acquisition. The data array of clearance against time is passed through the finite difference equation. Figure 4-18 shows the filtered data, from which noises are removed. A comparison of the filtered signal and unfiltered signal is also demonstrated (see Figure 4-19), as much of the noises reducing the accuracy of the system are eliminated.

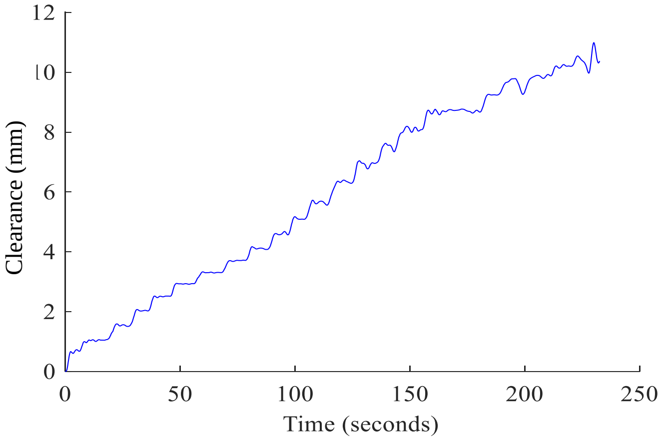

Figure 4-18. Filtering of the measured data using a 5th order Butterworth IIR filter

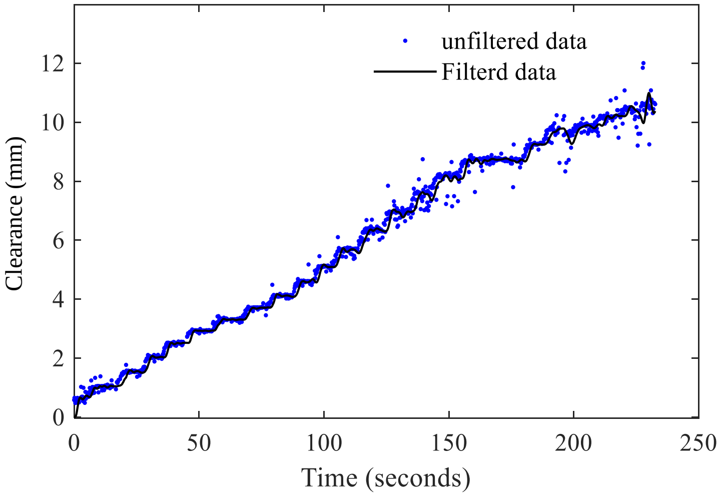

Figure 4-19. Comparison of filtered and unfiltered data

From the filtered data, we compute the accuracy of the signal to the true disk clearance. Figure 4-20 is used in the determination of the absolute errors in the filtered signal.

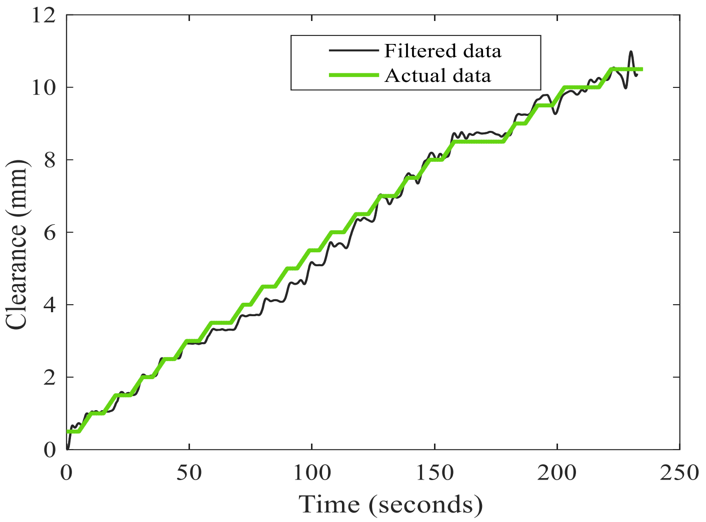

Figure 4-20. Accuracy measure of filtered data

The actual data is the accurate data that is taken from the manual measurements using the micrometer screw gauge with very high resolution. While the filtered data is the clearance response data with higher noise frequencies removed. Comparing the actual data with filtered data, the absolute measurement error of the system is averaged to 0.028058 (2.8058%). From the results, the accuracy of the filtered data with reference data has increased, as shown in Table 11 below.

Table 4-9. Calculated accuracy of the filtered data

Clearance (mm)	Error	%error
1	0.015534	1.5534
2	0.019077	1.9077
3	0.021802	2.1802
4	0.070238	7.0238
5	0.078392	7.8392
6	0.052738	5.2738
7	0.004391	0.4391
8	0.01114	1.114
9	0.027036	2.7036
10	0.011554	1.1554

To verify the real-time filtering, both Simulink and LabView filter models are considered. Equation (4.20) is the filter transfer function from which its coefficients are determined and used as the online filter parameters in Simulink and Labview models. The response is then filtered in real-time, in which the runtime and delay are continuously checked. The filter parameters are written to a Simulink real-time data acquisition model (see Figure 0-1 in appendix), and measurements are filtered online. Figure 4-21 shows the results of the filtered online response.

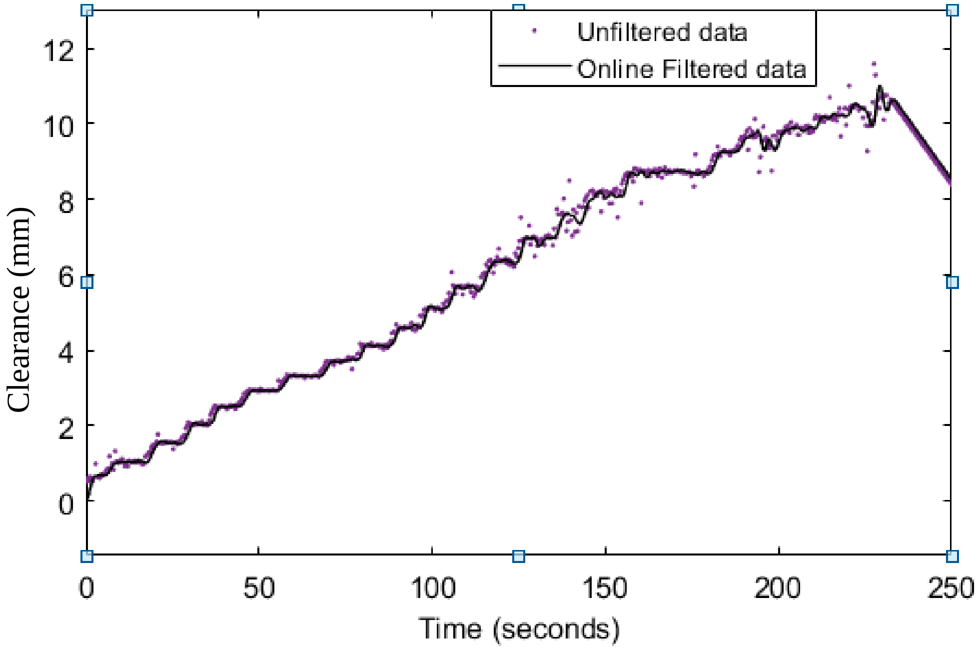

Figure 4-21. Real-time filtering of wheel flange measurements

From the filtered data, we compute the accuracy of the signal to the actual disk displacements. The actual data with filtered online data are compared, from which absolute to measurement error of the system was averaged to 2.8058%. Equation (70) from the locomotive multibody simulation dynamics frequency analysis is also written to Simulink real-time data acquisition model, and measurements are filtered online. From the result of the filtering process, it was seen to work through due to the increased filter order, a slight delay due to complexity in computation is observed (see Figure 4-22).

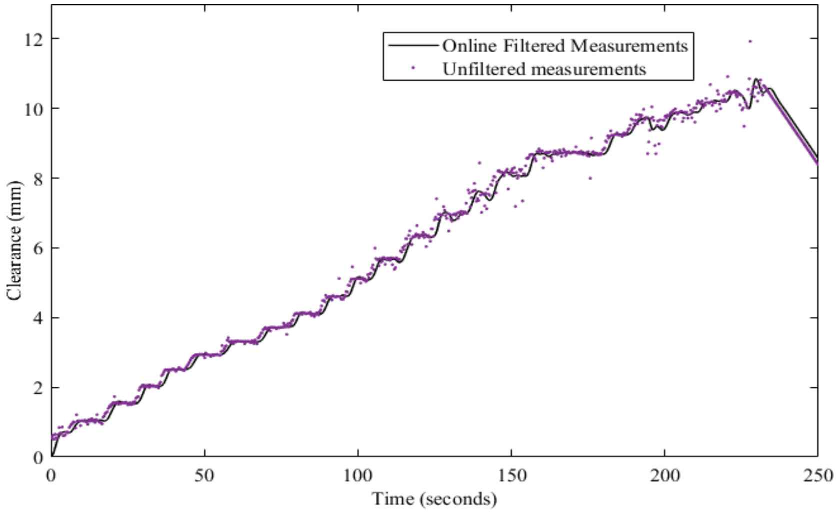

Figure 4-22. Real-time filtering of wheel flange measurements (Multi-body FFT analysis dynamics inclusive)

4.5.1. Online filtering using LabView

In the LabView software, an IIR low pass digital filter is modeled. The filter specifications extracted during the frequency analysis of the measurements and multibody simulations are used. Once the system is online (see Figure 3-6), measurements are taken, and in the front panel of the LabView program, shows scopes real-time data filtering and monitoring of the system. As shown in Figures 4-23, the runtime of the filtered results is low, meaning there are delays in the filtering process. This delay is explained due to the IIR Cascaded second-order section form II transposed structure used in Labview design of filters. This structure exhibits computational complexity, where it implements forward coefficients first, hence the delay experienced during the filtering process. When the order of the filter increases the delay increases because of an increase in computation complexity. However, the cascaded structure used in the filter design helps alleviate the finite word length effects, as seen from the smooth staircase curve.

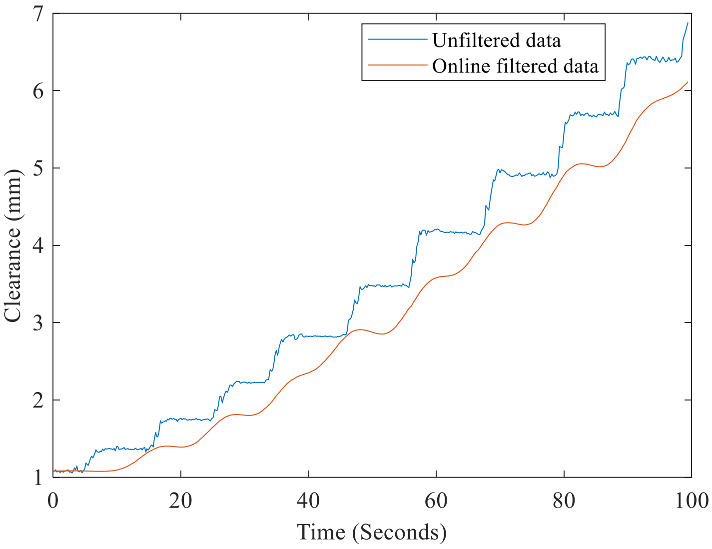

Figure 4-23. LABVIEW online monitoring and filtering of wheel flange measurements

Comparing this with the Direct form II transposed structure used in Simulink IIR filter design, the computation complexity is similar but the delay lines are shared between all poles and zeros sections. This reduces the number of delays while implementing the transfer function as seen in the Simulink filter results, fewer delays are experienced.

5 CONCLUSION AND RECOMMENDATION

5.1. Conclusion

In conclusion, a system that is able to measure the wheel flange thickness in real-time is designed and tested. The effect of temperature on the inductive displacement sensor for wheel flange thickness measurement is tested, analyzed, and evaluated by measuring the clearance between the disk and the sensor tip in the laboratory. This effect manifests in the ambiguity of the displacement measurement of flange thickness when the temperature rises; variations in the measurement data are seen.

The raw data from the two sensors (inductive sensor, thermocouple K type) are correlated using regression equations, to give clear estimates of the disk clearance. Hence, the drift of measurement resulting from the temperature effect is minimized through data prediction methods by the multi-univariate regression model. Based on the analysis done, correlation of the combined data gives reliable real-time measured data by the system as temperatures are elevated around the inductive displacement sensor as the rail vehicle is in operation. Accuracy of the system as the crucial aspect of this measurement system is improved more through frequent calibration by establishing a new multiple regression equation.

During experiments, we realized that the system sensor experience inconsistent repeatability over time. Therefore, a machine learning algorithm is implemented to develop a regression model which self-updates automatically every time more data is added to the database. To increase the accuracy of response, more input measurement data from manual tests need to be added in the database for the system to learn the pattern and behavior of all input conditions to predict a good response.

Finally, an online low pass digital IIR filter was designed to remove noise in the measurements in real-time through software implementation, and the accuracy of the system is increased significantly. Multi-body simulations were used to determine higher frequencies that affect the measurement from vibrations from the locomotive dynamics and track irregularities. The wheelsets and locomotive displacements were taken to propose a suitable design of the sensor support structure mechanism to maintain the coordinate positions range while taking the flange measurements in curved tracks. The system proposed here can be used to monitor the damage of the rail vehicle wheel flange wear in real-time and online.

5.2. Recommendation

a) Testing of the system on locomotive and hardware implementation of the IIR digital filter is recommended to achieve high performance, robust and fast processing of signals to eliminate delays resulting from a higher order of the filter.

b) From the proposed sensor support structure mechanism, kinematic analysis of the mechanism should be analyzed when the rail vehicle is in motion along with different track geometries.

c) This system provides a means of monitoring the wheel wear in real-time with online filtering, and the information can be integrated with the railway communication system.

5.2.1. Hardware filter implementation

As a result of delays during the online filtering observed when the filter order increases using the software implementation, a hardware digital low pass IIR filter implementation is opted to reach optimum operations. Dedicated hardware is required to implement the digital filter requiring high throughput and constrained power dissipation. The performance of the hardware design will depend on the architecture chosen to implement the digital filter. As we try to balance algorithm stability, quantization errors, and design performance, we opt for a range of different filter implementations. For this research, a hardware IIR digital filter design will be implemented based on field-programmable gate arrays (FPGA). FPGAs offer an effective alternative in digital systems due to the short response time in filter development and its implementation on real-time prototypes [52]. The parallel processing capacity of the FPGA logic slices makes the system robust. Consequently, it is obtained a high-performance filter and a quick operation [53].

The filter coefficients will be taken and proved in MATLAB functions. Then they will be transferred to the filter design in the FPGA. Once designed in FPGA, Vivado Design Suit 2020-3 will be used to program the FPGA and then it shall be implemented in Basys-3 to compare the results with those in obtained MATLAB. The implementation of a digital filter on configurable logic involves the explanation of the algorithm with a hardware description language such as the Very-high speed Hardware Description Language (VHDL). Advantages of the hardware description language are modularity and the interoperability of written modules [54].

The FPGA is advancing rapidly as a highly important element of the future of computing. Already developments have shown that it can massively reduce the price of specialized system development and it can complete on a variety of attributes with the top commercially available microprocessors. The basic FPGA architecture consists of a two-dimensional array of logic blocks and flip-flops with the means of the user to configure; the function of each block; the inputs/outputs, and; the interconnection between blocks. Families of FPGAs differ from each other by the physical means for implementing user programmability, arrangement of interconnection wires, and basic functionality of the logic blocks. The design top-level diagram that is implemented in Figure 5-1 displays the sequence and the interaction between signals in all blocks

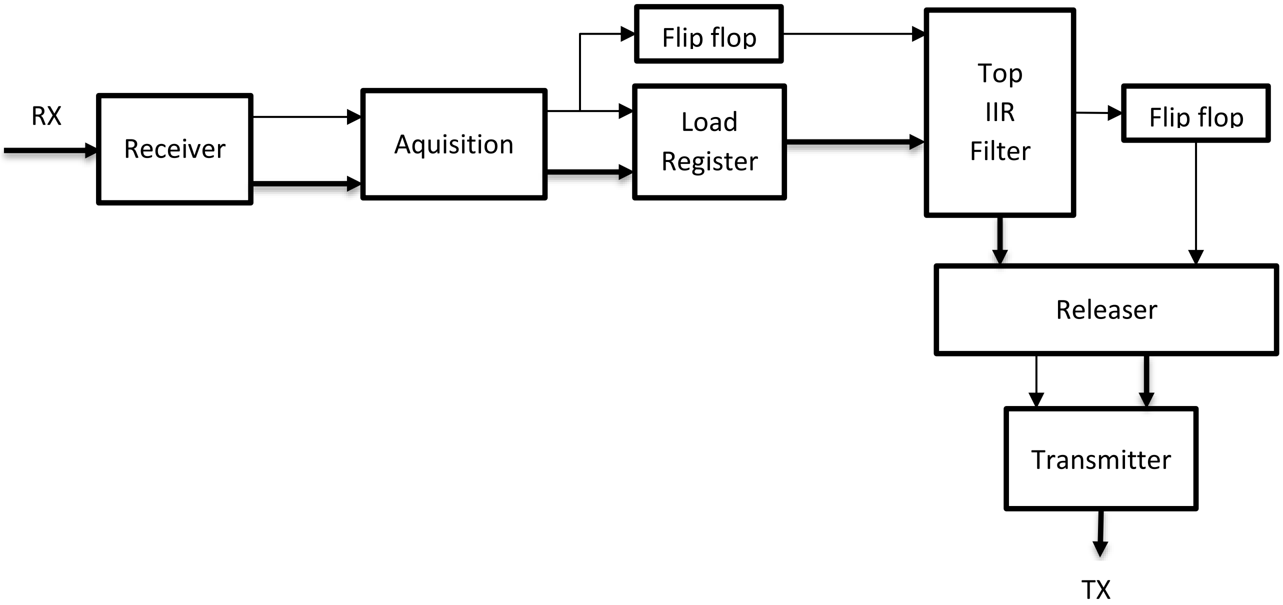

Figure 5-1. Design top-level diagram

The block diagram in Figure 5-2 shows the detailed design of the Top IIR filter block, where the bus signal YKO is the feedback source to the system. The delay blocks will be made up of Load registers (LRs), which store the values from the input signal (XIN) every time the EN signal is active. In that manner, the signal becomes the sample time. The LRs blocks amount will depend on the number of values inside the ROM_Q block which contains the coefficients calculated for the filter. The Bus target counter block shall be responsible for counting the received data whose values will be a force to a certain limit. Implying that the count begins from zero and the first stored value is multiplied with the first value inside the ROM and so on to the last value in the ROM. In this case, all the input and output signals are stored.

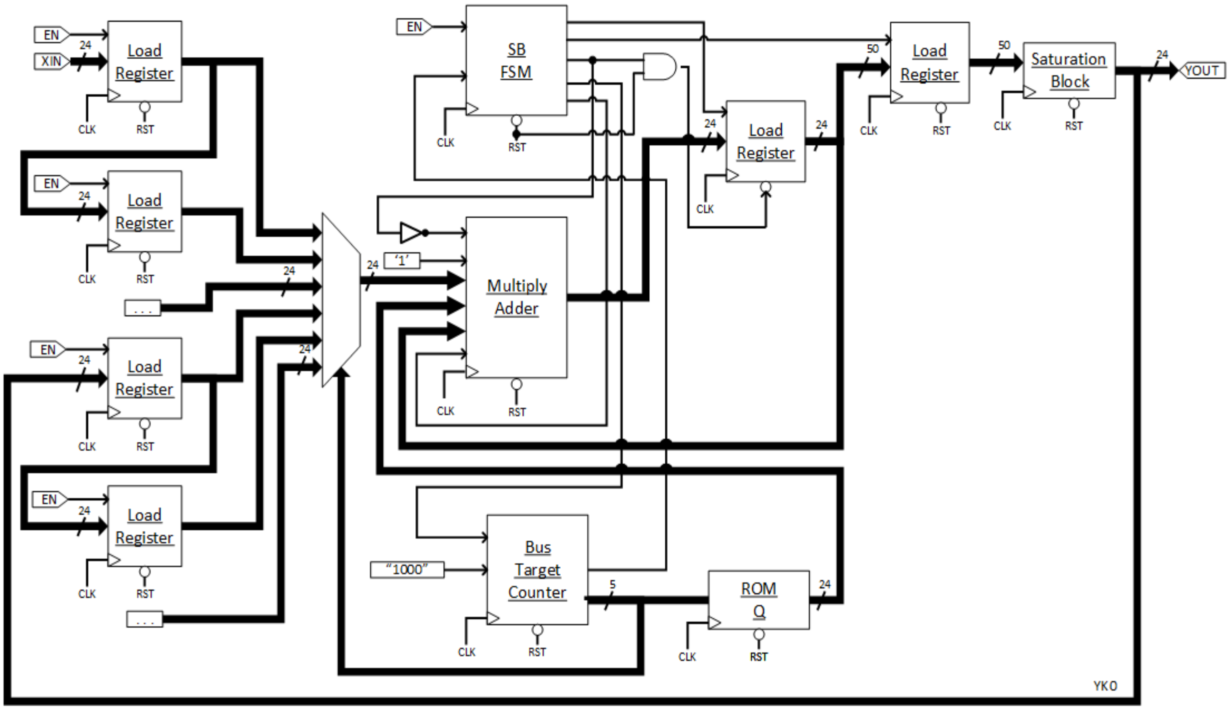

Figure 5-2. Top-level diagram of the IIR filter [41]

At first, the Finite State Machine (FSM) detects the enable signal from EN and it starts to let pass 10 latency clocks. Thus the multiplier adder can yield the results that will be stored in an LR if its output bus signal is going to be returned to the C input of the multiplier adder. From there, the SB FSM gives an impulse to the Bus Target Counter (BTC) to increase its count, and at the same time, it changes the output bus signal. Therefore, it deploys the next signals that are multiplied. In the end, the BTC stores the coefficients in other LR which carry this value until the previous value is computed. The final value cannot be 50-bits length, so it passes through a saturation block which verifies if the signal does not achieve the limit values, and if it does, then the bus is chopped for the output signal to have the same format as the input signal. Furthermore, it can be returned to the line of delays corresponding to $a_n x(k-n)$.

Figure 5-3 below shows a higher-order loop filter factored to a low-level IIR filter design. This is done by making use of a common technique from digital filter design consisting of factoring a higher-order transfer function into a product of second and first-order sections. High-speed IIR filters of arbitrary order are constructed by pipelining the cascade shown.

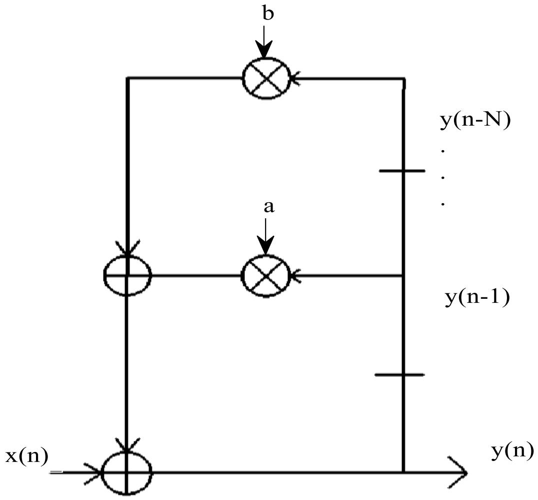

Figure 5-3. Linear time-invariant low-level IIR filter architecture

REFERENCES

[1] D. Serrano-Jiménez, L. Abrahamsson, S. Castaño-Solís, and J. Sanz-Feito, “Electrical railway power supply systems: Current situation and future trends,” *Int. J. Electr. Power Energy Syst.*, vol. 92, pp. 181–192, 2017, doi: 10.1016/j.ijepes.2017.05.008.

[2] H. Soleimani and M. Moavenian, “Tribological Aspects of Wheel–Rail Contact: A Review of Wear Mechanisms and Effective Factors on Rolling Contact Fatigue,” *Urban Rail Transit*, vol. 3, no. 4, pp. 227–237, 2017, doi: 10.1007/s40864-017-0072-2.

[3] Y. Muhamedsalih, J. Stow, and A. Bevan, “Use of railway wheel wear and damage prediction tools to improve maintenance efficiency through the use of economic tyre turning,” *Proc. Inst. Mech. Eng. Part F J. Rail Rapid Transit*, vol. 233, no. 1, pp. 103–117, 2019, doi: 10.1177/0954409718781127.

[4] M. Spiryagin, K. S. Lee, H. H. Yoo, O. Kashura, and S. Popov, “Numerical calculation of temperature in the wheel-rail flange contact and implications for lubricant choice,” *Wear*, vol. 268, no. 1, pp. 287–293, 2010, doi: 10.1016/j.wear.2009.08.014.

[5] P. Turabimana and C. Nkundineza, “Development of an on-board measurement system for railway vehicle wheel flange wear,” *Sensors (Switzerland)*, vol. 20, no. 1, 2020, doi: 10.3390/s20010303.

[6] M. Balog, A. L. Gaunt, M. Brockschmidt, S. Nowozin, and D. Tarlow, “DeepCoder: Learning to write programs,” *5th Int. Conf. Learn. Represent. ICLR 2017 - Conf. Track Proc.*, 2017.

[7] A. K. Menon, O. Tamuz, S. Gulwani, B. Lampson, and A. T. Kalai, “A machine learning framework for programming by example,” *30th Int. Conf. Mach. Learn. ICML 2013*, vol. 28, no. PART 1, pp. 187–195, 2013.

[8] F. Castanedo, “A review of data fusion techniques,” *Sci. World J.*, vol. 2013, 2013, doi: 10.1155/2013/704504.

[9] L. Lin, X. F. Gu, J. P. Li, L. Jie, J. X. Shi, and Y. Y. Huang, “Research on data fusion of multiple biometric features,” *2009 Int. Conf. Apperceiving Comput. Intell. Anal. ICACIA 2009*, pp. 112–115, 2009, doi: 10.1109/ICACIA.2009.5361140.

[10] U. Mechanism, “Mechanical System as an Object for Modeling,” 2012.

[11] C. H. Lee, S. Han, and J. Laskar, “GaAs MESFET dual-gate mixer with active filter design for Ku-band applications,” *IEEE MTT-S Int. Microw. Symp. Dig.*, vol. 2, pp. 841–844, 1999, doi: 10.1109/rfic.1999.805271.

[12] J. Sundh and U. Olofsson, “Seizure mechanisms of wheel-rail contacts under lubricated conditions using a transient ball-on-disc test method,” *Tribol. Int.*, vol. 41, no. 9–10, pp. 867–874, 2008, doi: 10.1016/j.triboint.2007.12.011.

[13] Z. Gong, J. Sun, and G. Zhang, “Dynamic measurement for the diameter of a train wheel based on structured-light vision,” *Sensors (Switzerland)*, vol. 16, no. 4, 2016, doi: 10.3390/s16040564.

[14] G. K. Binnig, "U . S . Patent Feb . 28 , 1989," no. 19, 1989.

[15] X. Cheng, Y. Chen, Z. Xing, Y. Li, and Y. Qin, "A Novel Online Detection System for Wheelset Size in Railway Transportation," *J. Sensors*, vol. 2016, 2016, doi: 10.1155/2016/9507213.

[16] D. Zhan, L. Yu, J. Xiao, and T. Chen, "Multi-camera and structured-light vision system (MSVS) for dynamic high-accuracy 3D measurements of railway tunnels," *Sensors (Switzerland)*, vol. 15, no. 4, pp. 8664–8684, 2015, doi: 10.3390/s150408664.

[17] W. Na, "The Measurement of a Wheel-Flange Wear Based on Digital Image Processing Technology," *Natl. Conf. High. Vocat. Tech. Educ. Comput. Inf.*, pp. 227–229, 2010.

[18] Z. Gong, J. Sun, and G. Zhang, "Dynamic structured-light measurement for wheel diameter based on the cycloid constraint," *Appl. Opt.*, vol. 55, no. 1, p. 198, 2016, doi: 10.1364/ao.55.000198.

[19] R. S. Dwyer-Joyce, C. Yao, R. Lewis, and H. Brunskill, "An ultrasonic sensor for monitoring wheel flange/rail gauge corner contact," *Proc. Inst. Mech. Eng. Part F J. Rail Rapid Transit*, vol. 227, no. 2, pp. 188–195, 2013, doi: 10.1177/0954409712460986.

[20] A. Brezulianu *et al.*, "Inductive Sensors," *Sensors*, vol. 19, no. 3284, p. 16, 2019.

[21] Winncy Y.Du., *Resistive, Capacitive, Inductive & Magnetic Sensor Technologies*. Books by SJSU Authors Book 113, 2014.

[22] Z. Liu, Z. Zhao, Y. Lyu, and L. Zhao, "Experimental investigation of inductive sensor characteristic for blade tip clearance measurement at high temperature," *Sensors (Switzerland)*, vol. 19, no. 17, 2019, doi: 10.3390/s19173694.

[23] F. Lamb, *Industrial Automation: Hands On*. McGraw-Hill Education, 2013.

[24] Thomas. A. Kinney, "Proximity Sensors Compared: Inductive, Capacitive, Photoelectric, and Ultrasonic," *Mach. Des.*, 2001, [Online]. Available: http://www.machinedesign.com/sensors/proximity-sensors-compared-inductive-capacitive-photoelectric-and-ultrasonic.

[25] P. Kejík, C. Kluser, R. Bischofberger, and R. S. Popovic, "A low-cost inductive proximity sensor for industrial applications," *Sensors Actuators, A Phys.*, vol. 110, no. 1–3, pp. 93–97, 2004, doi: 10.1016/j.sna.2003.07.007.

[26] A. Drumea, P. Svasta, and M. Blejan, "Modelling and simulation of an inductive displacement sensor for mechatronic systems," *ISSE 2010 - 33rd Int. Spring Semin. Electron. Technol. Polym. Electron. Nanotechnologies Towar. Syst. Integr. - Conf. Proc.*, pp. 304–307, 2010, doi: 10.1109/ISSE.2010.5547312.

[27] M. R. Nabavi and S. N. Nihtianov, "Design strategies for eddy-current displacement sensor systems: Review and recommendations," *IEEE Sens. J.*, vol. 12, no. 12, pp. 3346–3355, 2012, doi: 10.1109/JSEN.2012.2204321.

[28] D. Vyroubal, V. Vyroubal, and A. Stančić, "Modelling and Simulation of Target Temperature Effect on Eddy Current Sensing: Toward Concurrent Displacement and

Temperature Estimation," *Ijireeice*, vol. 4, no. 4, pp. 133–141, 2016, doi: 10.17148/ijireeice.2016.4432.

[29] H. Wang, B. Ju, W. Li, and Z. Feng, "Ultrastable eddy current displacement sensor working in harsh temperature environments with comprehensive self-temperature compensation," *Sensors Actuators, A Phys.*, vol. 211, pp. 98–104, 2014, doi: 10.1016/j.sna.2014.03.008.

[30] Z. Zhao, Z. Liu, Y. Lyu, and Y. Gao, "Experimental investigation of high temperature-resistant inductive sensor for blade tip clearance measurement," *Sensors (Switzerland)*, vol. 19, no. 1, 2019, doi: 10.3390/s19010061.

[31] S. Durić, L. Nad, B. Biberdžić, M. Damnjanović, and L. Živanov, "Planar inductive sensor for small displacement," *"2008 26th Int. Conf. Microelectron. Proceedings, MIEL 2008,"* no. Miel, pp. 345–348, 2008, doi: 10.1109/ICMEL.2008.4559292.

[32] P. R. Moffitt, "Digital filter design," *EE: Evaluation Engineering*, vol. 42, no. 11. pp. 12-14+16+18, 2003.

[33] A. Antoniou, *Digital Signal Processing: Signals, Systems, and Filters*, 1st ed. McGraw-Hill Professional, 2005.

[34] S. Asgari and A. Mehrnia, "A novel low-complexity digital filter design for wearable ECG devices," *PLoS One*, vol. 12, no. 4, pp. 1–19, 2017, doi: 10.1371/journal.pone.0175139.

[35] R. F. Woods, J. V. McCanny, S. C. Knowles, and O. C. McNally, "A high performance IIR digital filter chip," *Proc. - IEEE Int. Symp. Circuits Syst.*, vol. 2, pp. 1410–1413, 1990, doi: 10.1109/iscas.1990.112395.

[36] J. Kauraniemi, T. I. Laakso, I. Hartimo, and S. J. Ovaska, "Delta operator realizations of direct-form IIR filters," *IEEE Trans. Circuits Syst. II Analog Digit. Signal Process.*, vol. 45, no. 1, pp. 41–52, 1998, doi: 10.1109/82.659455.

[37] G. F. Dehner, "Noise optimized IIR digital filter design - Tutorial and some new aspects," *Signal Processing*, vol. 83, no. 8, pp. 1565–1582, 2003, doi: 10.1016/S0165-1684(03)00075-6.

[38] S. M. Rabiul Islam, R. Sarker, S. Saha, and A. F. M. Nokib Uddin, "Design of a programmable digital IIR filter based on FPGA," *2012 Int. Conf. Informatics, Electron. Vision, ICIEV 2012*, pp. 716–721, 2012, doi: 10.1109/ICIEV.2012.6317409.

[39] H. Chen and L. Wang, "Software and hardware implementation of IIR based on matlab&acceldsp," *Proc. 2012 Int. Conf. Comput. Appl. Syst. Model. ICCASM 2012*, pp. 1411–1415, 2012, doi: 10.2991/iccasm.2012.361.

[40] R. Hourani, H. Alassaly, and W. Alexander, "Hardware implementation of IIR digital filters for programmable devices," *Proc. IEEE Int. Conf. Electron. Circuits, Syst.*, pp. 783–786, 2013, doi: 10.1109/ICECS.2013.6815531.

[41] D. C. Toledo-Pérez, M. A. Martínez-Prado, J. Rodríguez-Reséndiz, S. Tovar Arriaga, and M. A. Márquez-Gutiérrez, "IIR Digital Filter Design Implemented on FPGA for Myoelectric Signals," *2017 13th Int. Eng. Congr. CONIIN 2017*, 2017, doi: 10.1109/CONIIN.2017.7968184.

[42] D. Moskau, “Application of real time digital filters in NMR spectroscopy,” *Concepts Magn. Reson. Part B Magn. Reson. Eng.*, vol. 15, no. 2, pp. 164–176, 2002, doi: 10.1002/cmr.10031.

[43] C. Nkundineza, “Research notes,” *J. Occup. Heal. Saf. - Aust. New Zeal.*, vol. 6, no. 5, p. 352, 2020.

[44] X.-D. Zhang, *Chapter 6 Machine Learning*, vol. 45, no. 13. 2017.

[45] W. Zhai, *Numerical Method and Computer Simulation for Analysis of Vehicle–Track Coupled Dynamics*. 2020.

[46] E. H. Chang, V. K. Garg, C. H. Goodspeed, and S. P. Singh, “Comparative study of the linear and non-linear locomotive response,” *J. Dyn. Syst. Meas. Control. Trans. ASME*, vol. 101, no. 3, pp. 263–271, 1979, doi: 10.1115/1.3426435.

[47] J. N. N. and C. Nkundineza, “DETC2021-66879,” *ASME*, pp. 1–11, 2021.

[48] W. Zhai *et al.*, “High-speed train–track–bridge dynamic interactions – Part I: theoretical model and numerical simulation,” *Int. J. Rail Transp.*, vol. 1, no. 1–2, pp. 3–24, 2013, doi: 10.1080/23248378.2013.791498.

[49] L. Ling, M. Dhanasekar, and D. P. Thambiratnam, “Dynamic response of the train–track–bridge system subjected to derailment impacts,” *Veh. Syst. Dyn.*, vol. 56, no. 4, pp. 638–657, 2018, doi: 10.1080/00423114.2017.1398341.

[50] A. Chudzikiewicz and M. Sowińska, “Modelling the dynamics of an unconventional rail vehicle bogie with independently rotating wheels with the use of Boltzmann-Hamel equations,” *Veh. Syst. Dyn.*, 2020, doi: 10.1080/00423114.2020.1838567.

[51] E. Demir, “3D Suspension Characterization of a Rapid Transit Vehicle Using a Multi-Body Dynamic Model,” *Urban Rail Transit*, vol. 2, no. 3–4, pp. 172–187, 2016, doi: 10.1007/s40864-016-0045-x.

[52] Arjuna Madanayake and Len Bruton “FPGA architectures for real-time 2d / 3d fir / iir plane wave filters", FIEEE and Chris Comis Department of Electrical and Computer Engineering Alberta , Canada,” pp. 2–5.

[53] C. Zhao and Z. Zhang, “Digital filter design and performance analysis of dynamic temperature signal denoise based on FPGA,” *Proc. Int. Conf. Sens. Technol. ICST*, 2016, doi: 10.1109/ICSensT.2016.7796285.

[54] D. Costa and C. S. Paez, “A comparative analysis of hardware techniques for implementation of IIR digital filter on FPGA,” *IEEE*, pp. 5–10, 2015.

APPENDIX

Appendix A. Multi-body simulation physical variables and input parameters

Table 0-1. Physical meaning of notations used in equations of motions of locomotive model

Notation	Physical meaning
d_o	half of the distance between the left and right wheel-rail contact point
e_1, e_2	half of the transverse distance between vertical primary and secondary suspension
C	damping matrix
C_{1x}, C_{1y}, C_{1z}	damping of longitudinal, lateral, and vertical primary suspension
C_{2x}, C_{2y}, C_{2z}	damping of longitudinal, lateral, and vertical secondary suspension
F	vector of external forces
$F_{Lyj}, F_{Ry}, F_{Lzj}, F_{Rzj}$	lateral and vertical component of tangential creep force at the left and right wheel-rail contact point of the jth wheelset
$F_{xf(L,R)j}, F_{yf(L,R)j}, F_{zf(L,R)j}$	longitudinal, lateral, and vertical force of primary suspension of the jth wheelset
$F_{xs(L,R)i}, F_{ys(L,R)i}, F_{zs(L,R)i}$	longitudinal, lateral, and vertical force of secondary suspension of the ith wheelset
g	Gravitational coefficient
h	superelevation
h_1	perpendicular distance between center of gravity of the locomotive body and lateral secondary suspension
h_2	perpendicular distance between center of gravity of bogie and lateral primary suspension
h_3	perpendicular distance between center of gravity of bogie and lateral primary suspension
$I_{lcx}, I_{lcy}, I_{lcz}$	moment of inertia of locomotive body around the x,y, and z axes
I_{bx}, I_{by}, I_{bz}	moment of inertia of bogie around the x,y, and z axes
I_{wx}, I_{wz}	moment of inertia of wheelset around the x, and z axes
K	stiffness matrix
K_{1x}, K_{1y}, K_{1z}	stiffness of longitudinal, lateral, and vertical primary suspension
K_{2x}, K_{2y}, K_z	stiffness of longitudinal, lateral, and vertical secondary suspension
l_{lc}	half of the distance between two bogie centres
l_b	half of the wheelbase
m	mass matrix
m_{lc}, m_b, m_w	mass of loco-body, bogie and wheelset
$N_{Lzj}, N_{Lyj} N_{Rzj}, N_{Ryj}$	vertical and lateral component of normal force at the left and right wheel-rail contact point of the jth wheelset
R	radius of circular arc

R_{lc}, R_b, R_{wj}	radius at centre of gravity of loco-body, ith bogie and jth wheelset
V	train speed
y_{lc}, y_{bi}, y_{wj}	lateral displacement of loco-body, ith bogie, and jth wheelset
z_{lc}, z_{bi}, z_{wj}	vertical displacement of loco-body, ith bogie, and jth wheelset
$\theta_{lc}, \theta_{bi}, \theta_{wj}$	rolling angular displacement of loco-body, ith bogie and jth wheelset
$\theta_{selc}, \theta_{sebi}, \theta_{sewj}$	superelevation at center of gravity of locobody, ith bogie and jth wheelset
$\varphi_{lc}, \varphi_{bi}$	pitching angular displacement of loco-body and the ith bogie

Table 0-2. Input parameters of the Locomotive

Name	Expression	Value	Comment
v0		20	
vehiclebase		14.42	
m_body		8.1000000E+4	
i_body_x		1.8000000E+5	
i_body_y		3.5000000E+6	
i_body_z		3.5000000E+6	
c_tractionrod		9.0000000E+6	Stiffness of traction rod, N/m
d_tractionrod		1.0000000E+4	Damping coefficient of traction rods, Ns/m
h_body		2.2	

Table 0-3. Bogie 1 input parameter

Name	Expression	Value	Comment
v0		20	Initial velocity
r_Wheel		0.625	Radius of wheel
x_Wheel_1		1.971	Position of 1st wheelset motor assembly along X - axis
x_Wheel_3		-2.655	Position of 3rd wheelset motor assembly along X - axis
x_Spring		0.08	Position of spring along X - axis
dx_Spring		0.39	The longitudial stiffness of spring
h_Spring		0.6	The height of spring
c_x_2		6.5000000E+4	Shear stiffness in axlebox suspension
c_z_2		5.6100000E+5	Stiffness coefficient in axlebox suspension
m_Body		8.1000000E+4	Mass of body
f_st_2	m_Body*9.81/ 12/c_z_2	0.11803476	Static deflection in the secondary suspension
c_Spr2lv_bending		1000	Bending stiffness coefficient of spring of 2nd level suspension
d_Spr2lv_z		8.0000000E+4	Z damping coefficient of secondary suspension
d_Spr2lv_y		8.0000000E+4	Y damping coefficient of secondary suspension

d_Spr2lv_x		8.0000000E+4	X damping coefficient of secondary suspension
l_Traction	sqrt(sqr(3)+sqr(0.075))	3.0009374	The length of traction
a_Traction	(1+26/60)*pi/180	0.025016386	The angle of traction with respect to horizontal
c_Traction_x		2.5000000E+7	X stiffness coefficient of traction rod
c_Traction_y		2.5000000E+7	Y stiffness coefficient of traction rod
c_Traction_z		2.5000000E+7	Z stiffness coefficient of traction rod
c_Traction_a		1.0000000E+5	Angular stiffness coefficient of traction rod
d_Traction_x	0.1*sqrt(c_traction_x*600)	1.2247449E+4	X damping coefficient of traction rod
d_Traction_a	0.2*sqrt(c_traction_a*1000)	2000	Angular damping coefficient of traction rod
m_Frame		1.1000000E+4	Mass of bogie frame without railway motor
i_Frame_x		4000	X moment of inertia of bogie frame
i_Frame_y		1.5000000E+4	Y moment of inertia of bogie frame
i_Frame_z		1.8000000E+4	Z moment of inertia of bogie frame

Table 0-4. Bogie 2 input parameters

Name	Expression	Value	Comment
v0		20	Initial velocity
c_RRod		2.0000000E+7	Stiffness coefficient reactive rod reducer
d_RRod		1.0000000E+4	Damping coefficient on reactive rod reducer
c_z_1	1570000/2	7.8500000E+5	Stiffness coefficient in axlebox suspension
c_x_1		7.5000000E+5	Shear stiffness in axlebox suspension
m_Reducer		500	Mass of reducer
x_Reducer		-0.2	Õ coordinate of the center of mass of reducer
i_Reducer_y		150	Y moment of inertia of reducer
m_RWMotor		3000	Mass of traction motor
m_Body		8.1000000E+4	Mass of body
m_Frame		4200	Mass of bogie frame without railway motor
f_St_1	(m_Body+2*m_Frame+6*(m_RWMotor+m_Reducer*0.2/0.747))*9.81/24/c_z_1	0.056341482	Static deflection in the primary suspension
i_TMotor_x		320	Õ moment of inertia of traction motor
i_TMotor_y		300	Y moment of inertia of traction motor
i_TMotor_z		320	Z moment of inertia of traction motor
x_TMotor		0.887	Õ coordinate center of mass of traction motor
y_TMotor		0.597	Y coordinate center of mass of traction motor
z_TMotor		-0.265	Z coordinate center of mass of traction motor
i_Rotor_y		45.44	Y moment of inertia of rotor
r_GWheel		0.128184	Radius of gear wheel
c_Reducer		1.0000000E+7	Reduced stiffness coefficient in reducer
d_Reducer		1.0000000E+4	Reduced damping coefficient in reducer

i_Cardan_x		20	Y moment of inertia of cardan shaft of driving gear
c_RCCoupler_torsion		2.6000000E+5	Torsion stiffness coefficient of rubber-cord coupler
c_RCCoupler_x		2.1075269E+7	Õ stiffness coefficient of rubber-cord coupler
c_RCCoupler_bending		2.2500000E+4	Bending stiffness coefficient of rubber-cord coupler
d_RCCoupler		600	Torsion damping coefficient of rubber-cord coupler
d_RCCoupler_x		500	Õ damping coefficient of rubber-cord coupler
MultiplierRod		0	Multiplier 0.8 in rate traction
ShiftAxleBox		1.085	Shear of axle-box along X - axis
c_Lead_x		1.2500000E+7	Stiffness coefficient of lead along X - axis
c_Lead_y		2.5000000E+6	Stiffness coefficient of lead along Y - axis
d_AxleBox_1part		2.5600000E+4	Damping coefficient of the first part of the characteristic
v_damper		0.125	Breaking point in the damper force diagram, m/s
d_AxleBox_2part		1850	Damping coefficient of second part characteristic
m_WSet		3105	Mass of wheelset
B_Lead		0.05	Damping ratio
d_Lead_x	2*B_Lead*sqrt(m_WSet*c_Lead_x)	1.9700888E+4	X damping coefficient of lead
d_Lead_y	2*B_Lead*sqrt(m_WSet*c_Lead_y)	8810.5051	Y damping coefficient of lead
i_AxleBox_y		3	Y moment of inertia axle-box
m_AxleBox		50	Mass of axle-box
Eccentricity		0.02	Eccentricity of lead
i_reducer_x		66	
i_reducer_z		100	
m_rotor		200	
i_rotor_x		118	
m_cardan		80	
i_cardan_y		3.3	
i_axlebox_x		1.84	
i_axlebox_z		3.17	

Table 0-5. Wheelset 1 input parameters

Name	Expression	Value	Comment
v0		20	Initial velocity
c_RRod		2.0000000E+7	Stiffness coefficient reactive rod reducer
d_RRod		1.0000000E+4	Damping coefficient on reactive rod reducer
c_z_1	1570000/2	7.8500000E+5	Stiffness coefficient in axlebox suspension
c_x_1		7.5000000E+5	Shear stiffness in axlebox suspension
m_Reducer		500	Mass of reducer
x_Reducer		-0.2	Õ coordinate of the center of mass of reducer
i_Reducer_y		150	Y moment of inertia of reducer
m_RWMotor		3000	Mass of traction motor
m_Body		8.1000000E+4	Mass of body
m_Frame		4200	Mass of bogie frame without railway motor

f_St_1	(m_Body+2*m_Frame+6*(m_RWMotor+m_Reducer*0.2/0.747))*9.81/24/c_z_1	0.056341482	Static deflection in the primary suspension
i_TMotor_x		320	Õ moment of inertia of traction motor
i_TMotor_y		300	Y moment of inertia of traction motor
i_TMotor_z		320	Z moment of inertia of traction motor
x_TMotor		0.887	Õ coordinate center of mass of traction motor
y_TMotor		0.597	Y coordinate center of mass of traction motor
z_TMotor		-0.265	Z coordinate center of mass of traction motor
i_Rotor_y		45.44	Y moment of inertia of rotor
r_GWheel		0.128184	Radius of gear wheel
c_Reducer		1.0000000E+7	Reduced stiffness coefficient in reducer
d_Reducer		1.0000000E+4	Reduced damping coefficient in reducer
i_Cardan_x		20	Y moment of inertia of cardan shaft of driving gear
c_RCCoupler_torsion		2.6000000E+5	Torsion stiffness coefficient of rubber-cord coupler
c_RCCoupler_x		2.1075269E+7	Õ stiffness coefficient of rubber-cord coupler
c_RCCoupler_bending		2.2500000E+4	Bending stiffness coefficient of rubber-cord coupler
d_RCCoupler		600	Torsion damping coefficient of rubber-cord coupler
d_RCCoupler_x		500	Õ damping coefficient of rubber-cord coupler
MultiplierRod		0	Multiplier 0.8 in rate traction
ShiftAxleBox		1.085	Shear of axle-box along OX - axis
axlebox_gap		0.015	Allow lateral displacement of wheelset
f_axlebox_friction		0.05	
c_gap		1.0000000E+7	Stiffness coefficient of axle bump stop
faxlebox_friction	(m_Body+2*m_Frame+6*m_RWMotor)*9.81/12*f_axlebox_friction	4389.975	
c_Lead_x		1.2500000E+7	Stiffness coefficient of lead along X - axis
c_Lead_y		2.5000000E+6	Stiffness coefficient of lead along Y - axis
d_AxleBox_1part		2.5600000E+4	Damping coefficient of the first part of the characteristic
v_damper		0.125	Breaking point in the damper force diagram, m/s
d_AxleBox_2part		1850	Damping coefficient of second part characteristic
m_WSet		3105	Mass of wheelset
B_Lead		0.05	Damping ratio
d_Lead_x	2*B_Lead*sqrt(m_WSet*c_Lead_x)	1.9700888E+4	X damping coefficient of lead
d_Lead_y	2*B_Lead*sqrt(m_WSet*c_Lead_y)	8810.5051	Y damping coefficient of lead
i_AxleBox_y		3	Y moment of inertia axle-box

m_AxleBox		50	Mass of axle-box
Eccentricity		0.02	Eccentricity of lead
i_reducer_x		66	
i_reducer_z		100	
m_rotor		200	
i_rotor_x		118	
m_cardan		80	
i_cardan_y		3.3	
i_axlebox_x		1.84	
i_axlebox_z		3.17	

Table 0-6. Wheelset 2 input parameters

Name	Expression	Value	Comment
v0		20	Initial velocity
c_RRod		2.0000000E+7	Stiffness coefficient reactive rod reducer
d_RRod		1.0000000E+4	Damping coefficient on reactive rod reducer
c_z_1	1570000/2	7.8500000E+5	Stiffness coefficient in axlebox suspension
c_x_1		7.5000000E+5	Shear stiffness in axlebox suspension
m_Reducer		500	Mass of reducer
x_Reducer		-0.2	Õ coordinate of the center of mass of reducer
i_Reducer_y		150	Y moment of inertia of reducer
m_RWMotor		3000	Mass of traction motor
m_Body		8.1000000E+4	Mass of body
m_Frame		4200	Mass of bogie frame without railway motor
f_St_1	(m_Body+2*m_Frame+6*(m_RWMotor+m_Reducer*0.2/0.747))*9.81/24/c_z_1	0.056341482	Static deflection in the primary suspension
i_TMotor_x		320	Õ moment of inertia of traction motor
i_TMotor_y		300	Y moment of inertia of traction motor
i_TMotor_z		320	Z moment of inertia of traction motor
x_TMotor		0.887	Õ coordinate center of mass of traction motor
y_TMotor		0.597	Y coordinate center of mass of traction motor
z_TMotor		-0.265	Z coordinate center of mass of traction motor
i_Rotor_y		45.44	Y moment of inertia of rotor
r_GWheel		0.128184	Radius of gear wheel
c_Reducer		1.0000000E+7	Reduced stiffness coefficient in reducer

d_Reducer		1.0000000E+4	Reduced damping coefficient in reducer
i_Cardan_x		20	Y moment of inertia of cardan shaft of driving gear
c_RCCoupler_torsion		2.6000000E+5	Tortion stiffness coefficient of rubber-cord coupler
c_RCCoupler_x		2.1075269E+7	Õ stiffness coefficient of rubber-cord coupler
c_RCCoupler_bending		2.2500000E+4	Bending stiffness coefficient of rubber-cord coupler
d_RCCoupler		600	Torsion damping coefficient of rubber-cord coupler
d_RCCoupler_x		500	Õ damping coefficient of rubber-cord coupler
MultiplierRod		0	Multiplier 0.8 in rate traction
ShiftAxleBox		1.085	Shear of axle-box along OX - axis
c_Lead_x		1.2500000E+7	Stiffness coefficient of lead along X - axis
c_Lead_y		2.5000000E+6	Stiffness coefficient of lead along Y - axis
d_AxleBox_1part		2.5600000E+4	Damping coefficient of the first part of the characteristic
v_damper		0.125	Breaking point in the damper force diagram, m/s
d_AxleBox_2part		1850	Damping coefficient of second part characteristic
m_WSet		3105	Mass of wheelset
B_Lead		0.05	Damping ratio
d_Lead_x	2*B_Lead*sqrt(m_WSet*c_Lead_x)	1.9700888E+4	X damping coefficient of lead
d_Lead_y	2*B_Lead*sqrt(m_WSet*c_Lead_y)	8810.5051	Y damping coefficient of lead
i_AxleBox_y		3	Y moment of inertia axle-box
m_AxleBox		50	Mass of axle-box
Eccentricity		0.02	Eccentricity of lead
i_reducer_x		66	
i_reducer_z		100	
m_rotor		200	
i_rotor_x		118	
m_cardan		80	
i_cardan_y		3.3	
i_axlebox_x		1.84	
i_axlebox_z		3.17	

Table 0-7. Wheelset 3 input parameters

Name	Expression	Value	Comment

v0		20	Initial velocity
r_Wheel		0.625	Radius of wheel
x_Wheel_1		1.971	Position of 1st wheelset motor assembly along X - axis
x_Wheel_3		-2.655	Position of 3rd wheelset motor assembly along X - axis
x_Spring		0.08	Position of spring along X - axis
dx_Spring		0.39	The longitudial stiffness of spring
h_Spring		0.6	The height of spring
c_x_2		6.5000000E+4	Shear stiffness in axlebox suspension
c_z_2		5.6100000E+5	Stiffness coefficient in axlebox suspension
m_Body		8.1000000E+4	Mass of body
f_st_2	m_Body*9.81/12/c_z_2	0.11803476	Static deflection in the secondary suspension
c_Spr2lv_bending		1000	Bending stiffness coefficient of spring of 2nd level suspension
d_Spr2lv_z		8.0000000E+4	Z damping coefficient of secondary suspension
d_Spr2lv_y		8.0000000E+4	Y damping coefficient of secondary suspension
d_Spr2lv_x		8.0000000E+4	X damping coefficient of secondary suspension
l_Traction	sqrt(sqr(3)+sqr(0.075))	3.0009374	The length of traction
a_Traction	(1+26/60)*pi/180	0.025016386	The angle of traction with respect to horizontal
c_Traction_x		2.5000000E+7	X stiffness coefficient of traction rod
c_Traction_y		2.5000000E+7	Y stiffness coefficient of traction rod
c_Traction_z		2.5000000E+7	Z stiffness coefficient of traction rod
c_Traction_a		1.0000000E+5	Angular stiffness coefficient of traction rod
d_Traction_x	0.1*sqrt(c_traction_x*600)	1.2247449E+4	X damping coefficient of traction rod
d_Traction_a	0.2*sqrt(c_traction_a*1000)	2000	Angular damping coefficient of traction rod
m_Frame		1.1000000E+4	Mass of bogie frame without railway motor
i_Frame_x		4000	X moment of inertia of bogie frame
i_Frame_y		1.5000000E+4	Y moment of inertia of bogie frame
i_Frame_z		1.8000000E+4	Z moment of inertia of bogie frame

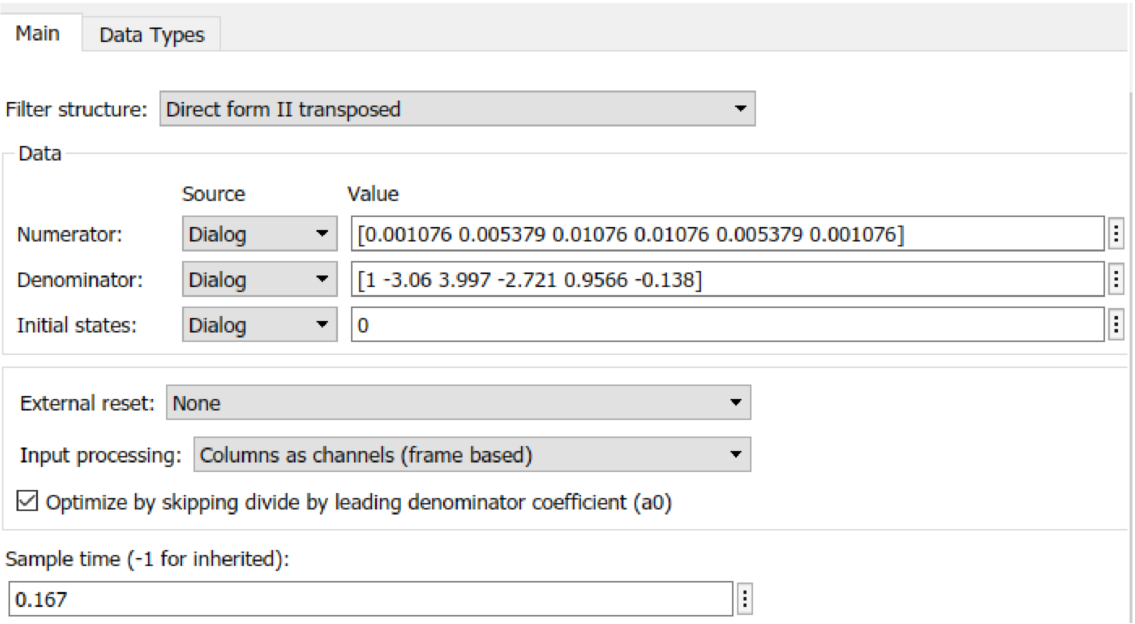

Filter structure: Direct form II transposed

Data

	Source	Value
Numerator:	Dialog	[0.001076 0.005379 0.01076 0.01076 0.005379 0.001076]
Denominator:	Dialog	[1 -3.06 3.997 -2.721 0.9566 -0.138]
Initial states:	Dialog	0

External reset: None

Input processing: Columns as channels (frame based)

☑ Optimize by skipping divide by leading denominator coefficient (a0)

Sample time (-1 for inherited):

0.167

Figure 0-1. Written transfer function in Simulink online filter model

Appendix B. Matlab codes for FFT analysis

```
clc
clear all
Load d6.mat

x=DX6.cleearance; %signal
fax_bins=[0:1101]; %frequency axis in bins
v=fax_bins;
X_mags =abs(fft(x));
y=X_mags;
N_2=ceil(N/2);
plot(v,y);
xlabel('Frequency (Hz)')
ylabel('Magnitude')
```

Appendix C. Matlab codes for data fittings

```
clc
load ML

x=expd1S2.voltage;

y=expd1S2.temperature;

z=expd1S2.clearancemm;

cftool

xlabel('Voltage (volts)')

ylabel('Temperature')

zlabel('Clearance (mm)')

////
```

```
clc

load TTP.mat
x=expd1S1.clearancemm;
y=expd1S1.err1;
y1=expd1S1.err11;
y2=expd1S1.err12;
%y3=expd1S1.err10;
%x=expd1S2.Tempearature;

plot(x,y,'*')
xlabel('Clearance (mm)');
ylabel('Error (volts)');
hold on
plot(x,y1,'v')
hold on
plot(x,y2,'x')
hold off
%plot(x,y3,'v')
clc
load TTP.mat
x=expd1S1.clearancemm;
y=expd1S1.err1;
y1=expd1S1.err11;
y2=expd1S1.err12;
%y3=expd1S1.err10;
%x=expd1S2.Tempearature;
plot(x,y,'*')
xlabel('Clearance (mm)');
ylabel('Error (volts)');
hold on
plot(x,y1,'v')
hold on
plot(x,y2,'x')
hold off
%plot(x,y3,'v'
////
clc
```

```
load x1.mat
x=expd1S2.clearancemm;
y=expd1S2.err1;
y1=expd1S2.err5;
y2=expd1S2.err6;
y3=expd1S2.err7;
%x=expd1S2.Tempearature;
plot(x,y,'*')
xlabel('Clearance (mm)');
ylabel('Error (volts)');
hold on
plot(x,y1,'v')
hold on
plot(x,y2,'x')
hold on
plot(x,y3,'v')
hold off
```

Appendix D. Matlab code for Filtering

```
%%Designing a Lowpass IIR Filter
load d6
t=DX6.time;
x2=DX6.distance;
N=5;
Fp=0.21128;
Ap=0.1737;
h=fdesign.lowpass('N,Fp,Ap', N, Fp, Ap, Fs);
d=design(h, 'butter');
%%Apply the filter to to Smooth out the Signal
xfilter = filter(d,x2);
%%Overlay the filtered signal on the original signal.
% Filtered signal is delayed
figure;
plot(t2,x2,'b',t2,xfilter,'r');
grid on;
legend({'Original Signal','Filtered Signal'});
%set(gcf,'NumberTitle','Off', 'Name','Filtered Signal vs. Actual Signal');
```

```
%%Compare the original signal and delay compensated filtered signal
figure;
xfiltfilt = filtfilt(d.sosMatrix,d.ScaleValues,x2);
plot(t2,x2,t2,xfiltfilt);
grid on
legend({'Original Signal','Actual (filtered and delayed signal)'});
/////
clc
s=tf('s');
Hs=1/(0.0169*s^5+0.12362*s^4+0.4524*s^3+1.0234*s^2+1.431*s+1)
%Hs=1/((7.465*10^-
3)*s^6+0.0653*s^5+0.2851*s^4+0.7899*s^3+0.7552*s^2+1.7082*s+1)
Hz=c2d(Hs,0.167,'tustine')
///

load bowman.mat
t=DX6.time;
x=DX6.distance;
% create the filter coefficients
a=[1 -3.564 5.235 -3.9322 1.504 -0.23372];
b=[0.000286 0.00143 .00286 0.00286 0.00143 0.000286];
%now we compute the moving average of the data
y =filter(b,a,x);
plot(t,x,'.',t,y,'-')
xlabel('Time (seconds)')
ylabel('Distance (mm)')
legend('Original data','Filtered data')
```